

MASTER OF SCIENCE THESIS

Modelling Delamination in an Equivalent Single Layer Model in Explicit Finite Element Analysis

J. Koeman

Faculty of Aerospace Engineering · Delft University of Technology

Modelling Delamination in an Equivalent Single Layer Model in Explicit Finite Element Analysis

MASTER OF SCIENCE THESIS

For obtaining the degree of Master of Science in Aerospace Engineering
at Delft University of Technology

J. Koeman

19-Dec-2017

The work in this thesis was supported by BMW AG. Their cooperation is gratefully acknowledged.



Copyright © J. Koeman
All rights reserved.



Rolls-Royce
Motor Cars Limited

DELFT UNIVERSITY OF TECHNOLOGY
FACULTY OF AEROSPACE ENGINEERING
DEPARTMENT OF AEROSPACE STRUCTURES AND MATERIALS

GRADUATION COMMITTEE

Dated: 19-Dec-2017

Chair holder:

Prof. dr. C. Bisagni

Committee members:

Dr. C. Kassapoglou

Dr. D. Zarouchas

C. Bögle

Abstract

The combination of continuously increasing safety standards and harder requirements on the emissions of cars leads to a challenge for the automotive industry: cars need to become safer and more efficient. One way to overcome this challenge is to make use of Carbon Fibre Reinforced Polymers (CFRP) in the car frame. CFRP laminates have vastly different failure modes than metal and are generally anisotropic. As a consequence, the structural concepts perfected for metals may not be the best ones for CFRP frames, hence, re-evaluation of them is needed to obtain the structurally most efficient concept for a CFRP car frame.

Finite Element Analysis (FEA) is chosen as one of the tools to evaluate these concepts. However, one problem is that currently there is no method to model CFRP which can be used in the context of car crash simulations, without the requirement of specifying the exact stacking sequence of the used laminates. Therefore, a new method is being developed for the implementation in a commercially available FEA software package (LS-Dyna) which does fulfil this requirement. The basis of this method is that it compacts a whole CFRP laminate into one element through thickness with a homogenized material, making use of the Equivalent Single Layer (ESL) theory. This thesis provides an approach to include one of the failure modes of CFRP in the method: delamination.

As foundation for the new method, a four-noded bilinear element based on First-order Shear Deformation Theory (FSDT) is chosen due to its low computational cost during processing. The problem with combining this element with the ESL theory, is that it is not possible to model the kinematics of delamination. Because of this, delamination in the new method is split into two parts: the detection of onset of delamination and modelling the effects of delamination.

For the detection of delamination, a stress-based failure criterion is chosen, following the failure theory of Alfred Puck and a quadratic delamination failure criterion. However, transverse stresses are not accurately predicted in FSDT: transverse shear stresses are assumed to be constant through thickness and transverse normal stresses are assumed to be zero. Therefore, each time step is post-processed automatically to recover more accurate transverse stresses. The result is a parabolic distribution of the shear stresses through thickness, however, due to the absence of parabolic shape functions in the four-noded bilinear element, transverse normal stresses are not recovered.

Since the kinematics of delamination cannot be modelled with the chosen four-noded element in combination with the ESL theory, each structural effect of delamination is analysed separately. The reduction of bending stiffness (to 25% of the undamaged laminate) and the reduction in stresses due to bending (to 50% of the undamaged laminate) are considered the most severe and are therefore selected to be implemented into the method. The implementation is done by applying a damage factor in the calculation of the stresses at an integration point. Afterwards, the same damage factor is used in the calculation of the nodal moments, simulating the desired bending stiffness. Since undamaged material surrounding a delamination can stiffen the delaminated part of a structure, only elements which are part of two perpendicular free edges or connected to them via a continuous delamination should have a reduction in bending stiffness and stress. Therefore, an algorithm is developed which identifies these elements.

The previously described method of modelling delamination in two-dimensional FEA models has been compared to finely meshed three-dimensional FEA models, by modelling square cantilever plates with differing shapes of delamination. First a benchmark model without delamination was tested: a square cantilever plate with a length 10 times the thickness of the plate, resulting in the shell elements over-predicting the out-of-plane displacement at the tip of the plate by 5.9%. The two models with common delaminations, a plate with a one-dimensional delamination and a plate with a moderate size square two-dimensional delamination, showed comparable over-prediction of the displacement. Finally, the two models with more uncommon delaminations, a plate with a two-dimensional delamination on the brink of becoming a one-dimensional delamination (i.e. progressing towards a third perpendicular free edge) and a plate with a slender delamination, showed more inaccurate results, with approximately 30% over-prediction of the deflection.

Several sidetracks and new problems arose during this research which have not been explored yet, and are therefore recommendations for further work. Due to time constraints exact implementation of the effects of delamination was not possible in the finite element software; a comparable method (manually assigning the delaminated area) was used to examine the results of the method. Implementation of the method would allow for better comparison to three-dimensional results, both obtained due to experimental tests as well as more detailed FEA. Next to this, while free edges and delamination crack fronts are identified using the earlier mentioned algorithm, their effects on delamination onset and growth have not been implemented. Hence, while this thesis provides an approach to model delamination in an equivalent single layer model in explicit finite element analysis, there are still possibilities left to enhance the capabilities and increase the accuracy of this approach.

Table of Contents

| | |
|---|-------------|
| List of Figures | xiii |
| List of Tables | xv |
| Nomenclature | xvii |
| Preface | xxi |
| 1 Introduction | 1 |
| 2 Behaviour of Composite Structures | 3 |
| 2.1 Basics of Composite Materials | 3 |
| 2.2 First-Order Shear Deformation Theory | 5 |
| 2.2.1 Expansion for Composite Materials | 6 |
| 2.2.2 Stiffness of the Homogenised Material Model | 8 |
| 2.3 Failure Modes of Composites on Micro Scale | 9 |
| 2.3.1 Failure of Fibres | 10 |
| 2.3.2 Interfacial Debonding | 11 |
| 2.3.3 Matrix Fracture | 11 |
| 2.3.4 Delamination | 11 |
| 2.4 Laminate Failure in In-Plane Impact Events | 12 |
| 2.4.1 Plastic Buckling of Composites | 12 |
| 2.4.2 Composite Crushing | 13 |
| 2.5 Delamination | 14 |
| 2.5.1 Causes of Delamination | 14 |
| 2.5.2 Effects of Delamination | 17 |

| | | |
|----------|--|-----------|
| 3 | Finite Element Framework and Initial Concept | 21 |
| 3.1 | Explicit Solution Scheme | 22 |
| 3.2 | Belytschko-Lin-Tsay Shell Element | 23 |
| 3.2.1 | Corotational Formulation | 23 |
| 3.2.2 | Velocity Strain Formulation | 24 |
| 3.2.3 | Stress and Force Calculation | 25 |
| 3.3 | Initial Considerations for Concept | 27 |
| 3.4 | Current Methods of Modelling Delamination in Finite Element Analysis | 27 |
| 3.5 | User Modules of LS-Dyna | 29 |
| 4 | Prediction of Delamination Initiation | 33 |
| 4.1 | Prediction of Transverse Stresses | 34 |
| 4.1.1 | State of Art Literature on Transverse Stresses in Finite Element Analysis | 34 |
| 4.1.2 | Prediction of Transverse Stresses in Shell Elements | 39 |
| 4.1.3 | Attempts on Obtaining Transverse Normal Stress | 42 |
| 4.1.4 | Application to Homogenised Material Model | 44 |
| 4.1.5 | Implementation in LS-Dyna | 48 |
| 4.2 | Delamination Failure Criteria and Adaptation for Shell Elements | 48 |
| 4.2.1 | State of Art Literature on Delamination Failure Criteria | 48 |
| 4.2.2 | Puck's Failure Criteria for Pure Delamination | 52 |
| 4.2.3 | Delamination Criteria Without Transverse Normal Stress | 53 |
| 4.2.4 | Implementation | 54 |
| 4.3 | Summary | 54 |
| 4.3.1 | Conclusion | 54 |
| 4.3.2 | Outlook | 55 |
| 5 | Effects of Delamination | 57 |
| 5.1 | Analysis on Effects of Delamination | 57 |
| 5.1.1 | Compression Strength Reduction | 57 |
| 5.1.2 | Membrane Stiffness Reduction | 58 |
| 5.1.3 | Bending Stiffness Reduction | 58 |
| 5.2 | Implementation | 59 |
| 5.2.1 | In-Plane Strength and Damage Evolution | 60 |
| 5.2.2 | Virtual Strain Reduction | 61 |
| 5.2.3 | Free Edge Indicator | 62 |
| 5.3 | Verification | 67 |
| 5.3.1 | Model Descriptions | 67 |
| 5.3.2 | Results | 69 |
| 5.4 | Summary | 75 |
| 5.4.1 | Conclusion | 75 |
| 5.4.2 | Outlook | 76 |

| | | |
|----------|---|-----------|
| 6 | Conclusions and Recommendations | 77 |
| | References | 81 |
| A | Obtaining Transverse Normal Stresses in a One-Dimensional Linear Element | 89 |
| B | Transverse Normal Stress Implementation | 93 |

List of Figures

| | | |
|------|--|----|
| 2.1 | Stacking sequence of a quasi-isotropic laminate | 5 |
| 2.2 | Definition of angles used in FSDT in the xz -plane | 6 |
| 2.3 | Failure modes of CFRP laminates | 10 |
| 2.4 | Plastic buckling of an axially loaded tube | 12 |
| 2.5 | Crushing of a cross-ply CFRP laminate | 13 |
| 2.6 | Crushing of three different CFRP laminates | 14 |
| 2.7 | Curved beam under bending load | 15 |
| 2.8 | Simply supported symmetric laminate under double-cosine transverse load | 17 |
| 2.9 | Stresses in beams due to applied transverse displacement | 18 |
| 2.10 | Bending of a delaminated beam | 19 |
| | | |
| 3.1 | Time integration loop used in LS-Dyna | 22 |
| 3.2 | Corotational coordinate system of the BTL element | 24 |
| 3.3 | Design diagram of a new car from initial idea to validation through full scale NCAP tests | 28 |
| 3.4 | Schematic of the routines used for the user shell element modules | 31 |
| | | |
| 4.1 | Opening modes of cracks | 34 |
| 4.2 | Transverse shear stress distribution for different quasi-isotropic layups under an applied shear force | 47 |
| 4.3 | Definition of coordinate system and angles used in Puck's failure theory | 50 |
| | | |
| 5.1 | Stresses in bending beams | 59 |
| 5.2 | Calculation of stresses in case of non-linear material behaviour, with a stress-based failure model calculating the damage by using the undamaged stress | 60 |
| 5.3 | Cantilever plate with two-dimensional delamination | 62 |
| 5.4 | Modelling of a cantilever square plate with a delamination at the corner, brick elements versus plate elements | 63 |

| | | |
|------|---|----|
| 5.5 | Flow chart of all delamination parameters | 64 |
| 5.6 | Example 1 on development of bending stiffness reduction: delamination starting at the corner of a cantilever plate | 65 |
| 5.7 | Example 2 on development of bending stiffness reduction: delamination starting in the middle of the free side of a cantilever plate | 66 |
| 5.8 | Geometrical specifications of the five used FEA models | 68 |
| 5.9 | Results of the cantilever plate without delamination, comparing brick elements to the proposed method using shell elements | 70 |
| 5.10 | Results of the cantilever plate with a one-dimensional delamination, comparing brick elements to the proposed method using shell elements | 71 |
| 5.11 | Results of the cantilever plate with a two-dimensional delamination at a free corner, comparing brick elements to the proposed method using shell elements | 72 |
| 5.12 | Results of the cantilever plate with a two-dimensional delamination almost extending to the whole plate, comparing brick elements to the proposed method using shell elements | 73 |
| 5.13 | Results of the cantilever plate with a two-dimensional delamination from root to tip over half the width of the plate, comparing brick elements to the proposed method using shell elements | 74 |

List of Tables

| | | |
|-----|---|----|
| 2.1 | Specific material properties of typical car frame materials | 4 |
| 2.2 | Mechanical properties IM7/8551-7 | 9 |
| 2.3 | Bending versus membrane properties of quasi-isotropic laminates | 9 |
| 3.1 | Description of subroutines in the user modules of LS-Dyna. | 30 |
| 4.1 | Qualitative comparison of methods to calculate transverse shear and normal stresses | 38 |
| 4.2 | Puck's inclination parameters for typical FRP | 50 |
| 5.1 | Results of the comparison with 3D FEA | 69 |

Nomenclature

Abbreviations

| | |
|----------|--------------------------------------|
| BLT | Belytschko-Lin-Tsay |
| CFRP | Carbon Fibre Reinforced Polymer |
| CLT | Classical Laminate Theory |
| CPT | Classical Plate Theory |
| ESL | Equivalent Single-Layer |
| FEA | Finite Element Analysis |
| FSDT | First-order Shear Deformation Theory |
| GFRP | Glass Fibre Reinforced Polymer |
| LaRC | Langley Research Center |
| NCAP | New Car Assessment Program |
| TSDT | Third-order Shear Deformation Theory |
| WWFE-I | First World-Wide Failure Exercise |
| WWFE-II | Second World-Wide Failure Exercise |
| WWFE-III | Third World-Wide Failure Exercise |
| XFEM | eXtended Finite Element Method |

Symbols

| | |
|----------------------------|------------------------------------|
| α | Fracture plane angle |
| γ | Shear strain |
| $\boldsymbol{\gamma}$ | Out-of-plane shear strain vector |
| ε | Strain |
| $\boldsymbol{\varepsilon}$ | In-plane strain vector |
| ζ | Isoparametric thickness coordinate |
| η | In-plane isoparametric coordinate |
| θ | Cross-sectional rotation |
| ϑ | Ply rotation angle |
| $\boldsymbol{\kappa}$ | Rotation vector |

| | |
|-----------------------|---|
| ν | Poisson ratio |
| ξ | In-plane isoparametric coordinate |
| $\boldsymbol{\sigma}$ | In-plane stress vector |
| σ | Stress |
| $\boldsymbol{\tau}$ | Out-of-plane shear stress vector |
| τ | Shear stress |
| ψ | Action plane resultant shear stress angle |
| $\boldsymbol{\omega}$ | Angular velocity vector |
| \mathbf{A} | Laminate membrane stiffness matrix |
| A | Area |
| \mathbf{a} | Inverse of \mathbf{A} of a symmetric laminate |
| a | Acceleration |
| \mathbf{B} | Laminate coupling matrix |
| \mathcal{B} | Strain-displacement matrix |
| b | Body force |
| \mathbf{C} | Material in-plane stiffness matrix |
| c | Damping coefficient |
| c_γ | Transverse shear strain coefficient |
| \mathbf{D} | Laminate bending stiffness matrix |
| \mathbf{D}^* | Reduced bending stiffness matrix |
| D_f | Delamination free edge flag |
| D_i | Failure index for delamination |
| D_r | Delamination damage factor |
| \mathbf{d} | Inverse of \mathbf{D} of a symmetric laminate |
| \mathbf{d}_σ | In-plane rate of deformation vector |
| \mathbf{d}_τ | Out-of-plane rate of deformation vector |
| d_{ij} | Rate of deformation tensor |
| E | Young's modulus |
| \mathbf{e}_3 | Shell base vector normal to its surface |
| \mathbf{F} | Stress-force resultant matrix |
| f^{ext} | Externally applied force |
| f^{int} | Internal force |
| \mathbf{G} | Material transverse shear stiffness matrix |
| $\bar{\mathbf{G}}$ | Transverse shear stiffness matrix in laminate coordinates |
| $\hat{\mathbf{G}}$ | Transverse shear stiffness matrix in lamina coordinates |
| G | Shear modulus |
| \mathbf{H} | Laminate transverse shear stiffness matrix |
| h | Laminate thickness |
| I | Area moment of inertia |
| \mathcal{K} | Stiffness |
| k | Shear correction factor |
| \mathbf{M} | Moment resultant |
| M | Moment |
| \mathcal{M} | Mass matrix |
| m | Mass |
| \mathbf{N} | Membrane force resultant |

| | |
|--------------------|--|
| p | Inclination parameter |
| p_0 | Applied transverse load |
| $\bar{\mathbf{Q}}$ | Reduced ply stiffness matrix in laminate coordinates |
| $\hat{\mathbf{Q}}$ | Reduced ply stiffness matrix in lamina coordinates |
| \mathbf{R} | Transverse shear force resultant |
| R | Strength |
| r | Radius |
| \mathbf{T}_2 | Transformation matrix |
| \mathbf{T}_3 | Transformation matrix |
| t | Thickness |
| Δt | Time step |
| u | Displacement |
| \mathbf{v} | Velocity vector |
| v | Velocity |
| w | Width |

Subscripts

| | |
|---------------|---|
| \perp | Perpendicular to the fibre direction |
| \parallel | Parallel to the fibre direction |
| b | Bending |
| I | Nodal value |
| L | Longitudinal |
| \mathcal{L} | Linear |
| m | Membrane |
| n | Normal to the action plane |
| $n\psi$ | In the plane perpendicular to the action plane, aligned with ψ |
| \mathcal{P} | Parabolic |
| S | Shear |
| T | Transverse |
| t | Tangential to the fibres |
| 0 | Mid-plane |

Superscripts

| | |
|-----|--------------------|
| c | Compression |
| n | Time step |
| s | Shortened notation |
| t | Tension |

Preface

This thesis is the end product of my labour at the Delft University of Technology (DUT), for the fulfilment of the graduation requirements of Master of Science in Aerospace Engineering. The project has been completed in collaboration with BMW AG, which meant I could showcase my passion for cars and the structural elements of which they are built. In this, I sincerely thank Simon Hesse for the initial contact at BMW, I was never able to get this opportunity if it was not for his positive experience as Delft alumnus at the *Bayerische Motoren Werke*. Having had the opportunity to join the Method Development group at BMW for 6-month internship in Munich, I can only underwrite his positive experiences.

After the first contact was made, my daily supervisors Dr. C. Kassapoglou (DUT) and C. Bögle (BMW) and I had a discussion about the topic of this thesis. Out of four possibilities in the field of the numerical modelling of composites for crash simulations, I chose what was deemed the hardest one with the most uncertainties in the possible solutions to the problem. Even though there were some times in which the uncertainties lead to unforeseen problems, I never regretted choosing for the option in which I could challenge myself the most.

I am grateful for all the people at DUT and BMW who helped me during my thesis. In particular, I would like to thank Dr. C. Kassapoglou and C. Bögle for their daily supervision during my time in Delft and Munich, and their support in each stage of the research and reporting of this project. For my time in Munich, I would like to thank the colleagues at the *Methodenentwicklung* group, who did not hesitate to give me feedback in constructive meetings, which sometimes ended after normal working hours. I would also like to thank my friends Martijn Tra, Marius Knol, Stijn Vial and Bas de Wit for reviewing this report and giving constructive criticism where needed. Last but not least, I would like to thank my friends, family and fellow students for their moral support.

I hope you will enjoy reading this thesis.

Chapter 1

Introduction

The automotive industry faces new challenges as regulatory bodies set harder requirements on the CO₂ emissions of cars, while safety standards are continuously increasing. The most demanding safety standards for a car are to pass crash tests like defined in a New Car Assessment Program (NCAP). These programs are defined by regulatory bodies in various regions, for instance the Euro NCAP by the European Union [1] and the US NCAP by the United States National Highway Traffic Safety Administration [2].

One opportunity to achieve the reduction in emissions, without compromising safety, is reconsidering the choice of material in car frames. For over a century, these have been mainly made out of metal. The geometrical concepts for the frame are therefore highly perfected. This means that for a new car model made of steel, the geometrical concept is set on forehand, the wall thickness of frame elements is usually the first parameter which can be changed. Because of the high level of perfection of the current metal car frames, meeting the emission and safety standards in the future will require a higher use of lightweight materials, one option is to make use of Carbon Fibre Reinforced Polymer (CFRP) in the car frame [3]. These materials are proven to have superior specific stiffnesses, strength and energy absorptions with respect to metals. Using CFRP makes mass savings on the car frame of up to 57% possible [4]; when evaluating the car as a whole, weight savings of 20% or more are expected [5]. However, the European Roadmap Safe Road Transport noted that the lack of numerical finite element crash simulation tools with accurate predictive capabilities prevent the wide-spread use of CFRP in the development of new automobiles [6]. This thesis will cover a part of this lack.

Contrary to isotropic materials such as steel, CFRP is a composite material consisting out of fibres embedded in a matrix, creating a brittle material with failure modes which are vastly different from metals. Furthermore, CFRP is anisotropic, with strength and stiffness parallel to the fibre direction an order of magnitude higher than perpendicular to the fibre direction. To circumvent this issue, laminates can be created by stacking several unidirectional plies on top of each other with different fibre directions. The combination of the freedom in stacking sequence and the complex failure modes of CFRP means that the geometrical concepts perfected for metals may not be the best concepts for frames made of CFRP. Hence, designing a CFRP car frame means an extra design phase is added: concept evaluation.

To evaluate the concepts, numerical tools like Finite Element Analysis (FEA) will be used, both its implicit and explicit form. Implicit FEA can be used to analyse the quasi-static crushing strength of car frame components. Although this is a useful tool, it is not capable of accurately predicting the energy absorption behaviour during dynamic loading like the NCAP tests; for this an explicit FEA code is necessary [7, 8]. In order to be able to evaluate more concepts in a limited time, details will be sacrificed in order to decrease the computational costs. Shell elements can be used when one of the dimensions is at least one order of magnitude smaller than the others. This reduces the number of degrees of freedom and hence reduces the computational cost. Furthermore, the CFRP laminate can be simplified using the Equivalent Single-Layer (ESL) theory, in which the material of a shell is homogenized through the thickness dimension. The combination of the ESL method with shell elements greatly reduces the computational cost when compared to solid element models [9].

One of the problems with homogenising a whole CFRP laminate through thickness, is that the failure modes are dependent on the differences in material characteristics through thickness. To tackle this problem, a new material model is being developed at BMW AG for the implementation in an explicit FEA code. While anisotropy in stiffness is easily implemented in FEA, the different failure modes of CFRP laminates need development. In this thesis the main focus will be on one of those failure modes: delamination. Delamination is the separation of a laminate into multiple sublaminates due to interlaminar cracks. For a broader overview of delamination itself, see the reviews by Garg [10] and Senthil et al. [11], and Chapter 2.13 in *Comprehensive Composite Materials* by Pagano and Schoeppner [12].

There are various ways to model delamination of laminates in FEA. One way is the global-local approach [13, 14]: the general global mesh is locally altered to incorporate the delaminated region. The use of changing element types throughout the analysis makes this way computationally very expensive in explicit FEA. Another way of modelling delamination in FEA is to make use of connecting elements (like cohesive zone elements) between two sublaminates [15–17]; if such an element fails, the laminate is delaminated. The use of these elements requires knowledge of the expected location of delamination in advance, and can only model a number of delaminations equal to the number of connecting elements.

While these are the most useful ways to model delamination, they are both computationally too expensive to be used in the new material model [18]. Hence, a new method is needed, leading to the following research question: *How to detect and model delamination of laminated composites in an equivalent single layer model in explicit finite element analysis?*

To give a well-founded answer, this report is structured as follows: first, the basics of composite materials and failure modes are covered in Chapter 2. In Chapter 3, the context of explicit FEA and initial considerations for the concept of the model are presented. Chapter 4 then explains how onset of delamination can be detected. The effects of delamination and how they can be used in an ESL method are described in Chapter 5. Chapter 6 concludes this thesis with a discussion on the model detailed in the previous chapters, and recommendations for future research.

New contributions in this thesis are the accurate calculation of transverse shear stresses in a homogenised material model in explicit FEA using ESL shell elements (see Section 4.1.4) and modelling the most important effects of delamination for the evaluation of new car frame concepts: a reduction in bending stiffness and a reduction in strain due to bending (see Section 5.2).

Behaviour of Composite Structures

In contrast to isotropic materials like metals, carbon fibre composite laminates consist of different anisotropic layers with a high directional differences in stiffness and strength. This may lead to totally different failure mechanism as known from ductile metals. One of these failure modes is delamination. To have a better understanding of the underlying topics regarding the research question, this chapter serves as background information on composite laminates and the delamination failure mode, with emphasis on the implementation in finite element analysis. The reader is referred to Daniel and Ishai [19] or Hahn and Tsai [20] for a more in-depth explanation on the engineering mechanics of composite materials.

To give a brief overview of this chapter, Section 2.1 starts of with a description of the components of the composite material and how a laminate is built up. Section 2.2 follows with the description of the First-order Shear Deformation Theory (FSDT), a theory which can be used for the analysis of composite structures. Section 2.3 then explains failure modes of composites on micro-level. How they can interact with each other in the case of a car crash is explained in Section 2.4. Since delamination is the failure mode of interest for this thesis, Section 2.5 closes the chapter with an in-depth analysis of its causes and effects.

2.1 Basics of Composite Materials

Composite materials owe their name due to their composition of two different materials. In the case of CFRP, the first component is the carbon fibre, which is stiff and strong in one direction. The second component is the weaker isotropic polymer, in which the fibres are embedded. If designed properly, the result is a composite whose mechanical properties are superior to those of the separate materials. In the case of CFRP, the fibres are the load bearing component of the composite, with their stiffness and strength one to two orders of magnitude higher than those of the matrix. The matrix then binds the fibres together, transferring the load between them and providing protection of the fibres against wear and chemicals. Comparison of specific properties of typical aluminium, steel, CFRP laminates and the bare components of CFRP as used in car frames can be found in Table 2.1.

Table 2.1: Specific material properties of typical car frame materials

| Material | ρ $\left(\frac{\text{kg}}{\text{m}^3}\right)$ | $\frac{E_{11}}{\rho}$ $\left(\frac{\text{m}^3\text{MPa}}{\text{kg}}\right)$ | $\frac{E_{22}}{\rho}$ $\left(\frac{\text{m}^3\text{MPa}}{\text{kg}}\right)$ | $\frac{R_{11,ult}}{\rho}$ ¹ $\left(\frac{\text{m}^3\text{kPa}}{\text{kg}}\right)$ | $\frac{R_{22,ult}}{\rho}$ ¹ $\left(\frac{\text{m}^3\text{kPa}}{\text{kg}}\right)$ |
|--|---|--|--|---|---|
| Aluminium 6101 T6 [21] | 2680 | 25.7 | 25.7 | 74.6 | 74.6 |
| Steel DP980 [22] | 7870 | 26.7 | 26.7 | 127 | 127 |
| Polymer 3501-6 [23] | 1265 | 3.32 | 3.32 | 54.5 | 54.5 |
| Carbon fibre AS4 [23] ² | 1790 | 126 | - | 1872 | - |
| AS4/3501-6 Unidirectional [23] ³ | 1580 | 79.7 | 6.96 | 1234 | 30.4 |
| AS4/3501-6 Quasi-isotropic [24] ³ | 1580 | 31.7 | 31.7 | 412 | 412 |

¹ Strength values are tensile test results of ambient conditions on room temperature.

² Note that carbon fibres cannot be used effectively as a stand-alone material; they need a matrix for stabilization and provide load transfer between the fibres.

³ The composite laminates had a fibre volume content of 60%.

A single carbon fibre has a diameter of 5 to 10 micrometer. To increase the manufacturability of CFRP, the thin carbon fibres are bundled together to form strands several thousands of fibres. The amount of fibres per strand is known as the tow count, which for general applications can vary from 1K (i.e. 1000) to 48K fibres per strand. The heavier tows (i.e. 24K and 48K) have generally slightly lower mechanical properties, however, their lower cost favours them for the use in automotive applications [18]. The resulting strands can then be used to create unidirectional plies, in which all fibres are aligned in a single direction.

The majority of plates used in automotive industry have more than one direction in which stiffness and strength are required. Therefore, several plies are stacked together and bonded such that load transfer between them is possible. This stack of bonded plies is called a laminate, with a characteristic stacking sequence defined by the orientation angle of the plies. An example of the notation to identify the stacking sequence of a laminate is $[0/90/45/-45]_s$, see Figure 2.1. Evaluating this notation from the left to the right, the “0” stands for the outside ply in which the fibres are aligned with the main direction of the laminate. A slash designates the following ply, which in this case is rotated by an angle of 90° with respect to the main direction of the laminate. At the end, the subscript s designates that the base unit of 4 plies between brackets is mirrored after the -45° layer, creating a laminate of 8 plies in total. In this example the single layers are stacked such that the properties of the laminate are equal in all in-plane directions, therefore this laminate is called quasi-isotropic. Furthermore, since mirroring about the mid-plane of the laminate would create a copy of the laminate itself, it is called symmetrical as well.

As can be seen from Table 2.1, the quasi-isotropic laminate performs better than its metal counterparts in terms of specific stiffness and strength. This is however based on test coupons with a fibre volume content of 60%. While it is possible to get such a high value for parts with simple geometries [26], for more sophisticated geometries a fraction of 50% is more likely to be achievable [27]; which would decrease the specific properties of the composite laminates of Table 2.1 by about 15%. However, the real power of composites lies in their ability to

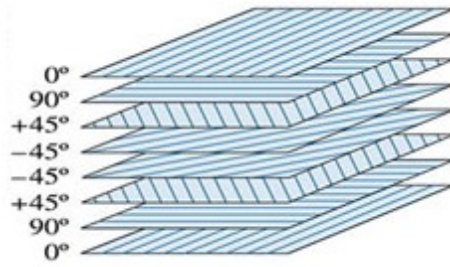


Figure 2.1: Stacking sequence of a $[0/90/45/-45]_s$ laminate [25]

tailor their layup to the loads applied to the structure. This means that for a properly designed CFRP part, the specific properties are in between the values of the unidirectional and quasi-isotropic laminates.

For a more detailed description on the basics of how a composite laminate is built up, the reader is referred to Chapters 1 and 2 of *Engineering Mechanics of Composite Materials* by Daniel and Ishai [19].

2.2 First-Order Shear Deformation Theory

One tool to analytically assess composite structures on their behaviour under load is the FSDT, which will be described in this section. The FSDT, first developed by Reissner [28] and Mindlin [29], is based on the Classical Plate Theory (CPT) of Kirchhoff and Love [30], but relaxes the assumption that plane sections remain perpendicular to the mid-plane. An overview of this plate theory as given by Whitney and Pagano [31] is presented first, followed by the expansion of the theory for composite materials by the same authors in Section 2.2.1. Section 2.2.2 closes the chapter by analysing the assumption of a homogenised material.

The previously mentioned relaxation increases the accuracy for plates which show relatively large shear deformation with respect to bending, which is the case for moderately thick plates and composite plates. It leads to a displacement field as given by Equation (2.1), with strains calculated by Equations (2.2) to (2.6).

$$\begin{bmatrix} u_x \\ u_y \\ u_z \end{bmatrix} = \begin{bmatrix} u_{x0} \\ u_{y0} \\ u_{z0} \end{bmatrix} + z \begin{bmatrix} \theta_y \\ -\theta_x \\ 0 \end{bmatrix} \quad (2.1)$$

With u the displacements and θ the cross-sectional rotations, as visualised in Figure 2.2. Subscript 0 denotes that it is evaluated at mid-plane.

$$\varepsilon_{xx} = u_{x,x} + z\theta_{y,x} \quad (2.2)$$

$$\varepsilon_{yy} = u_{y,y} - z\theta_{x,y} \quad (2.3)$$

$$\gamma_{xy} = u_{x,y} + u_{y,x} + z(\theta_{y,y} - \theta_{x,x}) \quad (2.4)$$

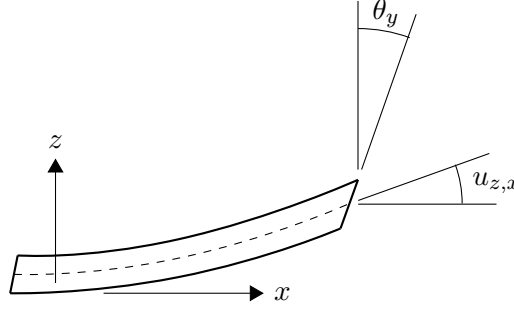


Figure 2.2: Definition of angles used in FSDT in the xz -plane

$$\gamma_{xz} = u_{z,x} + \theta_y \quad (2.5)$$

$$\gamma_{yz} = u_{z,y} - \theta_x \quad (2.6)$$

With ε the strains, γ the shear strains and a comma representing a derivative with respect to (i.e. $u_{z,x} = \frac{\partial u_z}{\partial x}$).

When comparing FSDT with CPT, two new degrees of freedom are introduced: θ_x and θ_y . However, for FSDT all derivatives needed for calculation of the strains are first derivatives, whereas for CPT second derivatives of u_z are needed for calculation of the bending strains in ε_x , ε_y and γ_{xy} . This has a beneficial effect on the computational cost of FEA, as will be explained in the next section on the element formulation.

2.2.1 Expansion for Composite Materials

Just like the Classical Laminate Theory (CLT) expands the CPT for the use with composite laminates, Whitney and Pagano [31] expanded the FSDT for the use of composites. The remainder of this section is based on their work. Since the relaxation of the assumption that plane sections remain perpendicular to the mid-plane does not affect the in-plane stiffness, the in-plane stiffness matrices used in it are equal; the FSDT only adds a transverse shear stiffness matrix. For completeness, they are shown next. First, the reduced ply stiffness matrix $\hat{\mathbf{Q}}$ and the transverse shear stiffness matrix $\hat{\mathbf{G}}$ for an orthotropic material are needed.

$$\hat{\mathbf{Q}} = \begin{bmatrix} Q_{xx} & Q_{xy} & 0 \\ Q_{xy} & Q_{yy} & 0 \\ 0 & 0 & Q_S \end{bmatrix} = \begin{bmatrix} \frac{E_{LL}}{1-\nu_{LT}\nu_{TL}} & \frac{\nu_{LT}E_{TT}}{1-\nu_{LT}\nu_{TL}} & 0 \\ \frac{\nu_{LT}E_{TT}}{1-\nu_{LT}\nu_{TL}} & \frac{E_{TT}}{1-\nu_{LT}\nu_{TL}} & 0 \\ 0 & 0 & G_{LT} \end{bmatrix} \quad (2.7)$$

$$\hat{\mathbf{G}} = \begin{bmatrix} G_{LT} & 0 \\ 0 & G_{TT} \end{bmatrix} \quad (2.8)$$

In which E is the Young's modulus, ν the poisson ratio (first subscript symbol is the load applied, second is the effect) and G the shear modulus. Furthermore, subscript L denotes longitudinal, T transverse and S shear. To obtain the stiffness matrices in the laminate

coordinate system, $\bar{\mathbf{Q}}$ and $\bar{\mathbf{G}}$, these need to be rotated by an angle ϑ . This is done in Equations (2.9) and (2.10).

$$\bar{\mathbf{Q}} = \mathbf{T}_3 \hat{\mathbf{Q}} \mathbf{T}_3^T \quad (2.9)$$

$$\bar{\mathbf{G}} = \mathbf{T}_2 \hat{\mathbf{G}} \mathbf{T}_2^T \quad (2.10)$$

With \mathbf{T}_3 and \mathbf{T}_2 the transformation matrices, given by Equations (2.11) and (2.12), respectively.

$$\mathbf{T}_3 = \begin{bmatrix} \cos^2(\vartheta) & \sin^2(\vartheta) & 2\cos(\vartheta)\sin(\vartheta) \\ \sin^2(\vartheta) & \cos^2(\vartheta) & -2\cos(\vartheta)\sin(\vartheta) \\ -\sin(\vartheta)\cos(\vartheta) & \sin(\vartheta)\cos(\vartheta) & \cos^2(\vartheta) - \sin^2(\vartheta) \end{bmatrix} \quad (2.11)$$

$$\mathbf{T}_2 = \begin{bmatrix} \cos(\vartheta) & -\sin(\vartheta) \\ \sin(\vartheta) & \cos(\vartheta) \end{bmatrix} \quad (2.12)$$

The stiffness matrices in laminate coordinates can now be used to construct the laminate membrane stiffness matrix \mathbf{A} , laminate coupling matrix \mathbf{B} , laminate bending stiffness matrix \mathbf{D} and laminate transverse shear stiffness matrix \mathbf{H} , which are shown in Equations (2.13), (2.14), (2.15) and (2.16), respectively.

$$\mathbf{A} = \int_{-h/2}^{h/2} \bar{\mathbf{Q}} dz \quad (2.13)$$

$$\mathbf{B} = \int_{-h/2}^{h/2} \bar{\mathbf{Q}} z dz \quad (2.14)$$

$$\mathbf{D} = \int_{-h/2}^{h/2} \bar{\mathbf{Q}} z^2 dz \quad (2.15)$$

$$\mathbf{H} = \int_{-h/2}^{h/2} \bar{\mathbf{G}} dz \quad (2.16)$$

In which h is the total thickness of the laminate. Finally, this leads to the relation between force and moment resultants and strains, as given by Equations (2.17) and (2.18).

$$\begin{bmatrix} \mathbf{N} \\ \mathbf{M} \end{bmatrix} = \begin{bmatrix} \mathbf{A} & \mathbf{B} \\ \mathbf{B} & \mathbf{D} \end{bmatrix} \begin{bmatrix} \boldsymbol{\varepsilon}_0 \\ \boldsymbol{\kappa} \end{bmatrix} \quad (2.17)$$

$$\mathbf{R} = k\mathbf{H}\boldsymbol{\gamma} \quad (2.18)$$

With the vectors

$$\boldsymbol{\varepsilon}_0 = [\varepsilon_{xx0} \quad \varepsilon_{yy0} \quad \gamma_{xy0}]^T$$

$$\begin{aligned}\boldsymbol{\kappa} &= [\theta_{y,x} \quad -\theta_{x,y} \quad \theta_{y,y} - \theta_{x,x}]^T \\ \boldsymbol{\gamma} &= [\gamma_{xz} \quad \gamma_{yz}]^T\end{aligned}$$

Furthermore, \mathbf{N} is the membrane force resultant, \mathbf{M} the moment resultant and \mathbf{R} the transverse shear force resultant, given by Equations (2.19), (2.20) and (2.21), respectively. Finally, k is the shear correction factor, usually taken as $k = 5/6$ for isotropic plates [28]. While this might be a material constant for metals, Whitney [32] indicated that it is a function of (at least) the layup of a composite laminate. The shear correction factor is needed to compensate for the fact that a constant shear angle through thickness is assumed, which violates local stress equilibrium at unloaded top and bottom surfaces of the laminate.

$$\mathbf{N} = \int_{-h/2}^{h/2} \boldsymbol{\sigma} dz \quad (2.19)$$

$$\mathbf{M} = \int_{-h/2}^{h/2} \boldsymbol{\sigma} z dz \quad (2.20)$$

$$\mathbf{R} = \int_{-h/2}^{h/2} \boldsymbol{\tau} dz \quad (2.21)$$

With the vectors

$$\begin{aligned}\boldsymbol{\sigma} &= [\sigma_{xx} \quad \sigma_{yy} \quad \tau_{xy}]^T \\ \boldsymbol{\tau} &= [\tau_{xz} \quad \tau_{yz}]^T\end{aligned}$$

and σ and τ the stress and shear stress, respectively.

2.2.2 Stiffness of the Homogenised Material Model

This section explains what the assumption of a homogenised material through thickness means for the material properties to be used, focussing on the stiffness.

For CFRP, the equivalent in-plane stiffness can be calculated as membrane stiffness using Equations (2.22) to (2.24), or bending stiffness using Equations (2.25) to (2.27) [20].

$$E_{11m} = \frac{1}{h\mathbf{a}_{11}} \quad (2.22)$$

$$E_{22m} = \frac{1}{h\mathbf{a}_{22}} \quad (2.23)$$

$$G_{12m} = \frac{1}{h\mathbf{a}_{33}} \quad (2.24)$$

In which \mathbf{a} is the inverse of the laminate membrane stiffness matrix \mathbf{A} . Next to that, subscript m denotes membrane properties.

$$E_{11b} = \frac{12}{h^3\mathbf{d}_{11}} \quad (2.25)$$

Table 2.2: Mechanical properties IM7/8551-7 [33]

| Property | Value | Property | Value |
|----------------|-------|------------------|-------|
| E_{11} (GPa) | 165 | R_{22}^t (MPa) | 73 |
| E_{22} (GPa) | 8.4 | R_{22}^c (MPa) | 185 |
| E_{33} (GPa) | 8.4 | R_{33}^t (MPa) | 63 |
| G_{12} (GPa) | 5.6 | R_{33}^c (MPa) | 185 |
| G_{13} (GPa) | 5.6 | R_{13} (MPa) | 90 |
| G_{23} (GPa) | 2.8 | R_{23} (MPa) | 57 |
| ν_{12} | 0.34 | t_{ply} (mm) | 0.125 |
| ν_{13} | 0.34 | ν_{23} | 0.5 |

$$E_{22b} = \frac{12}{h^3 \mathbf{d}_{22}} \quad (2.26)$$

$$G_{12b} = \frac{12}{h^3 \mathbf{d}_{33}} \quad (2.27)$$

In which \mathbf{d} is the inverse of the laminate membrane stiffness matrix \mathbf{D} . Furthermore, subscript b denotes bending properties. Both \mathbf{A} and \mathbf{D} can be obtained through FSDT.

To further understand the effects the homogenization has on the stiffness of laminates, a comparison is made on six eight-layered quasi-isotropic laminates. According to the FSDT the in-plane stiffness of these three layups is identical. However, due to the different stacking sequences, the bending stiffness is different. Using a standard CFRP material as given by Table 2.2, the results for bending over membrane stiffness ratios are given by Table 2.3. While the three layups show high differences in their bending behaviour, homogenizing the material using the membrane stiffness will lead to incorrect behaviour in bending. Vice-versa, using the bending stiffness in the homogenization will lead to incorrect membrane behaviour. Hence, using the CLT or FSDT for homogenizing the material will need knowledge on the load case on forehand to approach the real stiffness of a plate as close as possible.

2.3 Failure Modes of Composites on Micro Scale

The composite material model which this thesis is part of, will mainly be used in the computational analysis of impacts of cars. In such an event, the kinetic energy of the car has to

Table 2.3: Bending versus membrane properties of quasi-isotropic laminates

| Layup | $\frac{E_{11b}}{E_{11m}}$ | $\frac{E_{22b}}{E_{22m}}$ | $\frac{G_{12b}}{G_{12m}}$ |
|-------------------|---------------------------|---------------------------|---------------------------|
| $[0/90/45/-45]_s$ | 1.65 | 0.94 | 0.41 |
| $[90/0/45/-45]_s$ | 0.94 | 1.65 | 0.41 |
| $[0/45/-45/90]_s$ | 1.68 | 0.37 | 0.77 |
| $[90/45/-45/0]_s$ | 0.37 | 1.68 | 0.77 |
| $[45/-45/0/90]_s$ | 0.59 | 0.44 | 1.46 |
| $[45/-45/90/0]_s$ | 0.44 | 0.59 | 1.46 |

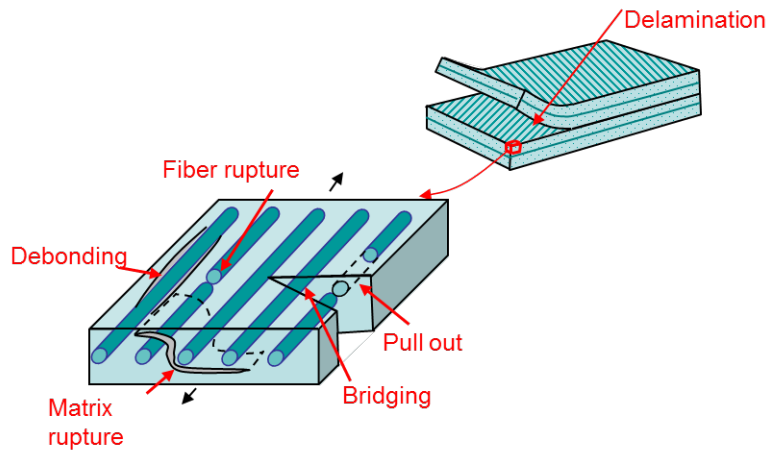


Figure 2.3: Failure modes of CFRP laminates [35]

be absorbed by its frame. The decelerations of the car should be kept to certain limits as defined in NCAPs in order to decrease the injuries of the occupants of the car. In composites, a weight-effective way to do this is by composite crushing. This is a laminate failure mode, which in turn is a combination of failures on a micro-level. In order to have a better understanding of these, this section describes four of these failure modes; fibre failure, interfacial debonding, matrix fracture and delamination in Sections 2.3.1 to 2.3.4. All four sections are based on Chapter 3 of *Damage and Failure of Composite Materials* by Talreja and Singh [34], unless specified otherwise. For a visualisation of the failure modes, see Figure 2.3.

2.3.1 Failure of Fibres

For a properly designed laminate, the final failure (separation) of CFRP ultimately comes from breaking of all fibres on a cross-section. For the case of a tensile loaded composite, fibres first break at the weakest point, which causes a redistribution of load via the matrix to other fibres. This redistribution may then cause new failure of fibres if the stress exceeds the strength of the affected fibres. The strength of each individual fibre is of a statistical nature because of manufacturing processes of the fibres themselves and the processes of manufacturing a composite structure. Therefore, the number of fibre breaks per unit volume is higher in the vicinity of a crack tip and reduces as the distance to the crack tip increases. Because of the difference in stiffness and strength between matrix and fibres, the main parameters influencing the magnitude of absorbed energy in this failure mode are the stiffness and strength of the fibres.

In the case of a compressive loaded composite, fibre failure is characterised by kinking of the fibres on micro level and is therefore known as the microbuckling of fibres. During the manufacturing processes of a composite structure, misalignment of fibres on micro level is inevitable. Therefore, idealizations of perfectly aligned fibres cannot be used in analysis of this type of buckling, as misalignments of even a few degrees tend to give inaccurate buckling loads. Next to the properties of the fibres, also the stiffness and strength of the matrix influence the amount of energy absorbed in this failure mode.

2.3.2 Interfacial Debonding

A primary factor in the mechanical performance of composite laminates is the quality of the interface between the fibres and the matrix. This interfacial bond secures the transfer of load between the two components of the composite material. Considering the strength of the interface in the fibres and the matrix, a weak bond results in matrix cracks at relatively low stresses. On the other hand, a bond which is too strong could cause a catastrophic failure of the composite once the matrix cracks, as the fibres will crack simultaneously. Controlling the bond strength is thus essential in creating a composite with optimal mechanical performance and maximum potential on absorbed energy.

According to Daniel and Ishai [19], a stress concentration in the interface is needed to cause failure in it, combined with a relatively weak interface when comparing to the matrix strength. They mention two main sources of stress concentration in the interface:

- For a ply tensionally loaded along the fibre direction, a single failed fibre causes stress concentrations in the interface since the load which was carried by this fibre, has to be transferred to other fibres
- For a ply loaded perpendicular to the fibre direction (both in tension and compression), as well as plies loaded in shear, the difference in stiffness of the fibre and matrix will cause the stress concentration

2.3.3 Matrix Fracture

As can be seen from Table 2.1, CFRP offer high stiffness and strength in the direction parallel to the fibres (1-direction). However, in the direction perpendicular to the fibres (2-direction), the matrix is dominant in providing the mechanical properties of the composite and hence the magnitude of these are lower. As a result, cracks tend to develop in the matrix along the fibres as first failure in a composite laminate. For laminates containing plies with different fibre orientations, these cracks can start in a given ply at a defect, progress to neighbouring plies and grow along the fibres in these plies. Defects include interfacial debonds and voids and inclusions due to manufacturing. Even though intralaminar matrix fracture itself does not cause structural failure, the effects can be significant, including considerable degradation in material stiffness. Furthermore, intraply matrix crack can induce more severe forms of damage, such as fibre failure and delamination. Even though the matrix strength and stiffness are low when compare to the properties of the fibres, the amount of absorbed energy can be significant because of the large crack area.

2.3.4 Delamination

A crack between two plies of a laminate which causes a separation between those plies is called delamination. Next to the earlier mentioned intraply cracks, delaminations in composite laminates can start at free edges, curvatures and changes in cross-sections. They can also be the result of a low-velocity impact. The effects of delamination are a reduced compressive strength and a reduction in membrane and bending stiffness. Visual inspection cannot be used in all cases to detect delamination, as the surface may appear undamaged while a

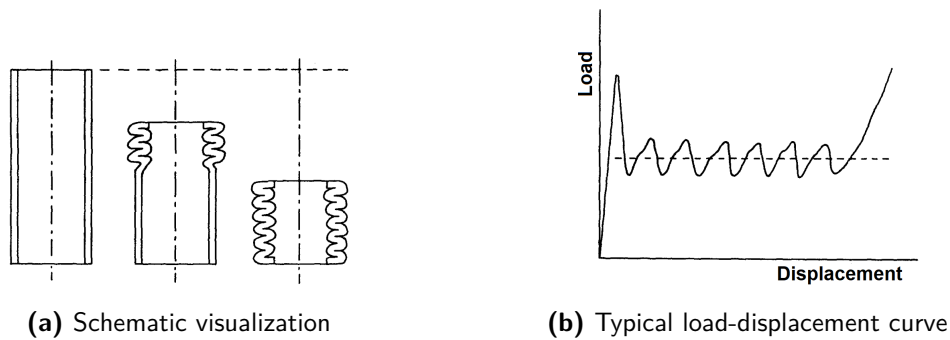


Figure 2.4: Plastic buckling of an axially loaded tube [40]

delamination has started. For a more in-depth analysis of the delamination failure mode, the reader is referred to Section 2.5.

2.4 Laminate Failure in In-Plane Impact Events

In contrast to metals structures, which generally collapse by plastic buckling in in-plane impact events [36], most composite structures collapse by a combination of the fracture processes described in the previous section [37, 38]. The actual interaction between these processes is highly dependent on the geometry of the structure, lamina orientation, type of trigger and crush speed, all of which can be suitably designed to develop high energy absorbing mechanisms [39].

The fact that plastic buckling is still possible for some specific composite structures, is described in Section 2.4.1. However, the preferred laminate failure mode in impact events is composite crushing, which is described in Section 2.4.2.

2.4.1 Plastic Buckling of Composites

The plastic buckling failure mechanism of tubes involves successive locally buckled tube sections, such that the tube folds axially similar to the folding of an accordion, see the schematics of Figure 2.4a. The corresponding load-displacement curve, shown in Figure 2.4b, shows three distinguishable parts, each corresponding to one of the three schematics. First, the tube compresses linear-elastically up to a peak load before dropping to a mean crushing load. In the second part, the load oscillates about a mean crush level in which each period corresponds to the formation of one new fold in the tube. Once no new folds can be created in the tube, the load rises rapidly in the final part.

The plastic buckling failure mode is typical for composites tubes based on aramid fibres, as these exhibit plastic yielding in case of compressive failure, instead of fracture seen in composites based on brittle fibres (like glass or carbon) [41–43]. There are cases known for which composites based on brittle fibres do exhibit the plastic buckling failure mode. Farley and Jones [44] identified three requirements for composites based on brittle fibres to exhibit plastic buckling:

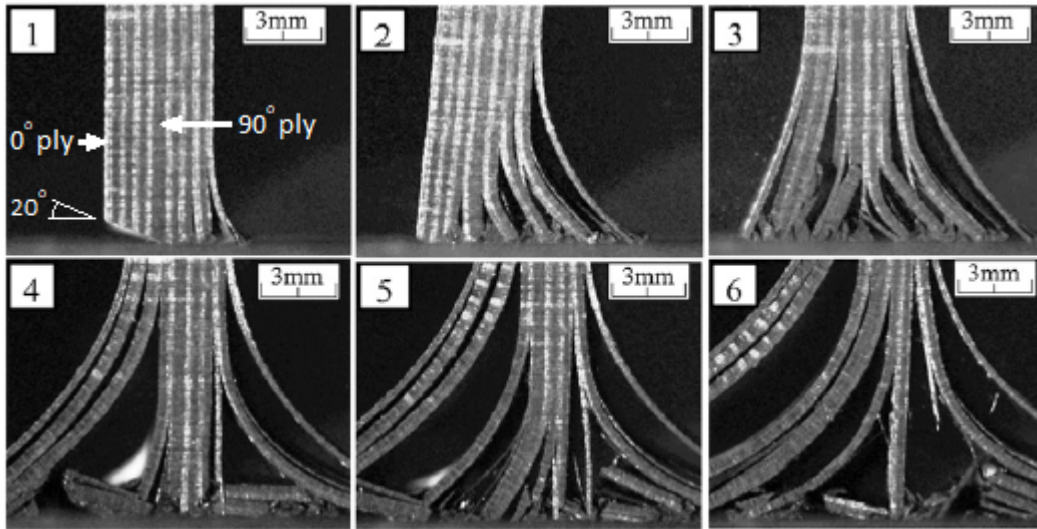


Figure 2.5: Sequence of images visualising the crushing of a $[0/90]_{4s}$ CFRP laminate [45]

1. The interlaminar stresses are small relative to the strength of the matrix
2. The matrix has a higher failure strain than the fibre
3. The matrix exhibits plastic deformation under high stress

However, Farley and Jones noted that this mode of failure is generally an inefficient one for thin-walled specimens, favouring the composite crushing mode as described in the next section.

2.4.2 Composite Crushing

Composite crushing is defined as the result of a combination of several failure mechanisms, such as matrix cracking, delamination and fibre tensile and compressive fracture, leading to a progressive brittle failure in a composite under an axial compressive force. How all different failure modes interact with each other during composite crushing is explained by using several of the tests of Israr et al. [45]. The first test was on the crushing of a $[0/90]_{4s}$ laminate, photographs of the progressive crushing are shown in Figure 2.5. The plate was given a 20° chamfer at the impact surface to create a progressive crash front, see image 1 of Figure 2.5.

From the beginning to image 1, the tip of the specimen crushes. The outermost ply delaminates and has a combination of interfacial debonding and matrix cracks, as can also be seen from the splitting of the outer 0° ply on the right hand side of image 1. Continuing to image 2, more delaminations appear, creating several $[0/90]$ sublaminates. After image 2, parts of the laminate begin fragmentation, which is the separation of small parts of the laminate, completely losing the load bearing capability for the remaining structure. During fragmentation, fibres break in the 0° plies due to excessive bending (tensile failure) or microbuckling (compressive failure). In the 90° plies, the matrix fractures as a result of losing the load carrying ability of the connected 0° plies. As the crushing progresses from image 3 to 6, the delamination grows such that fragmentation decreases and most of the sublaminates bend, creating larger fragments.

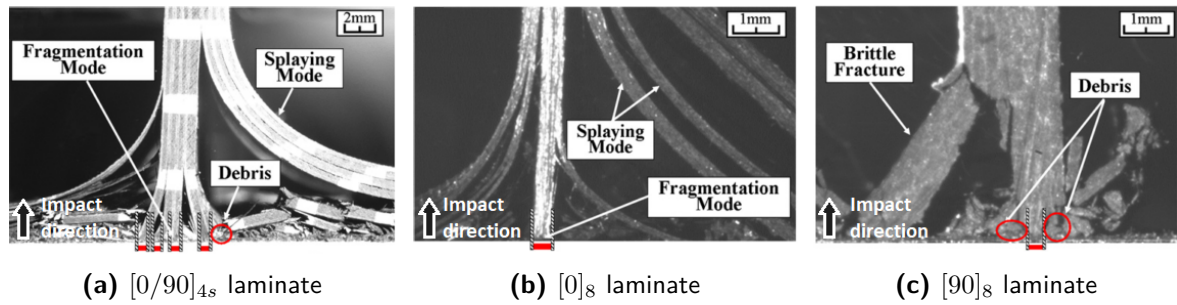


Figure 2.6: Crushing of three different CFRP laminates. Red lines indicate the thickness of the laminate in pure fragmentation mode [45]

Figure 2.6 shows photographs of three more tests at the stage of full crushing; i.e. the stage of images 4 to 6 of Figure 2.5. Note that these three laminates have a chamfer angle of 45° . When comparing Figure 2.6a to image 4 of Figure 2.5, the difference in chamfer angle results in comparable crushing behaviour. This is not the case for the crushing of a $[0]_8$ laminate, as can be seen from Figure 2.6b. It exhibits more splaying than the cross-ply laminate, resulting in a smaller part of the laminate which fails by fragmentation; 9 out of 16 plies for the cross-ply laminate versus approximately 2 out of 8 plies for the uni-directional laminate.

Comparing Figure 2.6c to Figure 2.5, the failure modes interact differently with each other for the transverse uni-directional laminate as well. Since no fibres are in the direction of movement of the impacted surface, the stiffness and strength in this direction are low. This causes smaller delaminations and fragment sizes. Furthermore, minimal fibre breakage was reported, as the stress in the fibres is relatively small. Hence, matrix failure and delaminations are dominant in this crushing test. Since the way the failure modes interact with each other is different for the three presented cases, it is concluded that the layup of a laminate influences this interaction. The exact manner in which the material parameters (like strengths, failure strains, stacking sequences) influence the crushing process is not fully understood yet.

2.5 Delamination

As concluded from the previous section, delamination plays a major role in the crushing of composites. However, not only in crushing does delamination occur, it can also have other causes, as can be read in Section 2.5.1. The effects of delamination on a structural level follow in Section 2.5.2.

2.5.1 Causes of Delamination

Delaminations start when the transverse stresses on the interface between plies become higher than the strength of this interface. Due to the anisotropic nature of CFRP, there are more causes for transverse stresses than for metals. Curvatures, free edges, changes in cross-sections and applied transverse loads can all give rise to these stresses [46]. Each of them is shortly explained below.

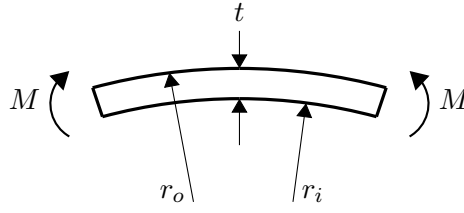


Figure 2.7: Curved beam under bending load

Curvatures

Delamination due to curvature could be best explained using a simple beam. If a curved beam is bent such that the deformation is in the opposite direction as the initial curvature (see Figure 2.7), the layers near the inner surface will tend to straighten out. The layers near the outer surfaces will keep part of their curvature. This combination leads to a tensile transverse normal stress. The opposite also holds; a loading which leads to an increase in the initial curvature, develops a compressive transverse normal stress in the curved region. To keep local stress equilibrium, transverse shear stresses develop as well. This effect is also present in isotropic material, for which the maximum stress is approximated by Equation (2.28) [47].

$$\sigma_{rr}^{max} = \frac{3M}{2t\sqrt{r_i r_o}} \quad (2.28)$$

In which M is the applied moment (positive direction is shown in Figure 2.7), t is the thickness and r_i and r_o are the radius of curvature of the inner and outer surfaces, respectively. For further reading on this topic, the reader is referred to sections 23 and 24 of Lekhnitskii [48], who developed a theory for the loading of anisotropic curved beams. Webber [49] noted a small error in Lekhnitskii's derivation for the application of a force in the tangential direction and provided a corrected equation for it.

Free-Edge Effects

When laminates are built up from plies of different orientations, general lamination theory implies interlaminar shear is needed to overcome the difference in the elastic constants between layers. However, this indicates a problem at traction-free boundaries, where such shear stress would violate local equilibrium. The first widely accepted model to analyse this problem was developed by Pipes and Pagano [50], which is based on a finite-difference solution technique. The numerical results of this analysis indicated a singularity in the interlaminar shear stress at the intersection of the interface and free-edge. This phenomenon is known as the free-edge effect. The mathematical proof and the strength of the singularity in the transverse shear stresses were later obtained by Wang and Choi [51]. Shalev and Reifsnider [52] performed tests on notched plates of moderate thickness (4 to 5 mm) and showed delaminations due to the free edge effect are likely to occur close to the outer plies of the laminate. For a broader literature review from 1967 to 2004 on this topic, see the review of Mittelstedt and Becker [53].

To overcome the general problem of singular stresses, Whitney and Nuismer [54] introduced an approach to either take the stress at a characteristic length d_0 away from the stress

concentration (point stress), or to take the average stress over a region of length a_0 (averaging stress). When applying either of these approaches to the free edge problem, the characteristic lengths d_0 and a_0 are a function of material and geometrical parameters. Much debate has arisen on the particular parameters influencing these lengths [55–57], including material properties, ply orientation and laminate thickness. It is however generally agreed upon that the free-edge effect is a local effect, only influencing the transverse stresses in the vicinity of a free edge (within a few laminate thicknesses of it).

A different method predicting the transverse stresses due to the edge effect is presented by Kassapoglou [58], based on the principle of minimum complementary energy. Although the method does not predict singular stresses, the agreement when compared to other literature is good up to a few fibre diameters away from the free edge. Two arguments are given for the unimportance of the solution in this small region. First, on this scale the assumption of a homogeneous material would no longer hold. Second, the method will mainly be used to evaluate the stresses for failure. This is generally done using the averaging or point stress approach of Whitney and Nuismer, minimizing the effect this difference has on the resulting delamination strengths.

Changes in Cross-Section

In the case of a change in cross-section, transverse shear stresses are locally needed to redistribute the load. To keep local stress equilibrium, transverse normal stresses are also introduced. Examples of cross-sectional changes are internal and external ply-drops, a stiffener bonded to a skin and doublers.

Since the problem of dropping plies is an inherently three-dimensional problem, no solutions exist to obtain the resulting stresses in an ESL approach. For a stiffener bonded to a skin, a series of studies by Kassapoglou [59–61] showed that local transverse shear stresses of up to 1.5 times the applied in-plane shear stress can be obtained for certain skin-stiffener designs. However, this was found to be a local effect, with the transverse stresses generally vanishing within 10 times the skin laminate thickness. For a broader review on the effect of changes in cross-section on transverse stresses and delamination, see the review of He et al. [62].

Applied Transverse Loads

When a transverse normal load is applied to a composite laminate, transverse stresses are a result. For a simply-supported rectangular composite laminate consisting of only 0° and 90° plies, Pagano [63] developed a general analytical solution. Rohwer [64] used this general solution to construct benchmark results with plates under a double-cosine load on both top and bottom surfaces, see Figure 2.8. The results were transverse shear stresses which are of piece-wise continuous parabolic shape, with no stress at the outer surfaces as no transverse shear is applied. Since the transverse normal load was applied on both surfaces, the transverse normal stress was constant through thickness.

Since the exact solution of Pagano can only be used for simple configurations and lamination schemes, Savoia and Reddy [65] developed a three-dimensional elasticity solution which can be used for more general laminates, including anti-symmetric laminates and laminates with arbitrary ply orientations. Rolfes et al. [66] used this elasticity solution to generate benchmark

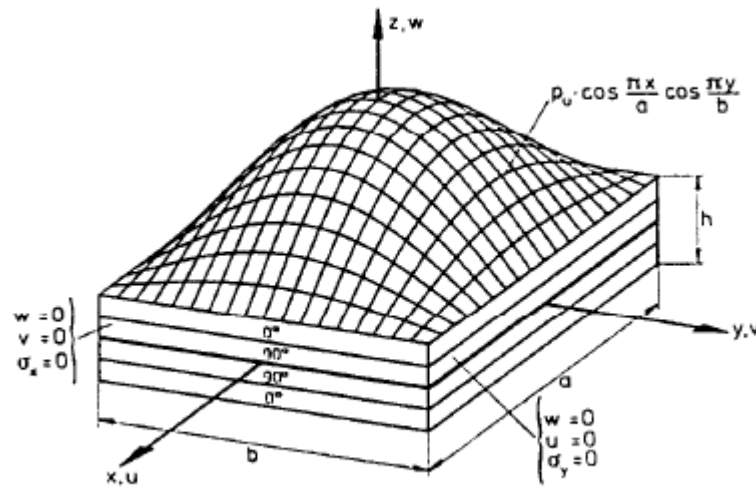


Figure 2.8: Simply supported symmetric laminate under double-cosine transverse load [64]

results for simply supported rectangular plates (i.e. the same as Figure 2.8), however, now only a load was applied on the top surface of the laminate. The results are a piece-wise continuous fourth order equation of z for the transverse normal stress, ranging from 0 at the unloaded bottom surface to the applied stress at the top surface.

2.5.2 Effects of Delamination

Once a delamination exists in a laminate, based on the location and size it can have several structural effects. These can be distinguished into effects on membrane and bending behaviour, as explained below.

Membrane Behaviour

Stalnaker and Stinchcomb [67] performed experiments on plates containing delaminations, caused by fatigue loading. After damage was inflicted, they tested the panels on membrane stiffness and strength. While no change in tensile strength was noted, the tensile stiffness was decreased by up to 13.6% for quasi-isotropic laminates. Building on these results, O'Brien [68] performed stiffness analysis on panels designed to delaminate on their edges and validated this analysis with experiments. Using a rule of mixtures approach, the result was a reduction of 25.8% in membrane stiffness for a totally delaminated panel with layup $[\pm 30/\pm 30/90/90]_s$ with delaminations in both -30/90 interfaces. Kutlu and Chang [69,70] developed an analytical model for compression loading of panels containing multiple delaminations, and validated this with FEA and experiments. Their main conclusions were that buckling of sublaminates is the dominant source of reduction in compression strength of delaminated panels, and multiple delaminations reduce the compression strength more than a single delamination does.

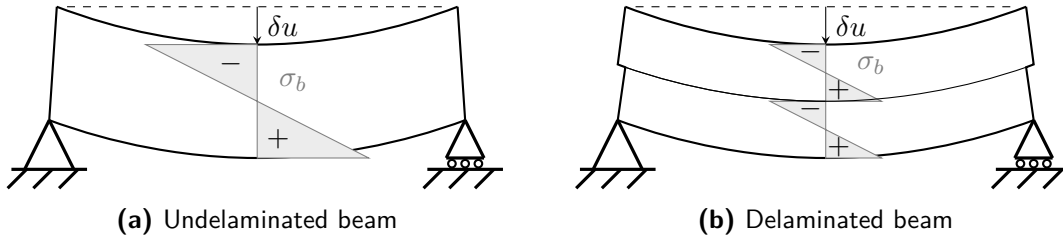


Figure 2.9: Stresses in beams due to applied transverse displacement

Bending Behaviour

To start the description of the effect a delamination has on bending behaviour, first a comparison is made between a cantilever beam and two cantilever beams of half thickness above each other, see Figure 2.9. This is done by calculating the bending stiffness of an isotropic beam, EI , in which E is the Young's modulus and I the area moment of inertia. If a beam is delaminated, its area moment of inertia changes, see Equation (2.29).

$$I = \frac{wt^3}{12} \quad (2.29)$$

With w the width of the beam and t the thickness. Due to the third power of thickness, the inertia of a beam of half thickness is 12.5% of the full thickness beam. However, since there are two halves, the total inertia is 25%. As can be seen from Figure 2.9, not only the stiffness changes, but also the stress distribution through thickness. Since the beam is split in two, each half has its own neutral line. For each half, the maximum distance to the neutral line is halved. Therefore, the maximum stress due to bending for an applied transverse displacement is halved as well.

This can be beneficial for CFRP, as it can delay failure of the outer plies due to bending while keeping the load carrying ability in the in-plane directions. One application of this could be in the firewall between a front-engine and the passenger compartment; a reduction of the bending stiffness due to delaminations would increase the intrusion of the engine into the firewall without the latter being penetrated or failed catastrophically. This in turn increases the effective length of the frontal crumple zone of the car, which in the end leads to a lower average deceleration of the occupants of the car in case of a frontal crash.

Chan and Chou [71] extended the rule of mixtures approach for membrane stiffness as used by O'Brien to the calculation of bending stiffness. Without comparison to other methods or experiments, they obtained reductions in bending stiffness of over 80% for a beam with a single delamination over its full length. One of the essential assumptions made, was that a delamination can be translated in in-plane coordinates without any consequences. That this last assumption is not valid, was shown by Tracy and Pardoen [72]. They used an analytical solution for a one-dimensional mid-plane delamination, not reaching the end of a beam. At the crack tips, axial displacement between the intact segment and the delaminated segments was satisfied. They validated their model using FEA and experiments, with excellent agreement. Looking at the bending stiffness of the whole beam under three-point bending, they concluded that up to 40% delamination, the reduction in stiffness is less than 5%. However, after 40% delamination, the stiffness reduces linearly to 57% of the intact beam, for a 99% delaminated

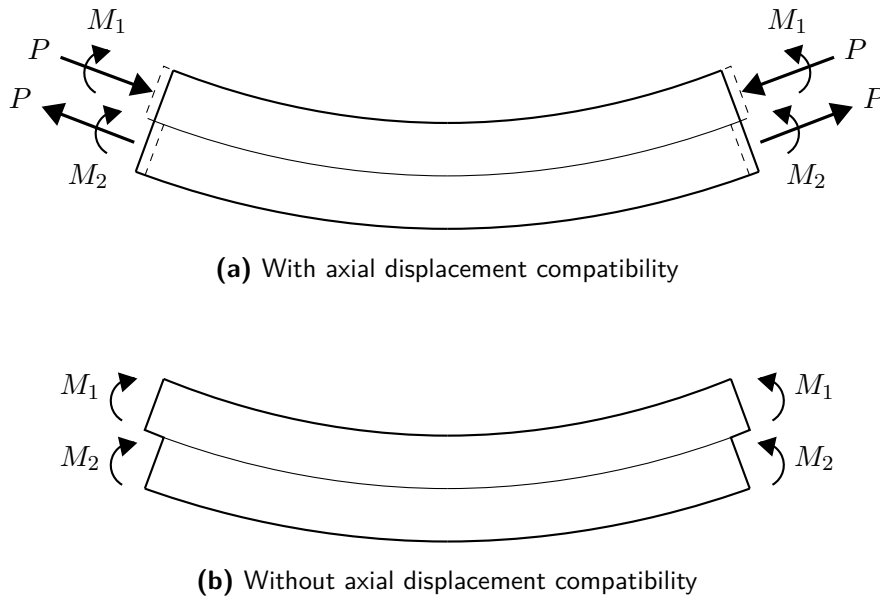


Figure 2.10: Bending of a delaminated beam

beam (the 1% at the end is still capable of load transfer between the halves). Without any shear transfer at the end, a fully delaminated beam would have a reduction in bending stiffness of 75% of the intact beam based on the inertia of two beam halves. In contrast to the reduced bending stiffness for three-point bending, they noted no reduction in bending stiffness for a delaminated beam under four-point bending, as long as there is shear transfer at the end of the beam. Without shear transfer, the stiffness would again be reduced by 75%. Hence, a beam with a delamination of three-quarters of its length at the root has a significant different stiffness than a beam with the same delamination length starting at the tip, invalidating the essential assumption made by Chan and Chou.

The difference as to why a three-point bending beam sees a reduction in bending stiffness, while a four-point bending beam does not, is perhaps best explained by Mujumdar and Suryanarayan [73] and Figure 2.10: at the crack tip, a single beam element is connected to two delaminated beam segments (the sublaminates). Satisfying compatibility of axial displacement at both ends of the crack, creates an additional load system with magnitude P of equal and opposite forces on the delaminated segments. One segment is compressed while the other is stretched, such that their ends lie in the same plane. The effect of this load system gives is a net resultant internal bending moment. Thus the requirement of axial compatibility produces a differential stretching of the delaminated segments which add to the total bending stiffness of the beam in the delamination zone. Looking at the isolated top half of an intact beam under three-point bending, the magnitude of the axial load increases closer to the axial midpoint of the beam. This is made possible by shear transfer to the bottom half. The delaminated beam misses this possibility of shear transfer, which in turn reduces the bending stiffness for larger delaminations. For four-point bending, there is no such increase in load. Hence, no shear transfer is needed between the top and bottom half, leading to no reduction in bending stiffness.

Hou and Jeronimidis [74, 75] identified a local thickness increase for small delaminations created by impacts, when measuring the vibration characteristics of circular plates with centralized, elliptical delaminations. This increase in thickness caused an increase in bending stiffness. Once the size of the delaminations increased above a certain threshold, the effect of local thickening was reduced and a decrease in bending stiffness was observed. However, the magnitude of the changes in bending stiffness was small, the natural frequencies of the delaminated plates were within 5% of the intact plates.

Finite Element Framework and Initial Concept

A delamination failure in a composite will have an effect on the mechanical performance of the whole laminate through thickness, as was shown in Section 2.5.2. In order to see how this can be implemented in an ESL model in explicit FEA, this chapter describes the framework for this thesis on the numerical side. The framework is given through the commercial finite element code LS-Dyna [76]. LS-Dyna is a widely used crash solver in the automotive industry. It has the advantage that essential parts of the code are available for user interface coding. This allows access to most parts of the code, including transformation matrices, material models, etc. Furthermore, the complete element formulation for one of the most efficient elements, the Belytschko-Lin-Tsay (BLT) element, is included in the user interface, which can easily be modified. The combination of using LS-Dyna and the BLT element is a boundary condition for this thesis.

In the BLT element, the thickness direction is represented by making use of several integration points through thickness. Any material law of material model is applied to an integration point, as will be shown in Section 3.5. Since delamination affects the stress distribution of all integration points through thickness, its effects cannot be implemented in a material model alone. Hence, the element formulation and its interaction with the material model are needed as well.

To be able to explain the element and material models, first a brief overview of the explicit solution scheme is covered in Section 3.1. This section is followed by the element formulation in Section 3.2. In Section 3.3 initial considerations for the concept, as basis for this work, are outlined. Section 3.4 continues with describing methods currently used to model delamination in finite element analysis. Section 3.5 finalizes this chapter by explaining the relevant subroutines and identifying possibilities for the implementation of the method.

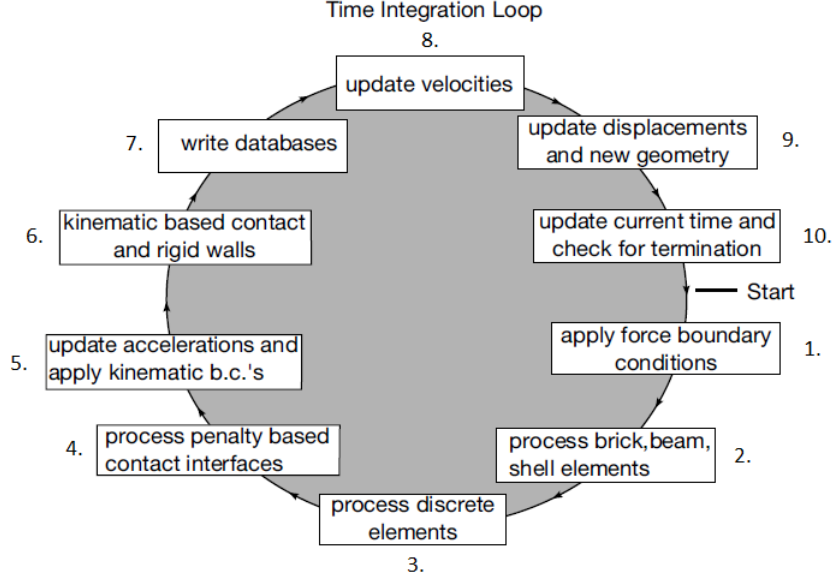


Figure 3.1: Time integration loop used in LS-Dyna [78]

3.1 Explicit Solution Scheme

This section provides a brief overview of the explicit time integration scheme. For the full time integration loop as used by LS-Dyna, see Figure 3.1. Furthermore, the reader is referred to Belytschko et al. [77] for a more in-depth explanation of explicit finite element analysis; this section is an excerpt of it with focus on the parts which are important for this thesis.

The aim of the method is to solve the equation of motion, Equation (3.1), for the whole structure.

$$m\ddot{u} + \underbrace{c\dot{u} + \mathcal{K}u}_{f^{int}} = f^{ext} \quad (3.1)$$

With m the mass, c the damping coefficient, \mathcal{K} the stiffness, f^{ext} the externally applied force and f^{int} the internal force. Furthermore, $\dot{}$ represents a derivative in time, which makes $\dot{u} = v$, the velocity, and $\ddot{u} = a$, the acceleration. Discretising in space and time leads to the discrete equation of motion, as shown in Equation (3.2).

$$\mathcal{M}\mathbf{a}^n = (\mathbf{f}^{ext})^n - (\mathbf{f}^{int})^n \quad (3.2)$$

Due to the discretization in space, the scalars f^{ext} , f^{int} and \ddot{u} become vectors, and m is discretised to the mass matrix \mathcal{M} . Superscript n indicates the time step at which the equation is evaluated. It follows from Figure 3.1 that the external forces are calculated in the first part (apply force boundary conditions) and the internal forces are calculated in parts 2 to 4: based on the displacements obtained in part 9 of the previous time step, first the strains are calculated on each integration point of an element. Using a material model, these strains are then converted into stresses. Finally, these stresses are integrated over the element to

create the internal force vector. Hence, rewriting Equation (3.2) to Equation (3.3) leads to the accelerations at time step n , since all parameters on the right-hand side are known. These are then used in combination with a central-difference time integration to calculate the unknown velocities, Equation (3.4), and displacements, Equation (3.5), at the next time step. This roughly compares to parts 5 to 9 in the integration loop of Figure 3.1.

$$\mathbf{a}^n = \mathcal{M}^{-1} \left((\mathbf{f}^{ext})^n - (\mathbf{f}^{int})^n \right) \quad (3.3)$$

$$\mathbf{v}^{n+1/2} = \mathbf{v}^{n-1/2} + \mathbf{a}^n \Delta t^n \quad (3.4)$$

$$\mathbf{u}^{n+1} = \mathbf{u}^n + \underbrace{\mathbf{v}^{n+1/2} \Delta t^{n+1/2}}_{\Delta \mathbf{u}} \quad (3.5)$$

In which Δt is the time step, which is updated in the last step of the integration loop. $\Delta t^{n+1/2}$ is the average of Δt^n and Δt^{n+1} .

The process of calculation of stresses, forces, moments and failure is all part of the calculation of f^{int} , in particular in the step of processing brick, beam and shell elements. To know how this processing is done, the following section will look into the shell element formulation used in crash analyses.

3.2 Belytschko-Lin-Tsay Shell Element

The main shell element used in explicit FEA is the Belytschko-Lin-Tsay (BLT) element, especially in dynamic problems [78]. This element is computationally efficient due to the combination of a corotational and velocity strain formulation. These two concepts are explained in Sections 3.2.1 and 3.2.2, followed by the method of calculating the stresses inside the element in Section 3.2.3. These sections are based on the description of the original developers of the element; see Belytschko, Lin and Tsay [79]. The element is based on the FSDT as described in Section 2.2, however, it does not include Whitney and Pagano's expansion of it for the use of composites [31]. Therefore, the analysis inside an element is done assuming one layer of material through the thickness. This means, for instance, that $\bar{\mathbf{Q}}$ and $\bar{\mathbf{G}}$ as used in Equations (2.13) to (2.16) are constant through thickness. However, the material can be orthotropic, and under an angle ϑ .

3.2.1 Corotational Formulation

One characteristic of explicit FEA is that thousands of time steps are used to deal with dynamic problems, which means non-linear geometrical and material behaviour. When using a fixed coordinate system, difficulties may arise of expressing physical properties in an element. Therefore, the BLT element has a coordinate system embedded in the element, see Figure 3.2. The mid-plane of the element acts as a reference plane of the coordinate system, which reduces the effort needed to calculate orthotropic material properties in the element.

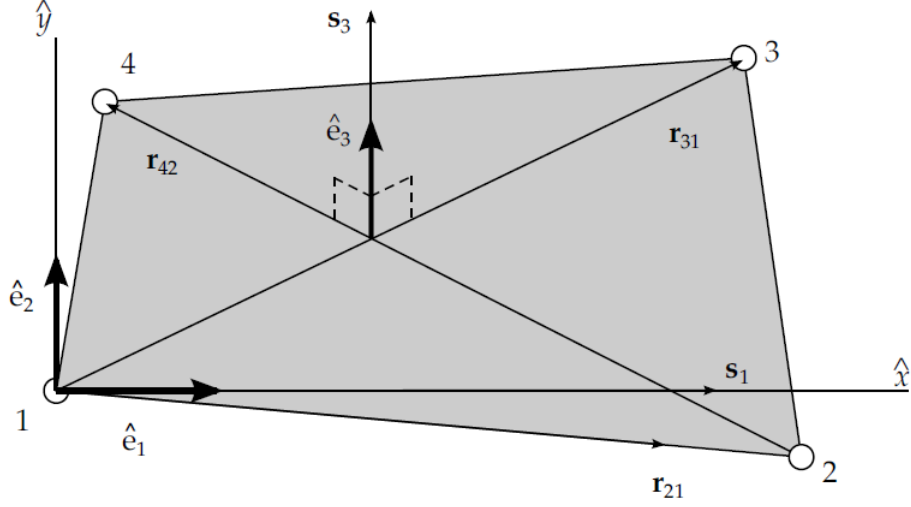


Figure 3.2: Corotational coordinate system of the BTL element [78]

3.2.2 Velocity Strain Formulation

To be able to analyse dynamic behaviour, the BLT element uses a velocity strain formulation. In a certain time step, this means that the time derivative of the strains are calculated first, which are then multiplied by the size of the time step to get an increase in strain. To be able to do this, first the velocity of a point in the element is defined as Equation (3.6), which is the time derivative of Equation (2.1).

$$\mathbf{v} = \mathbf{v}_0 - z\mathbf{e}_3 \times \boldsymbol{\omega} \quad (3.6)$$

With \mathbf{v} the velocity vector, \mathbf{e}_3 the shell base vector normal to its surface and $\boldsymbol{\omega}$ the angular velocity vector. Similarly to Equations (2.2) to (2.6), the rate of deformation tensor components d_{ij} are given by Equations (3.7) to (3.11).

$$d_{xx} = v_{x,x} + z\omega_{y,x} \quad (3.7)$$

$$d_{yy} = v_{y,y} - z\omega_{x,y} \quad (3.8)$$

$$d_{xy} = v_{x,y} + v_{y,x} + z(\omega_{y,y} - \omega_{x,x}) \quad (3.9)$$

$$d_{xz} = v_{z,x} + \omega_y \quad (3.10)$$

$$d_{yz} = v_{z,y} - \omega_x \quad (3.11)$$

Note that these relations are evaluated at the integration point, which is in the middle of the element. The BLT element uses standard bilinear isoparametric interpolation to determine the mid-plane element coordinates, angular velocities and mid-surface velocities, see Equations (3.12) to (3.15).

$$\mathbf{x}_0(\xi, \eta) = \sum_{I=1}^4 N_I(\xi, \eta) \mathbf{x}_I \quad (3.12)$$

$$\mathbf{v}_0(\xi, \eta) = \sum_{I=1}^4 N_I(\xi, \eta) \mathbf{v}_I \quad (3.13)$$

$$\boldsymbol{\omega}(\xi, \eta) = \sum_{I=1}^4 N_I(\xi, \eta) \boldsymbol{\omega}_I \quad (3.14)$$

$$\begin{aligned} N_1 &= \frac{1}{4}(1-\xi)(1-\eta); & N_2 &= \frac{1}{4}(1+\xi)(1-\eta); \\ N_3 &= \frac{1}{4}(1+\xi)(1+\eta); & N_4 &= \frac{1}{4}(1-\xi)(1+\eta) \end{aligned} \quad (3.15)$$

With subscript I denoting the nodal values. Furthermore, ξ and η are the in-plane isoparametric coordinates, ranging from -1 to 1. The BLT element uses one integration point in in-plane coordinates, at $\xi = \eta = 0$.

The use of the FSDT in the BLT element has as beneficial effect that only first derivatives of the velocities are needed to calculate the strains inside an element. This allows for the use of only 4 nodes to construct the full internal force vector. This greatly increases the computational efficiency when compared to an element based on CPT, where second derivatives are needed to calculate all strains. Hence, parabolic shape functions are needed, requiring at least 8 nodes for a quadrilateral element.

3.2.3 Stress and Force Calculation

In the BLT element in its original formulation, the stresses are calculated using Equations (3.16) to (3.19), distinguishing between the membrane behaviour in $\boldsymbol{\sigma}$ and the transverse shear behaviour in $\boldsymbol{\tau}$.

$$\boldsymbol{\sigma}^{n+1} = \boldsymbol{\sigma}^n + \Delta t \left(\dot{\boldsymbol{\sigma}}^{n+1/2} \right) \quad (3.16)$$

$$\boldsymbol{\tau}^{n+1} = \boldsymbol{\tau}^n + \Delta t \left(\dot{\boldsymbol{\tau}}^{n+1/2} \right) \quad (3.17)$$

The time derivatives of the stresses, $\dot{\boldsymbol{\sigma}}$ and $\dot{\boldsymbol{\tau}}$, are given by Equations (3.18) and (3.19).

$$\dot{\boldsymbol{\sigma}} = \mathbf{C} \mathbf{d}_\sigma \quad (3.18)$$

$$\dot{\boldsymbol{\tau}} = \mathbf{G} \mathbf{d}_\tau \quad (3.19)$$

With \mathbf{C} the material in-plane stiffness matrix, \mathbf{G} the material transverse shear stiffness matrix and the vectors

$$\begin{aligned} \mathbf{d}_\sigma &= [d_{xx} \quad d_{yy} \quad d_{xy}]^T \\ \mathbf{d}_\tau &= [d_{xz} \quad d_{yz}]^T \end{aligned}$$

Note that the time integration, here done in the step of calculating the stresses, can be done in other steps as well. In the user modules of LS-Dyna, it is chosen to integrate the velocities over the time step, thus creating the displacement increments. Hence, the $\Delta \mathbf{u}$ of Equation (3.5) is used to calculate the strain increments, see Equation (3.20).

$$\Delta \boldsymbol{\varepsilon} = \mathcal{B} \Delta \mathbf{u} \quad (3.20)$$

With \mathcal{B} the strain-displacement matrix, which is a 6x24 matrix containing the spatial derivatives of the shape functions. How this matrix is filled depends on the arrangement of the strain and displacement components in $\Delta \boldsymbol{\varepsilon}$ and $\Delta \mathbf{u}$. In the user modules of LS-Dyna, the six components of $\Delta \boldsymbol{\varepsilon}$ are called $d1$ to $d6$. The eight unique entries of \mathcal{B} are given through the shortened form \mathcal{B}^s in Equation (3.21).

$$\mathcal{B}^s = \frac{1}{2A} \begin{bmatrix} y_2 - y_4 & y_3 - y_1 & y_4 - y_2 & y_1 - y_3 \\ x_4 - x_2 & x_1 - x_3 & x_2 - x_4 & x_3 - x_1 \end{bmatrix} \quad (3.21)$$

With A the area of the element, calculated by Equation (3.22); x_I and y_I the local coordinates of node I and the entries of \mathcal{B}^s following Equation (3.23).

$$A = \frac{1}{2} \left((x_3 - x_1)(y_4 - y_2) + (x_2 - x_4)(y_1 - y_3) \right) \quad (3.22)$$

$$\mathcal{B}_{1I}^s = \frac{\partial N_I}{\partial x}, \quad \mathcal{B}_{2I}^s = \frac{\partial N_I}{\partial y} \quad (3.23)$$

With N_I the shape functions of Equation (3.15).

Finally, in the case of a linear elastic material law, the new stresses are calculated by Equations (3.24) and (3.25). Application of a non-linear material law is also possible, as will be explained in Section 5.2.1.

$$\Delta \boldsymbol{\sigma} = \mathbf{C} \Delta \boldsymbol{\varepsilon} \quad (3.24)$$

$$\boldsymbol{\sigma}^{n+1} = \boldsymbol{\sigma}^n + \Delta \boldsymbol{\sigma} \quad (3.25)$$

With the stresses now available, the force and moment resultants at the integration point are calculated identically as in the FSDT, see Equations (2.19) to (2.21). Afterwards, these resultants are integrated and extrapolated to the nodes to create the nodal forces and moments. This results in Equations (3.26) to (3.31).

$$f_{xI} = A \left(\mathcal{B}_{1I}^s \int_{-h/2}^{h/2} \sigma_{xx} dz + \mathcal{B}_{2I}^s \int_{-h/2}^{h/2} \tau_{xy} dz \right) \quad (3.26)$$

$$f_{yI} = A \left(\mathcal{B}_{2I}^s \int_{-h/2}^{h/2} \sigma_{yy} dz + \mathcal{B}_{1I}^s \int_{-h/2}^{h/2} \tau_{xy} dz \right) \quad (3.27)$$

$$f_{zI} = Ak \left(\mathcal{B}_{1I}^s \int_{-h/2}^{h/2} \tau_{xz} dz + \mathcal{B}_{2I}^s \int_{-h/2}^{h/2} \tau_{yz} dz \right) \quad (3.28)$$

$$m_{xI} = A \left(\mathcal{B}_{2I}^s \int_{-h/2}^{h/2} z \sigma_{yy} dz + \mathcal{B}_{1I}^s \int_{-h/2}^{h/2} z \tau_{xy} dz - \frac{1}{4} k \int_{-h/2}^{h/2} \tau_{yz} dz \right) \quad (3.29)$$

$$m_{yI} = A \left(-\mathcal{B}_{1I}^s \int_{-h/2}^{h/2} z \sigma_{xx} dz + \mathcal{B}_{2I}^s \int_{-h/2}^{h/2} z \tau_{xy} dz + \frac{1}{4} k \int_{-h/2}^{h/2} \tau_{xz} dz \right) \quad (3.30)$$

$$m_{zI} = 0 \quad (3.31)$$

With \mathcal{B}_{2I}^s and \mathcal{B}_{1I}^s the entries of the contracted strain-displacement matrix of Equation (3.21) and A the area of the element of Equation (3.22).

To be able to construct the total internal force vector in the BLT element, Equations (3.26) to (3.31) show that integrations through thickness are needed. This is done in the BLT element by making use of Gaussian quadrature. Considering only elastic behaviour of materials, two integration points would be sufficient to cover all integrations of Equations (3.26) to (3.31). This can be the case for ductile metals, if the structure will stay connected during an impact event. However, for composites the fragmentation seen during crushing calls for an option to gradually let sublaminates of the laminate fail during crushing, creating stress functions which can be non-continuous through thickness. Accurately covering this can be done by increasing the number of integration points through thickness, and deleting an integration point (i.e. setting its stress values to 0) if the sublaminate this point represents has failed. Therefore, the number of integration points through thickness is usually set to 5 [76, 78].

3.3 Initial Considerations for Concept

Figure 3.3 shows a design cycle as used in automotive applications. When using this so-called V-diagram in combination with CFRP materials, up to the phase of “Requirements on Material/Structure” the layup of components is not known. However, already in the phases of “Loadpath Concept” and “FE-Loadpath Model” FEA has proven to be a valuable design tool for metals. To be able to use FEA in this phase for CFRP as well, a new material model is in development which does not rely on exact layups, but on the total stiffness and strength of a plate. Hence, a homogenized material in combination with the ESL method is chosen to represent the laminate. With this approach, requirements on laminates and components could be obtained and laminates can be designed to fulfil global requirements, like stiffness, strength, crushing stress and delamination characteristics. This approach also makes it possible to develop requirements on components and perform tests on components in an early design stage. The goal of the material model in development is that material constants, like failure strengths and stiffnesses, are mainly to be obtained through static and dynamic tests. However, to limit the scope of this thesis, the assumption is made that material properties are to be obtained using CLT or FSDT. Further assumptions are that only symmetric, balanced laminates are used, with negligible bending-twisting coupling. Also, the laminates used will at least have 8% of the fibres in the layup aligned with each of the four principle directions, to prevent failures due to secondary load cases.

3.4 Current Methods of Modelling Delamination in Finite Element Analysis

There are numerous ways to model delamination of laminates in FEA, which can be categorised in the scale they operate; on the micro-, meso- or macro-scale. On the micro-scale,

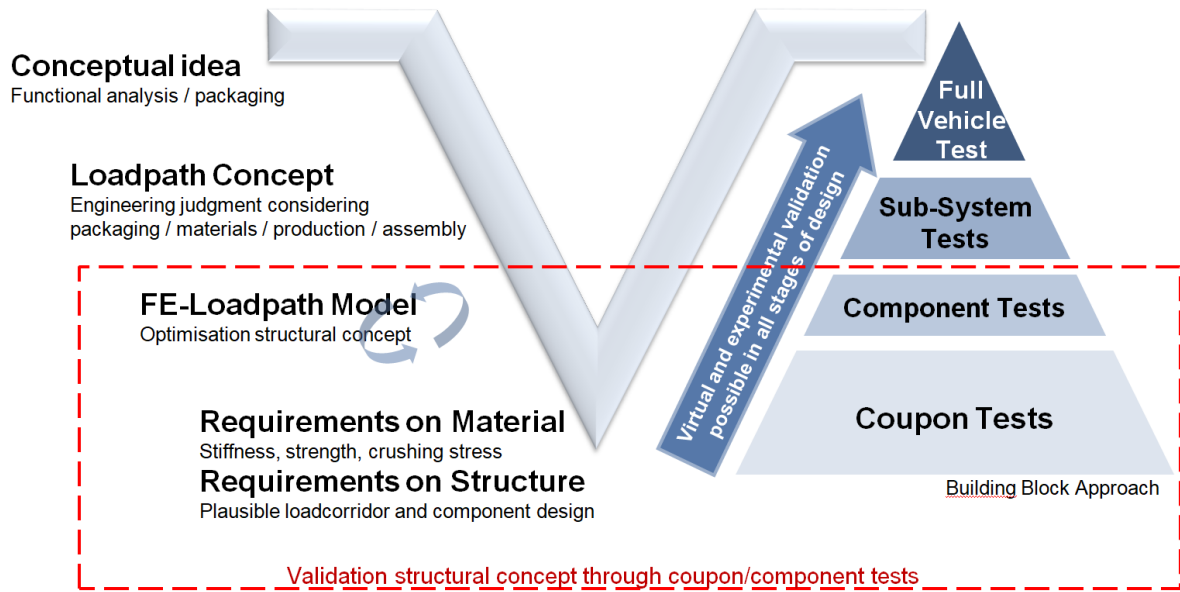


Figure 3.3: Design diagram of a new car from initial idea to validation through full scale NCAP tests [18]

each of the fibres in a yarn is modelled separately. On the meso-scale, the modelling is on ply-level as a multiphase material. On the macro-scale, the laminate is being modelled as unidirectional plies stacked together. The equivalent single layer method falls into the last scale, hence, this section will focus on modelling delamination on macro-scale. The most common approach is to model each ply with one shell or brick element through thickness, which are separated by connecting elements to simulate the bond between two plies. Connecting elements used in this approach are the cohesive zone elements of Alfano and Crisfield [15] and Camanho, et al. [16] and the constraint element of Greve and Prickett [17] fall into this category. The use of these elements requires knowledge of the expected location of delamination in advance, and can only model a number of delaminations equal to the number of connecting elements.

To be used for delamination analysis in composites, cohesive elements need to be inserted at every location where delamination can be expected. Therefore, one can also design a laminate which is prone to delaminate only at a few ply interfaces through thickness, an approach which was used by Reedy et al. [80]. This would decrease the computational cost, as now sublaminates of several plies can be simulated with a single element through thickness.

Another way to model delamination is to make use of the global-local approach: the general global mesh is locally altered to incorporate the delaminated region. For instance, Krueger and O'Brien [13] developed a combined shell/brick modelling technique for which a local three-dimensional solid finite element model is used only in the immediate vicinity of the delamination front. Instead of using solid elements at the delamination front, Gim [14] developed a method in which the delaminated area was modelled by using two layers of plate elements, each representing one of the two sublaminates. While both methods provide reasonably accurate results, their use of changing element types throughout the analysis makes them computationally very expensive in explicit FEA.

3.5 User Modules of LS-Dyna

In the previous sections the theory of FEA and the considerations of the initial concept have been examined. To see what can be implemented in LS-Dyna, this section describes the user modules of this software package and what manipulations can be made for the implementation. The user subroutines used in LS-Dyna are given in Table 3.1 and Figure 3.4. The user modules are written in Fortran, with most of the routines in the file `dyn21b.f`. The user material subroutines are the only exception, they are found in the file `dyn21.f`.

In the user modules, it is possible to create new parameters belonging to elements. An example of this is the damage parameters of Figure 5.2, which are used in the `umatXXv` subroutine. The value of these parameters is allowed to change freely in time steps. It is also possible to create new elements belonging to nodes, however, there is a problem on how these parameters can be processed. The root of this problem is in how LS-Dyna divides the total analysis into subanalyses when using multiple CPUs. All elements of the total analysis are divided into subanalyses, usually of elements linked to each other. The way LS-Dyna submits each subanalysis to its own CPU, makes communication between the subanalyses while they are running impossible in user subroutines [18]. Since each element only belongs to one subanalysis, this allows for easy processing of parameters being stored on elements. However, on the border between two element groups, nodes are part of more than one subanalysis. This means that if these node parameters are processed during different subanalyses, there may be more than one value for a single node parameter. When assembling the subanalyses back together, a maximum, minimum or average value can be obtained for node parameters belonging to neighbouring subanalyses.

Another limiting factor of the division of the analysis into subanalyses, is in the communication between elements. Inside the double integration point loop of Figure 3.4, a node does not know to which elements it belongs. This can be circumvented by storing a matrix on each node which has all the connecting element IDs. While this has been done before, it proved to be a very computationally expensive routine [18].

Table 3.1: Description of subroutines in the user modules of LS-Dyna.

| Subroutine | Function | Input |
|------------|---|--|
| usrshl | Main subroutine, called for in the "process brick, beam and shell elements"-step of Figure 3.1. Initializes all element properties and user specified parameters. | All |
| usrshl_b | General subroutine for partially assembling the strain-displacement matrix \mathcal{B} . | $\xi; \eta; \zeta; N;$ $N_{,\xi}; N_{,\eta}; h;$ $\mathbf{x}; \mathbf{v}; \boldsymbol{\omega}$ |
| ushl_bXXX | Calculates \mathcal{B} for element type XXX, with XXX ranging from 101 to 105. Contains all shape functions and their derivatives. | $\xi; \eta; \zeta; N;$ $N_{,\xi}; N_{,\eta}; h;$ \mathbf{x} |
| usrshl_b2b | Performs matrix operations for final form of \mathcal{B} . | \mathcal{B} |
| usrshl_str | Computes strain and rotation increments in element coordinate system, see Equations (3.5) and (3.20). | $\mathcal{B}; \Delta \mathbf{u}$ |
| usrshl_con | Transfers information from element subroutines to material subroutines. | |
| usrmat | Selects right type of constitutive model used, in this case shell, 's'. | |
| urmats | Transforms strain increments and stresses from element coordinate system to material coordinate system. | $\boldsymbol{\sigma}^{n-1}; \boldsymbol{\tau}^{n-1};$ $\Delta \boldsymbol{\varepsilon}; \Delta \boldsymbol{\gamma}; \boldsymbol{\varepsilon};$ $\boldsymbol{\gamma}$ |
| umatYYv | Material model for material type YY, with YY ranging from 41 to 50. Updates the stresses, including calculation of non-linear material behaviour (Figure 5.2), damage parameters and final failure. | $E; R; \boldsymbol{\sigma}^{n-1};$ $\boldsymbol{\tau}^{n-1}; \Delta \boldsymbol{\varepsilon};$ $\Delta \boldsymbol{\gamma}; \boldsymbol{\varepsilon}; \boldsymbol{\gamma};$ D^n |
| usrshl_frc | Calculates element forces and moments. | Of all int. points: $\mathcal{B};$ $\boldsymbol{\sigma}^n; \boldsymbol{\tau}^n$ |

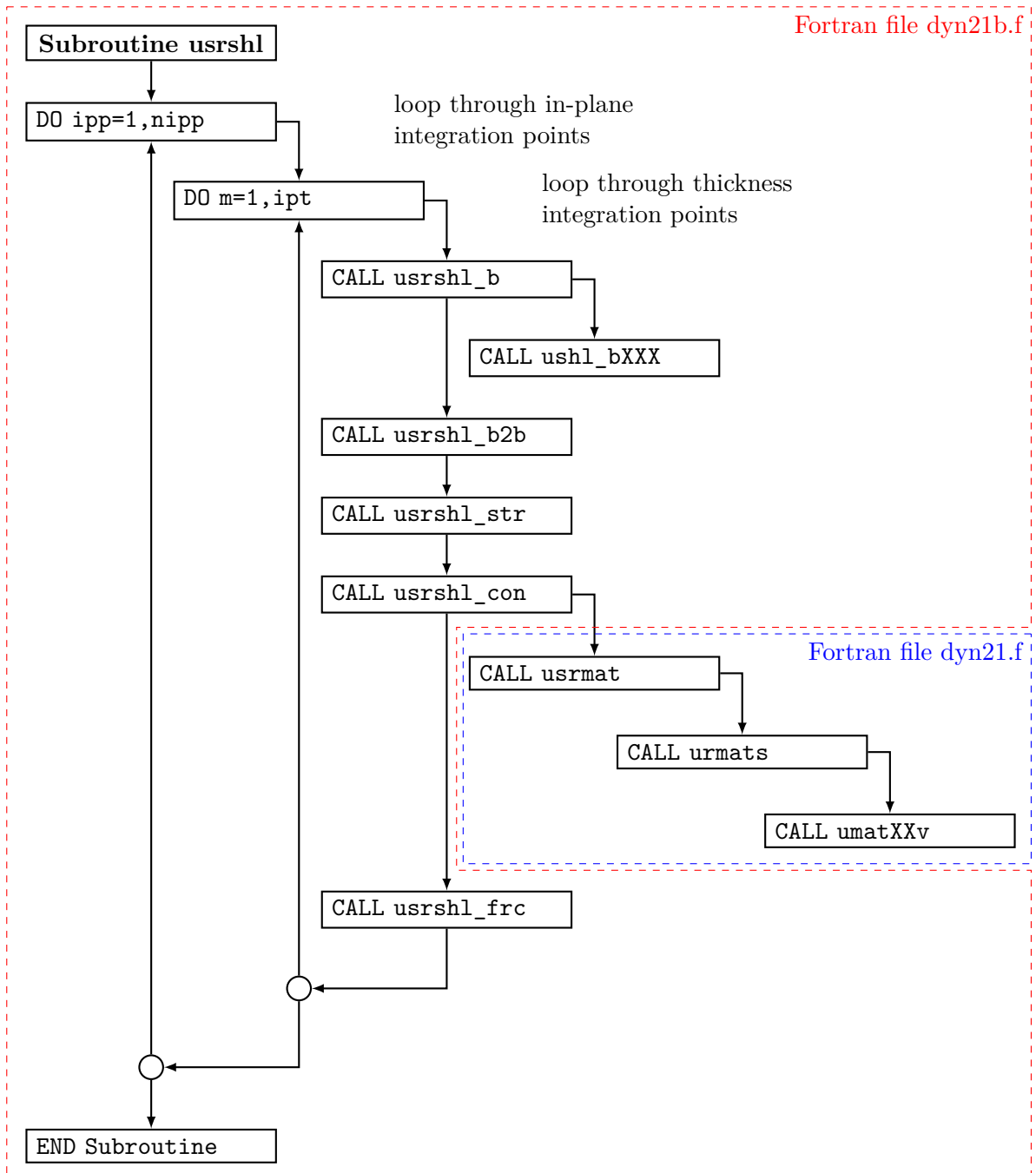


Figure 3.4: Schematic of the routines used for the user shell element modules, see Table 3.1 for routine descriptions.

Prediction of Delamination Initiation

In general, there are three groups of methods for the detection of onset of delamination. The first group uses cohesive zone elements to detect delamination. Section 3.4 showed that this group cannot be used in combination with the ESL method, because it requires more than one element through thickness. The second group assumes pre-existing flaws in the material, which can be seen as cracks. This group of methods then looks at the stresses and strains and checks if there is growth possible of such a small defect.

The second group of methods, which focusses on pre-existing flaws in the material, includes the virtual crack closure technique [81], the virtual crack extension technique [82] and using a path-independent integral (i.e. J-integral) to calculate near-tip strain concentrations [83]. These methods have two problems: they require the location of the initial crack and they distinguish between the opening modes I, II and III, visualised in Figure 4.1. To circumvent the first issue, one can assume small defects like voids everywhere in the laminate. However, distinguishing between the three different modes is not possible for the delamination initiation in an ESL method. Even if this would be possible, there are differences in opinion by several authors on how the modes interact with each other. Reasons for these differences include: the difficulty in obtaining, identifying and characterising pure mode III crack growth in experiments [84]; the debate over whether mode III is considered a separate mode or acts together with mode II [85]; and the absence of any reliable tests for mixed mode I-III and II-III crack growth measurements [86]. Hence, methods used to determine growth of delamination, cannot be used combined with an ESL method to detect delamination onset.

The third group calculates the transverse stresses inside a plate and applies a stress based failure criterion on these to see whether delamination occurs. For this method, accurate prediction of the transverse stresses is needed; Section 4.1 shows the possibilities and limitations of this. Next, Section 4.2 covers the failure criterion which will be used in the model. Section 4.3 closes this chapter with the conclusions and an outlook for further work.

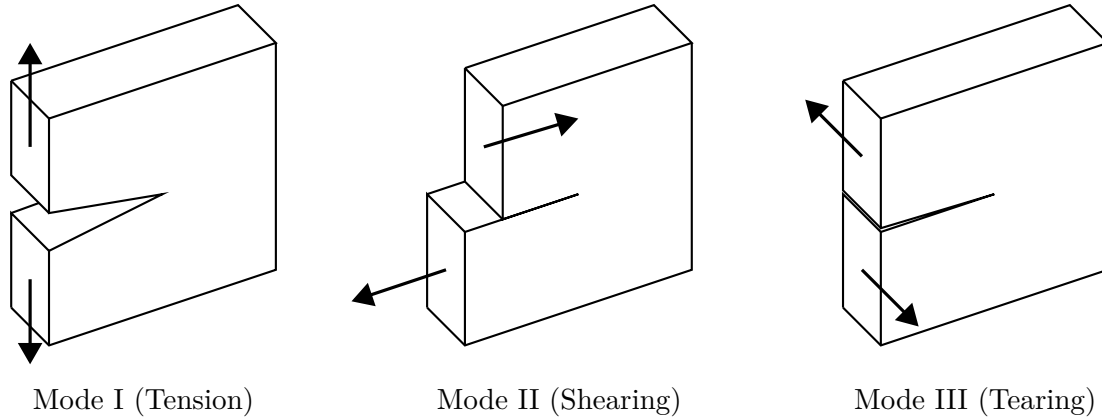


Figure 4.1: Opening modes of cracks

4.1 Prediction of Transverse Stresses

To be able to use a stress-based failure criterion, accurate transverse stresses are needed. As explained in Section 3.2, the BLT element is the basis for this approach. The BLT element in its original form [79] is unable to predict transverse normal stresses, and predicts transverse shear stresses which are constant through thickness. These shear stresses would violate local stress equilibrium on unloaded surfaces. Hence, an alternative to the transverse stresses as predicted by the BLT element is needed.

In this section, first the literature on transverse stresses in FEA is reviewed in Section 4.1.1. The best methods will then be analysed for compatibility with the BLT element in Section 4.1.2. Evaluation of these methods lead to the conclusion that direct implementation of any method to predict transverse normal stresses is not possible. Therefore, attempts to obtain these stresses are described in Section 4.1.3. Afterwards, the effects that homogenizing the material through thickness have on the results for transverse stresses, is explained in Section 4.1.4. Finally, how the improved transverse stresses can be implemented by using the user modules of LS-Dyna is explained in Section 4.1.5.

4.1.1 State of Art Literature on Transverse Stresses in Finite Element Analysis

As alternative to using the transverse stresses predicted by the BLT element, one option is to choose an element based on a different plate theory. Since this will add DOFs to the system, it means that efficiency is sacrificed in the general analysis step for more accuracy on the transverse stresses. To the best knowledge of the author, the element to choose would be the one developed by Tabiei and Tanov [87, 88], since other elements [89–91] would have a higher computational cost. The Tabiei and Tanov element uses a Third-order Shear Deformation Theory (TSDT), a theory which is based on the FSDT, but with added DOFs to improve the accuracy of transverse strains. While an increased accuracy of the shear stress distribution over the BLT element was reported, the eight-fold increase in computing time [88] is considered too high for the use in the current model.

Several other approaches have been considered to obtain more accurate transverse stresses with the use of the BLT element. These approaches, including the the predictor-corrector

approach, the post-processing approach and an approach which uses enrichment formulations, are described in the next paragraphs. Afterwards, these options are compared with each other by making use of comparative studies reported in literature.

Predictor-Corrector Approach

The predictor-corrector approach uses a global solution, obtained by a computationally efficient element like the BLT element (predictor part), followed by a second step which refines certain aspects of the global solution (corrector part). Methods using this approach for computation of the transverse stresses in ESL models [92–98] use in the first step an efficient FSDT element to compute the global response. They differ in the second step; either a refined higher-order shear deformation theory is used [92–94], or a re-analysis using an updated force vector due to the non-linear part of the displacements is performed [95, 99], or the transverse stresses are calculated by means of a re-analysis using improved shear correction factors [96–98]. While most of the methods apply the corrector phase once, some of these methods [93, 99] apply the corrector phase a number of times until the solution is converged.

Post-Processing Approach

The post-processing approach uses the results of each time step to calculate more accurate transverse stresses. This is done by using the three-dimensional equilibrium equations to calculate the transverse stresses, see Equations (4.1) to (4.3).

$$\sigma_{xx,x} + \tau_{xy,y} + \tau_{xz,z} + b_x = 0 \quad (4.1)$$

$$\tau_{xy,x} + \sigma_{yy,y} + \tau_{yz,z} + b_y = 0 \quad (4.2)$$

$$\tau_{xz,x} + \tau_{yz,y} + \sigma_{zz,z} + b_z = 0 \quad (4.3)$$

In which b denotes a body force and a comma represents a derivative with respect to (i.e. $\tau_{xy,y} = \frac{\partial \tau_{xy}}{\partial y}$).

One of the first uses of these equilibrium equations in combination with a shell finite element, is the work of Pryor and Barker [100]. Equations (4.1) and (4.2) were used to recover the transverse shear stresses by deriving the in-plane stresses and then integrating them over the thickness. The element they used had 28 DOFs, compared to the 20 provided by the BLT element. The extra DOFs were needed to set up a third order equation for w in x and y , otherwise the derivatives needed in Equations (4.1) and (4.2) are non-existent. They showed a significant improvement in the transverse shear stresses compared to other finite elements at that date. However, the approach comes at a cost of more DOFs, and hence, is computationally more expensive. Other approaches calculating the transverse shear stresses using higher-order shear deformation theories are, amongst others, developed by Chauduri [101] and Reddy et al. [102].

Instead of using a higher-order theory, Rolfes and Rohwer [103] used additional assumptions to recover the transverse stresses with Equations (4.1) and (4.2). By neglecting the influence of membrane forces and assuming two cylindrical bending modes, the transverse shear stresses are only a function of the transverse shear forces. Using this approach, they were also able

to compute improved shear stiffnesses, no longer needing shear correction factors. Therefore, instead of needing a higher-order shear deformation theory or a higher-order element, the transverse shear stresses can be computed in a 4-node element based on FSDT, like the BLT element.

Further building on this theory, Rolfes et al. [66] used Equation (4.3) to calculate the transverse normal stress inside such an element as well. Since second derivatives of the out-of-plane displacement w are needed, the method could only be applied to parabolic quadrilateral elements using FSDT. Noting small errors in their printed paper (see the corrected Equations (19 of [66]) and (20 of [66])), the solutions agree well with (semi-)analytical solutions. However, a comparison for elements with an initial curvature is missing.

$$\mathbf{c}(z) = \frac{1}{2} \sum_{i=1}^{k-1} \bar{\mathbf{Q}}_i (z_{i+1} - z_i)^2 + \frac{1}{2} \bar{\mathbf{Q}}_k (z - z_k)^2 + \sum_{i=1}^{k-1} \bar{\mathbf{Q}}_i (z_{i+1} - z_i) \cdot (z - z_{i+1}) \quad (19 \text{ of [66]})$$

$$\mathbf{d}(z) = \frac{1}{6} \bar{\mathbf{Q}}_k z^3 + \sum_{i=1}^k \bar{\mathbf{Q}}_i z_i^2 \left(\frac{1}{2} z - \frac{1}{3} z_i \right) + \sum_{i=1}^{k-1} \bar{\mathbf{Q}}_i z_{i+1}^2 \left(\frac{1}{2} z - \frac{1}{3} z_{i+1} \right) \quad (20 \text{ of [66]})$$

Tanov and Tabiei [104] used added an additional assumption to the work of Rolfes et al. to prevent the need for parabolic elements: they assume that the ratio of the transverse shear strains in an element, γ_{xz} and γ_{yz} , is equal to the weighted ratio of the derivatives of the transverse shear forces, $R_{xz,x}$ and $R_{yz,y}$. In this case, weighted means weighted with respect to the transverse shear stiffness in their respective directions. They mentioned themselves that this assumption is quite arbitrary, although the comparison with a 3D elasticity solution showed good agreement. Furthermore, this method is only capable of calculating transverse normal stresses due to locally applied transverse loads, the transverse stresses due to curvatures cannot be predicted.

Alfano et al. [105] used a different way to obtain the higher-order functions needed to construct the transverse normal stress profile. For each node, they constructed an extensional and bending strain field, using strain values of nodes of neighbouring elements. Focussing on transverse normal stresses due to locally applied loadings, their comparison to three-dimensional elasticity solutions showed equal accuracy as previously mentioned methods of Rolfes et al. [66] and Tanov and Tabiei [104]. As like in previous mentioned papers, no studies were made of transverse normal stresses due to curvatures. Furthermore, since the method requires strain values of neighbouring elements, the computational cost of implementing this in the user modules of LS-Dyna is too high.

A method which does take the transverse stresses due to curvatures into account, is presented in the PhD thesis of Roos [106]. Although this method is mainly developed for a self-designed parabolic element, Section 5.2 of the thesis shows a method to calculate the initial curvature for 4-node elements, needed for the evaluation of transverse normal stresses. Just like the method of Alfano et al. [105], it requires communication between elements, on the basis of nodes. Furthermore, a comparison was done between the solution using a mesh constructed of 4-node elements and using doubly-curved 8-node elements. This comparison showed an under prediction of 55.7% in transverse normal stress for the model with 4-node elements, even though its mesh was more refined at critical areas.

Other Methods

Comparable to the predictor-corrector approach, Schuerg et al. [107] used a coupled system of ordinary differential equation in terms of two warping functions to calculate the transverse shear stresses. Although no higher-order theories are needed in this model, solving the system of differential equations described in the paper is still computationally expensive.

Kant and Manjunatha [108] proposed several elements for evaluation of both transverse shear and normal stresses. Since the elements themselves are based on higher-order shear deformation theories, they are not of interest. To obtain the transverse stresses via the equilibrium equations (i.e. Equations (4.1) to (4.3)), they propose the *central difference exact surface fitting method*. This method interpolates the in-plane stresses of 9-noded or 16-noded elements, such that the second and third derivatives of these, needed for the equilibrium equations, are obtained.

The final method discussed in this literature review is based on the eXtended Finite Element Method (XFEM). XFEM, first described by Moes et al. [109], works by enriching a standard, displacement-based FEA near a crack by incorporating two type of fields through a partition of unity method: discontinuous fields and near tip asymptotic fields. Then, it constructs the enriched approximation from the interaction of the crack with the mesh. This technique allows the crack to be represented independently of the mesh, therefore remeshing is not necessary to model crack growth.

For the specific application of modelling delamination, several element formulations and model enrichments in XFEM have been proposed. Nagashima and Suemasu [110] developed a method in which a thin-walled structure containing a bonded joint is modelled by shell elements, and the nodes on the interface are enriched in order to model the delamination. The goal for this method was to model delamination of two bonded surfaces, like a stiffener bonded to a skin. Therefore, only a single delamination can be modelled at the interface, which should be defined during preprocessing.

An enrichment formulation to model delaminations in general is proposed by Brouzoulis et al. [111], which is also capable of modelling the interaction between intraply matrix cracks and delaminations. To prevent constant through thickness transverse shear strain, they use an element with 7 DOFs per node. Building on this approach, Framby et al. [112] developed a method to predict delamination onset and growth. To recover the transverse normal stress, they use a method based on the *central difference exact surface fitting method* as proposed by Kant and Manjunatha [108]. They change this method, by instead of using the in-plane stresses of different integration points in a single element, using these stresses of neighbouring elements. As was explained in Section 3.5, acquiring this type of information while staying inside a subanalysis during an analysis is computationally very expensive. So even though the XFEM approach provides methods to model the effects of delamination, it relies on the same approaches used in general FEA to recover the transverse stresses and predict delamination.

Comparisons

To evaluate the different methods described in the previous paragraphs, several comparative studies are presented in literature. The results of these are presented in Table 4.1, based on the following comparisons. In the studies of Noor et al. [113, 114], their own predictor-corrector

approach [97] was compared to a general FSDT approach (without any additional post-processing) and three more refined plate theories. Noor and Malik [115] compared a further developed predictor-corrector approach [93] to three refined plate theories. Final comparative study included in Table 4.1 is the one of Rohwer et al. [116], in which the approach of Rolfe and Rohwer [103] was compared to the direct application of Equations (4.1) to (4.3) and several more refined plate theories. The remaining theories in Table 4.1 [66,87,88,99,106,112] were ranked based on comparisons made in their own studies.

Table 4.1: Qualitative comparison of methods to calculate transverse shear and normal stresses

| Approach type | Ref. | Accuracy ¹ | | Computational |
|---|---------|-----------------------|---------------------|-------------------------|
| | | Shear | Normal ² | Efficiency ³ |
| FSDT 4-node element (standard BLT element) | [79] | -- | X | ++ |
| FSDT 4-node element with post-processing and improved shear stiffness | [103] | o | X | ++ |
| FSDT 4-node shell element with initial curvature computation | [106] | o | ++ (C:-) | + |
| FSDT 8-node shell with post-processing and improved shear stiffness | [66] | o | ++ | + |
| FSDT 8-node shell element including curvature effects | [106] | o | ++ (C: o) | + |
| FSDT 4-node shell predictor, non-converged corrector approach | [97,99] | o | ++ | - |
| FSDT 4-node shell predictor, converged corrector approach | [93,99] | + | ++ | -- |
| TSDT 4-node element | [87,88] | o | X | - |
| TSDT 4-node element with XFEM, using exact surface fitting method | [112] | o | ++ | - |

¹ Maximum error reported in literature: ++ <2%; + <5%; o <20%; - <50%; -- >50% or incorrect trend; X: non-existent stress.

² Only Roos' [106] methods are capable of predicting normal stresses due to curvature effects (C), which are therefore mentioned separately from normal stresses due to applied loads. All methods which are capable of calculating the transverse normal stress due to applied loads are very accurate, since a general, accurate third-order equation can be constructed for every symmetric laminate.

³ Only qualitative, since no quantitative data is mentioned in literature except for the TSDT element of Tabiei and Tanov [87,88], mentioning an 8-fold increase in computation time over the BLT element.

The following is concluded from the comparison in Table 4.1. All described methods provide a decent improvement in accuracy on transverse shear stress when compared to the standard BLT element formulation. Furthermore, as soon as a method is capable of predicting transverse normal stress, it does it accurately as well (within 2% of a three-dimensional elasticity solution). Lastly, the efficiency for the post-processing methods is still decent, but for elements using predictor-corrector approaches or a more refined plate theory, there is an unacceptable increase in computing cost. For both accuracy and efficiency, ‘o’ is considered the minimum to be used in the new material model [18]. However, currently there are no 8-node elements implemented in the LS-Dyna user modules or the capability to compute initial curvature. Therefore, the solution that will be implemented for computation of transverse shear stresses is the one of Rolfes and Rohwer [103]. There is currently no method to predict transverse normal stresses in 4-node shell elements, which can readily be implemented into the user modules of LS-Dyna. Section 4.1.3 will analyse this problem further.

4.1.2 Prediction of Transverse Stresses in Shell Elements

As explained in the previous section, the method developed by Rolfes and Rohwer [103] is the most promising one to predict the transverse shear stresses. Therefore, this method is explained in more detail in this section, together with additions to this theory, like the one of Tanov and Tabiei [104].

In each element, two cylindrical bending modes are assumed and the influence of the membrane forces on the transverse shear stresses is neglected. This means that the transverse shear stresses will only be a function of the transverse forces, which for most practical cases is a valid assumption [66, 103]. Furthermore, this is also in line with how the FSDT is built up (see also Section 2.2); the membrane behaviour is modelled independently from the transverse forces, by the introduction of two new DOFs with respect to the CPT: the two cross-sectional rotations θ_x and θ_y . Afterwards, these are equilibrated in the nodal force and moments calculations, i.e. Equations (3.26) to (3.31) (or, in the case of explicit FEA, the accelerations are calculated).

Applying the two previously explained assumptions on the equilibrium Equations (4.1) and (4.2), results in in Equation (4.4).

$$\boldsymbol{\tau}(z) = \begin{bmatrix} F_{11} & F_{32} \\ F_{31} & F_{22} \end{bmatrix} \mathbf{R} \quad (4.4)$$

With $\boldsymbol{\tau}$ the transverse shear stresses, F_{ij} components of the stress-force resultant matrix \mathbf{F} given by Equation (4.5) and \mathbf{R} the transverse shear forces given by Equation (4.11).

$$\mathbf{F}(z) = \left(\mathbf{a}(z) \mathbf{A}^{-1} \mathbf{B} - \mathbf{b}(z) \right) \mathbf{D}^{*-1} \quad (4.5)$$

With A and B the membrane and coupling matrix of the composite laminate and \mathbf{D}^* the reduced bending stiffness matrix, see Equation (4.6). Furthermore, the partial membrane stiffness $\mathbf{a}(z)$ and partial coupling stiffness $\mathbf{b}(z)$ are given by Equations (4.7) and (4.8), respectively.

$$\mathbf{D}^* = \left(\mathbf{D} - \mathbf{B}^T \mathbf{A}^{-1} \mathbf{B} \right) \quad (4.6)$$

With \mathbf{D} the bending stiffness matrix of the laminate.

$$\mathbf{a}(z) = \int_{\lambda=-h/2}^{\lambda=z} \mathbf{Q} d\lambda \quad (4.7)$$

$$\mathbf{b}(z) = \int_{\lambda=-h/2}^{\lambda=z} \mathbf{Q} \lambda d\lambda \quad (4.8)$$

With \mathbf{Q} the reduced stiffness of the local lamina, z the thickness coordinate and h the total thickness of the laminate. Note that $\mathbf{a}(h/2) = \mathbf{A}$, the laminate membrane stiffness matrix, and $\mathbf{b}(h/2) = \mathbf{B}$, the laminate coupling matrix. Furthermore, since \mathbf{Q} is a piece-wise constant function through thickness, Equations (4.7) and (4.8) can be written as sums, as shown in Equations (4.9) and (4.10).

$$\mathbf{a}(z) = \mathbf{Q}_k (z - z_k) + \sum_{i=1}^{k-1} \mathbf{Q}_i (z_{i+1} - z_i) \quad (4.9)$$

$$\mathbf{b}(z) = \frac{1}{2} \mathbf{Q}_k (z^2 - z_k^2) + \frac{1}{2} \sum_{i=1}^{k-1} \mathbf{Q}_i (z_{i+1}^2 - z_i^2) \quad (4.10)$$

In which the thickness location z lies in lamina k and an subscripts of z denote the thickness location of the lower surface of that lamina.

$$\mathbf{R} = \underbrace{\int_{z=-h/2}^{z=-h/2} \begin{bmatrix} F_{11} & F_{31} \\ F_{32} & F_{22} \end{bmatrix} \begin{bmatrix} G_{55} & G_{45} \\ G_{45} & G_{44} \end{bmatrix}^{-1} \begin{bmatrix} F_{11} & F_{32} \\ F_{31} & F_{22} \end{bmatrix} dz}_{\mathbf{H}} \gamma \quad (4.11)$$

With \mathbf{G} the matrix of transverse shear moduli, γ the transverse shear strains and \mathbf{H} the improved shear stiffness matrix. The use of this improved shear stiffness matrix eliminates the use of shear correction factors as done in the extension for FSDT for composites, see Equation (2.18). An improvement in accuracy of the transverse shear stresses is the result [103].

Next to the transverse shear stresses, Rolfes et al. [66] also developed a method to predict the transverse normal stresses. Using the same assumptions, the result is given by Equation (4.12).

$$\sigma_{zz}(z) = - \left(\begin{bmatrix} F_{11}^* & F_{32}^* \end{bmatrix} \mathbf{R}_{,x} + \begin{bmatrix} F_{31}^* & F_{22}^* \end{bmatrix} \mathbf{R}_{,y} \right) + p_0 \quad (4.12)$$

With p_0 the applied transverse load at $z = -h/2$, F_{ij}^* components of the resulting matrix given by Equation (4.13) and the derivatives of the shear forces $\mathbf{R}_{,x}$ and $\mathbf{R}_{,y}$ given by Equations (4.16) and (4.17), respectively.

$$\mathbf{F}^*(z) = \left(\mathbf{c}(z)\mathbf{A}^{-1}\mathbf{B} - \mathbf{d}(z) \right) \mathbf{D}^{*-1} \quad (4.13)$$

With $\mathbf{c}(z)$ and $\mathbf{d}(z)$ the integrals of $\mathbf{a}(z)$ and $\mathbf{b}(z)$, respectively, and given by Equations (4.14) and (4.15).

$$\mathbf{c}(z) = \frac{1}{2}\mathbf{Q}_k(z - z_k)^2 + \sum_{i=1}^{k-1} \mathbf{Q}_i(z_{i+1} - z_i) \left(z - \frac{1}{2}z_{i+1} - \frac{1}{2}z_i \right) \quad (4.14)$$

$$\mathbf{d}(z) = \frac{1}{6}\mathbf{Q}_k(z^3 + 2z_k^3 - 3z_k^2z) + \frac{1}{2}\sum_{i=1}^{k-1} \mathbf{Q}_i \left(\left(\frac{1}{3}z_{i+1}^3 - z_i^3 \right) + \left((z_{i+1} + z_i)(z - z_{i+1}) - z_i^2 \right) (z_{i+1} - z_i) \right) \quad (4.15)$$

$$\mathbf{R}_{,x} = \mathbf{H}\boldsymbol{\gamma}_{,x} \quad (4.16)$$

$$\mathbf{R}_{,y} = \mathbf{H}\boldsymbol{\gamma}_{,y} \quad (4.17)$$

The problem of combining Equations (4.16) and (4.17) with the BLT element lies in the fact that the shear strains $\boldsymbol{\gamma}$ are constant throughout the element in x - and y -direction, as can be seen from Equations (2.5) and (2.6). Therefore, elements with at least parabolic shape functions are needed to implement the transverse normal stress recovery of Rolfe et al. [66]. This is further explained in Section 4.1.3.

Tanov and Tabiei [104] made additional assumptions in their model to prevent the need for parabolic shape functions. First, they assumed no transverse shear coupling in the laminate, hence the non-diagonal terms $G_{45} = 0$ in Equations (4.11), (4.16) and (4.17). Next, they consider bending and shear in x -direction not having any gradients in y -direction (and vice versa), hence $\gamma_{xz,y} = \gamma_{yz,x} = 0$. This leads to \mathbf{H} becoming a diagonal matrix and therefore Equations (4.16) and (4.17) are simplified to Equations (4.18) and (4.19).

$$\begin{bmatrix} R_{xz,x} \\ R_{yz,x} \end{bmatrix} = \begin{bmatrix} H_{11} & 0 \\ 0 & H_{22} \end{bmatrix} \begin{bmatrix} \gamma_{xz,x} \\ 0 \end{bmatrix} \quad (4.18)$$

$$\begin{bmatrix} R_{xz,y} \\ R_{yz,y} \end{bmatrix} = \begin{bmatrix} H_{11} & 0 \\ 0 & H_{22} \end{bmatrix} \begin{bmatrix} 0 \\ \gamma_{yz,y} \end{bmatrix} \quad (4.19)$$

Hence,

$$\sigma_{zz}(z) = -F_{11}^* H_{11} \gamma_{xz,x} - F_{22}^* H_{22} \gamma_{yz,y} \quad (4.20)$$

Equation (4.20) still has two unknowns: $\gamma_{xz,x}$ and $\gamma_{yz,y}$. Combining equilibrium on the upper surface of the laminate with the fact that Tanov and Tabiei assume the load p_0 to be applied to the top surface of the laminate (contrary to Rolfe et al., who assume it to be applied on the lower surface), leads to one relation between the two derivatives, as shown by Equation (4.21).

$$\sigma_{zz}(z = h/2) = -F_{11}^{*top} H_{11} \gamma_{xz,x} - F_{22}^{*top} H_{22} \gamma_{yz,y} = p_0 \quad (4.21)$$

In which F_{11}^{*top} and F_{22}^{*top} denote F_{11}^* and F_{22}^* evaluated at $z = h/2$, respectively. This leaves one relation needed to have a solvable system of equations. One more assumption is therefore needed as presented by Tanov and Tabiei, which is made as follows. First, two new parameters α and β are introduced, such that $H_{11}\gamma_{xz,x} = \alpha \cdot p_0/F_{11}^{*top}$ and $H_{22}\gamma_{yz,y} = \beta \cdot p_0/F_{22}^{*top}$. Then, from Equation (4.21), $\alpha + \beta = 1$. This means that α and β represent the contribution of resultant transverse shear stresses τ_{xz} and τ_{yz} to the transverse normal stress. Now, they make use of the decoupling of behaviour in x - and y -directions again, by assuming that $H_{11}\gamma_{xz,x}$ is proportional to the shear strain γ_{xz} and that $H_{22}\gamma_{yz,y}$ is proportional to the shear strain γ_{yz} , as contribution to σ_z in Equation (4.12). Therefore, the following assumption is made on the ratio of α and β :

$$\alpha = \frac{|\gamma_{xz}|}{|\gamma_{xz}|+|\gamma_{yz}|}; \quad \beta = \frac{|\gamma_{yz}|}{|\gamma_{xz}|+|\gamma_{yz}|} \quad \text{for } |\gamma_{xz}| + |\gamma_{yz}| \neq 0$$

$$\alpha = \beta = \frac{1}{2} \quad \text{for } |\gamma_{xz}| + |\gamma_{yz}| = 0$$
(4.22)

Combining Equation (4.20) with the relations given in Equations (4.21) and (4.22) results in the final expression for σ_z :

$$\sigma_z(z) = -p_0 \left(\alpha \frac{F_{11}^*(z)}{F_{11}^{*top}} + \beta \frac{F_{22}^*(z)}{F_{22}^{*top}} \right)$$
(4.23)

As can be concluded from Equation (4.23), this approach only yield transverse normal stresses on laminates at which a transverse normal load p_0 is applied on the top surface. A general solution for transverse normal stresses at locations without an applied transverse normal load cannot be obtained by the method of Tanov and Tabiei. Furthermore, the equation requires the knowledge whether the applied pressure p_0 acts on top or bottom surface, which is unavailable information when using the BLT element in LS-Dyna.

4.1.3 Attempts on Obtaining Transverse Normal Stress

Trying to find a general solution which can predict transverse normal stresses anywhere in a shell structure, Rolfes et al. [66] stated that at least parabolic shape functions are needed to recover the transverse normal stresses from an analysis based on FSDT elements, in absence of applied transverse normal stresses. The reasoning behind this is as follows. The transverse normal stresses are obtained by substituting the result of Equations (4.16) and (4.17) into Equation (4.12). To do this, first the in-plane derivatives of γ_{xz} and γ_{yz} are needed, which are obtained by using the derivatives of Equations (2.5) and (2.6), given by Equations (4.24) to (4.27).

$$\gamma_{xz,x} = u_{z,xx} + \theta_{y,x}$$
(4.24)

$$\gamma_{xz,y} = u_{z,xy} + \theta_{y,y}$$
(4.25)

$$\gamma_{yz,x} = u_{z,xy} - \theta_{x,x}$$
(4.26)

$$\gamma_{yz,y} = u_{z,yy} - \theta_{x,y}$$
(4.27)

As can be seen from Equations (4.24) to (4.27), the second in-plane derivatives of u_z are needed, which calls for at least parabolic shape functions of u_z . This is the only DOF for which linear shape functions are not sufficient, since only first derivatives are needed of the cross-sectional rotations θ_x and θ_y .

To find a solution for σ_z (Equation (4.12)), attempts were made to acquire a parabolic equation of u_z in the form of Equation (4.28).

$$u_z(\xi, \eta) = C_0 + C_1\xi + C_2\eta + C_3\xi\eta + C_{4a}\xi^2 + C_{4b}\eta^2 \quad (4.28)$$

With the unknown constants C_0 to C_5 to be solved for using boundary conditions, which means a total of 6 are needed. One could also choose for an equation in x and y and then transform back using transformation matrices. However, chosen is for an equation in the isoparametric coordinates ξ and η , because the implementation will have to be done in the stage of the subroutines where these coordinates are used.

The relevant information available in an element is:

- Values of all 20 DOFs of the element: three translational velocities and two angular velocities per node
- Spatial coordinates of all nodes
- Material constants of the element (Young's moduli, poisson ratios, strengths, etc.)
- In-plane damage parameters
- Thickness of the element
- Parameters derived from the previous mentioned ones: displacements, cross-sectional rotations, strain increments and stress increments
- Stresses, strains and internal forces and moments of the previous time step

As was concluded in Section 3.5, relevant information from neighbouring elements during the evaluation of an element can only be obtained at an unacceptable computational cost.

Since the nodal values are solved for in the analysis step, the first four conditions can be obtained from the value of u_z at the nodes. Substituting these to rewrite Equation (4.28) leads to Equation (4.29).

$$u_z(\xi, \eta) = C_5(1 - \xi^2) + C_6(1 - \eta^2) + \sum_{I=1}^4 N_I(\xi, \eta) u_{zI} \quad (4.29)$$

With N_I the linear shape functions as used in the BLT element, see Equation (3.15); u_{zI} the out-of-plane displacement at node I and the new constants C_5 and C_6 to be determined. Rewriting to this form automatically satisfies the solution at the four nodes ($\xi = \pm 1, \eta = \pm 1$).

Several conditions have been invoked to find the two equations for C_5 and C_6 , with no satisfying result. The most promising one was by making use of two additional conditions. Equate the internal energy of the linear solution of u_z to the internal energy of the parabolic solution of u_z , which is the first equation. Second equation is to minimize the internal energy with respect to one of the unknowns C_5 and C_6 . Problem here is that the energy is first set to

a constant value by equating it to the energy of the linear solution, which leaves no possibility for minimization any more.

Next to solving the problems in two dimensions right away, attempts have been made to find the solution for a one-dimensional problem in the form of Equation (4.30), followed by using a form of superposition to construct a two-dimensional solution. One attempt was made by assuming a Timoshenko beam, using the out-of-plane displacement and the cross-sectional rotation to construct a solution for u_z . While the Timoshenko beam theory does allow for a parabolic function of u_z , constructing that solution with the out-of-plane displacement and cross-sectional rotation at the nodes needs the assumption of a constant shear angle. The result is that while the terms of the right-hand sides of Equations (4.24) to (4.27) may be non-zero, the left-hand sides are always zero.

$$u_z(\xi) = C_8 + C_9\xi + C_{10}\xi^2 \quad (4.30)$$

Final attempt to find a parabolic solution for the one-dimensional problem, was to use an idea that had also been used in the two-dimensional case: use u_z at the nodes to get a solution for the first two constants, and equate the internal energy of the linear solution of u_z to the internal energy of the parabolic solution of u_z to get the last unknown. Equivalent to the two-dimensional case, Equation (4.30) can be rewritten to Equation (4.31).

$$u_z(\xi) = C_{11} \left(1 - \xi^2\right) + \frac{\xi - 1}{2} u_{z1} + \frac{-\xi + 1}{2} u_{z2} \quad (4.31)$$

Using the internal energy approach, the trivial solution ($C_{11} = 0$) and a new solution were found. While this new solution was mathematically correct, it was found to be physically invalid. The reason for this, is that the transverse shear strain given by Equation (2.5), is squared in the internal energy equation. If the trivial solution would lead to Equation (2.5) being a positive function, the found second solution would be the negative counterpart of that function. For a more elaborate explanation, see Appendix A.

It should be noted that, once there is a parabolic version of u_z is available, it can readily be implemented into the LS-Dyna code to obtain the transverse normal stress. For this implementation, see Appendix B.

4.1.4 Application to Homogenised Material Model

As was discussed in Section 2.2.2, the overall approach is the usage of a homogenised material model, to gather basic laminate parameters for a new architectural approach. This also effects the transverse stresses, which will be discussed in this section. First, the effects on the transverse shear stress distribution are discussed, followed by the transverse shear stiffness. Then, a comparison is made on the transverse shear stress distribution for six quasi-isotropic laminates.

Transverse Shear Stress Distribution

To explain what the effect of homogenizing the material through thickness has on the distribution of transverse shear stresses, several equations are needed which are given in the

previous sections and chapters. For convenience of the reader, they are revisited below.

The equations for the laminate stiffness and coupling matrices:

$$\mathbf{A} = \int_{-h/2}^{h/2} \bar{\mathbf{Q}} dz \quad (2.13 \text{ revisited})$$

$$\mathbf{B} = \int_{-h/2}^{h/2} \bar{\mathbf{Q}} z dz \quad (2.14 \text{ revisited})$$

$$\mathbf{D} = \int_{-h/2}^{h/2} \bar{\mathbf{Q}} z^2 dz \quad (2.15 \text{ revisited})$$

$$\mathbf{H} = \int_{-h/2}^{h/2} \bar{\mathbf{G}} dz \quad (2.16 \text{ revisited})$$

The equation for the transverse shear stresses as function of the transverse shear force resultant, as derived by Rolfes and Rohwer [103]:

$$\boldsymbol{\tau}(z) = \begin{bmatrix} F_{11} & F_{32} \\ F_{31} & F_{22} \end{bmatrix} \mathbf{R} \quad (4.4 \text{ revisited})$$

The stress-force resultant matrix:

$$\mathbf{F}(z) = \left(\mathbf{a}(z) \mathbf{A}^{-1} \mathbf{B} - \mathbf{b}(z) \right) \mathbf{D}^{*-1} \quad (4.5 \text{ revisited})$$

The reduced bending stiffness:

$$\mathbf{D}^* = \left(\mathbf{D} - \mathbf{B}^T \mathbf{A}^{-1} \mathbf{B} \right) \quad (4.6 \text{ revisited})$$

The partial membrane and coupling stiffness matrices:

$$\mathbf{a}(z) = \mathbf{Q}_k (z - z_k) + \sum_{i=1}^{k-1} \mathbf{Q}_i (z_{i+1} - z_i) \quad (4.9 \text{ revisited})$$

$$\mathbf{b}(z) = \frac{1}{2} \mathbf{Q}_k (z^2 - z_k^2) + \frac{1}{2} \sum_{i=1}^{k-1} \mathbf{Q}_i (z_{i+1}^2 - z_i^2) \quad (4.10 \text{ revisited})$$

The equation for the transverse shear force resultant as function of the transverse shear strains, as derived by Rolfes and Rohwer [103]:

$$\mathbf{R} = \underbrace{\int_{z=-h/2}^{z=h/2} \begin{bmatrix} F_{11} & F_{31} \\ F_{32} & F_{22} \end{bmatrix} \begin{bmatrix} G_{55} & G_{45} \\ G_{45} & G_{44} \end{bmatrix}^{-1} \begin{bmatrix} F_{11} & F_{32} \\ F_{31} & F_{22} \end{bmatrix} dz}_{\mathbf{H}}^{-1} \boldsymbol{\gamma} \quad (4.11 \text{ revisited})$$

Since there is only one layer of material, $\bar{\mathbf{Q}}$ and $\bar{\mathbf{G}}$ are constant through thickness in Equations (2.13) to (2.16). This results in $\mathbf{B} = \mathbf{0}$ and \mathbf{D} given by Equation (4.32).

$$\mathbf{D} = \int_{-h/2}^{h/2} \mathbf{Q} z^2 dz = \frac{h^3}{12} \mathbf{Q} \quad (4.32)$$

This in turn leads to $\mathbf{D}^* = \mathbf{D}$ by the use of Equation (4.6). It also means that $k = 1$ in Equations (4.9) and (4.10), hence the summation in them is dropped. Substituting the results in Equation (4.5) simplifies it to Equation (4.33).

$$\mathbf{F}(z) = -\frac{1}{2} \mathbf{Q} (z^2 - z_k^2) \mathbf{D}^{-1} \quad (4.33)$$

Substituting \mathbf{D} from Equation (4.32) in Equation (4.33) and simplifying gives Equation (4.34).

$$\mathbf{F}(z) = \left(\frac{3}{2h} - \frac{6z^2}{h^3} \right) \mathbf{I}_3 \quad (4.34)$$

Finally, substituting the needed entries of $\mathbf{F}(z)$ from Equation (4.34) into Equation (4.4) gives Equation (4.35).

$$\boldsymbol{\tau}(z) = \left(\frac{3}{2h} - \frac{6z^2}{h^3} \right) \mathbf{R} \quad (4.35)$$

Hence, an expression for more accurate transverse shear stresses inside the BLT element is obtained assuming a homogenised material. It only relies on the transverse shear force of the element, and is a quadratic equation through thickness ranging from zero stress at the top and bottom surface of the element to the maximum at the mid-plane of the element.

Transverse Shear Stiffness

Now that an expression for the stress-force resultant matrix $\mathbf{F}(z)$ is obtained in Equation (4.34), it can be used to improve upon the transverse shear stiffness of an element. This is done by substituting it into Equation (4.11), resulting in Equation (4.36).

$$\mathbf{R} = \frac{5h}{6} \underbrace{\begin{bmatrix} G_{55} & G_{45} \\ G_{45} & G_{44} \end{bmatrix}}_{\mathbf{H}} \boldsymbol{\gamma} \quad (4.36)$$

The resulting equation can now be compared to its counterparts of the general FSDT, i.e. Equations (2.16) and (2.18). The result is the same, if $k = 5/6$ is assumed, which is the case for isotropic plates according to Reissner [28]. Hence, applying the theory of Rolfes and Rohwer [103] to the homogenized material, leads to an unchanged transverse shear stiffness.

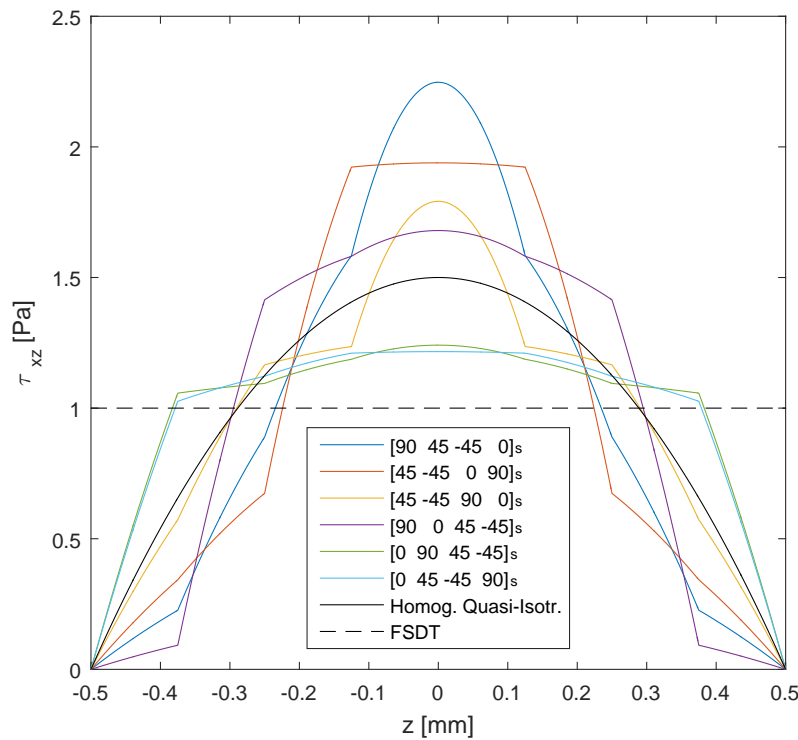


Figure 4.2: Transverse shear stress distribution for different quasi-isotropic layups under an applied shear force

Transverse Shear Stress Comparison

The transverse shear stresses are changed from a constant value to a depending quadratically on the thickness coordinate. To give a brief overview of the effect, this shear stress distribution is compared to the shear stress distribution of the same six quasi-isotropic laminates of Section 2.2.2. These laminates have a unit width and all contain eight plies of 0.125 mm thickness each. On these laminates, a force of $R_x = 1$ N is applied, and the theory of Rolfe and Rohwer [103] is used (see Section 4.1.2) to obtain the shear stress distribution over the thickness. These distributions are compared to the FSDT as used in the BLT element, as well as the parabolic distribution of Equation (4.35). The result is Figure 4.2.

Since all layups are symmetrical, all show their maximum shear stress on the mid-plane of the laminate. The maxima range from 1.22 Pa for the $[0/45/-45/90]_s$ laminate, to 2.25 Pa for the $[90/45/-45/0]_s$ laminate. The FSDT approach as used in the BLT element shows a constant stress of 1 Pa, while the parabolic distribution of Equation (4.35) shows a maximum of 1.5 Pa.

In general, laminates which are designed against bending in the direction of loading (in this case, having the 0-layers on the outside to prevent bending in x-direction, due to the applied load R_x), have lower transverse shear stresses as well for a given applied shear force. The reason for this is that the transverse shear stresses and membrane stresses due to moments are coupled to each other through the stress equilibrium Equations (4.1) and (4.2). Hence, plies

which take up more of the bending load have in turn higher transverse shear stress gradients. This can be seen as the shear stresses being coupled to the membrane stiffness of a ply in Equation (4.10). A ply with a higher in-plane stiffness will result in a higher transverse shear stress gradient, as can also be observed from Figure 4.2. Therefore, having those stiffer plies on the outside of the laminate, will result in a higher gradient at the outside, in turn resulting in a lower maximum shear stress.

4.1.5 Implementation in LS-Dyna

For the calculation of the transverse shear stresses, the thickness coordinate is needed. The last subroutine in the flow chart of Figure 3.4 in which this coordinate is available, is `ushl_bXXX`. This is however the isoparametric thickness coordinate, which is defined as $\zeta = 2 \cdot z/h$. To include this adaptation, elements of \mathcal{B} determining the transverse shear strains need to be multiplied by a factor c_γ , as defined by Equation (4.37).

$$c_\gamma(\zeta) = \frac{3(1 - \zeta^2)}{2h} \quad (4.37)$$

4.2 Delamination Failure Criteria and Adaptation for Shell Elements

Based on a more accurate transverse stress prediction, this section searches for a failure criterion for delamination. To find the best suited delamination failure criterion, Section 4.2.1 starts with a review of the available literature on this topic. One promising failure theory, the one of Puck [117], is analysed in Section 4.2.2 and adjusted to predict pure delamination failure. Together with the most used delamination failure criterion [56], the resulting delamination failure criterion is further simplified in Section 4.2.3, by adding the assumption of no transverse normal stresses. Section 4.2.4 finalises the delamination failure criteria analysis with the implementation in the user modules of LS-Dyna.

4.2.1 State of Art Literature on Delamination Failure Criteria

To evaluate the different theories on delamination onset based on stress analysis, first the World Wide Failure Exercises are examined. One of the the best performing failure criteria in these exercises, the one of Puck, is analysed next, followed by failure criteria designed for pure delamination.

Failure in composites is still hard to predict today, with countless failure criteria often lacking validation across the whole range of load cases they are supposed to cover. This reason led Hinton, Kaddour and Soden to organize the first World-Wide Failure Exercise (WWFE-I) [118]. In this experiment, authors of leading failure criteria and theories were invited to blindly predict failure of various test cases, after which the tests were independently executed and the results were compared. Since this was the first effort to compare failure criteria on such a large scale, only test cases with in-plane failures were addressed. Interesting is that

one of the best performing failure theories was a three-dimensional failure theory, developed by Puck [117].

Because of the critical acclaim the organisers got on WWFE-I, they decided to continue with efforts to determine which failure criteria are best suited for certain load cases. They set up experiments for composites under triaxial loads in the second World-Wide Failure Exercise (WWFE-II) [33, 119–121], focussing on in-ply failures. Hence, no tests were done on prediction of delamination. Out of 12 theories, the theory developed by Puck was among the three best-performing ones, together with the failure criteria developed by NASA's Langley Research Center (LaRC) [122] and the theory developed by Laurin et al. [123]. All three theories have in common that they distinguish between fibre failure and matrix failure, an idea dating back to Hashin's failure criteria [124]. Out of the three best-performing failure theories, Puck's theory is the only one capable of predicting delamination. The opinion of LaRC is that delamination should be included in FEA by the use of cohesion elements [122] as developed by Camanho et al. [16] or Turon et al. [125]. Laurin et al. initially developed their model for first ply failure and final failure, not incorporating delamination. Even though this theory was further developed to take some effects of delamination into account [126], the authors state that delamination is a specific mechanism that must be modelled and identified with specialised tools. Parallel with the second one, also the third World-Wide Failure Exercise (WWFE-III) was started with experiments for cracks and damage development [127, 128]. Among the participants in this exercise are Laurin et al. [129] and the LaRC group [130]. The blind predictions have been published for this exercise [131], the comparison to test results is not finished yet. Nonetheless, the results would only be relevant for the prediction of growth of delamination, not the onset of it.

Puck's failure criteria

The failure theory of Puck [117] (conveniently translated to English and summarized in textbook form by Knops [132]) is a three-dimensional failure criterion, capable of predicting a failure delamination. It distinguishes between damage due to fibre failure and damage due to matrix failure. When comparing to the failure modes in Section 2.3, this means that the modes matrix fracture, interfacial debonding and delamination are all contained in the matrix failure group. Since delamination failure is a matrix failure, only this mode will be evaluated here. Matrix failure in the Puck failure theory is based on the stresses acting on a fracture plane in a single ply, which is always parallel to the fibres. The fracture plane angle α is measured counter-clockwise from the x_3 -axis, hence $\alpha = 90$ deg is pure delamination. For a visualization, see Figure 4.3. Puck's failure criterion for matrix failure distinguished between a tensile and a compressive stress normal to the action plane and is given by Equation (4.38).

$$\begin{aligned} \left(\frac{\tau_{n\psi}}{R_{\perp\psi}}\right)^2 + 2\frac{p_{\perp\psi}^c \sigma_n}{R_{\perp\psi}} &= 1 & \text{if } \sigma_n < 0 \\ \left(\frac{\tau_{n\psi}}{R_{\perp\psi}}\right)^2 + 2\frac{p_{\perp\psi}^t \sigma_n}{R_{\perp\psi}^t} + \left(1 - 2\frac{p_{\perp\psi}^t R_{\perp\psi}^t}{R_{\perp\psi}^t}\right) \left(\frac{\sigma_n}{R_{\perp\psi}^t}\right)^2 &= 1 & \text{if } \sigma_n \geq 0 \end{aligned} \quad (4.38)$$

With R the strength for different failure modes and p the inclinations parameters, which are all material parameters. Superscripts t and c represent tension and compression, respectively. Furthermore, a single n subscript means normal to the action plane, subscript $n\psi$ denotes

Table 4.2: Puck's inclination parameters for typical FRP [133]

| | $p_{\perp\parallel}^t$ | $p_{\perp\parallel}^c$ | $p_{\perp\perp}^t$ | $p_{\perp\perp}^c$ |
|------------|------------------------|------------------------|--------------------|--------------------|
| GFRP/Epoxy | 0.30 | 0.25 | 0.20 to 0.25 | 0.20 to 0.25 |
| CFRP/Epoxy | 0.35 | 0.30 | 0.25 to 0.30 | 0.25 to 0.30 |

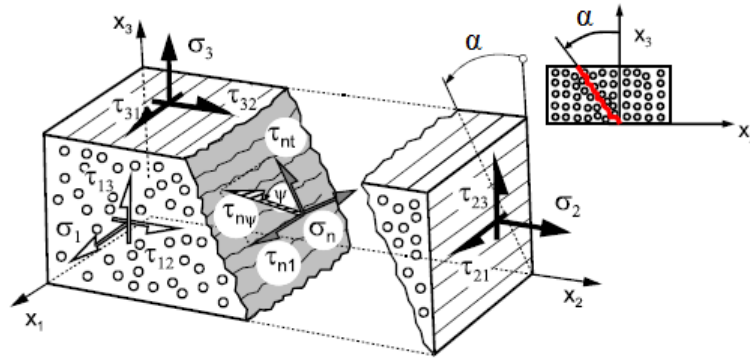
in the plane perpendicular to the action plane, aligned with ψ . The angle ψ itself is defined as the angle between τ_{nt} and $\tau_{n\psi}$, see also Figure 4.3. Subscripts \perp and \parallel are referring to a direction perpendicular and parallel to the fibre direction, respectively.

The strengths R in Equation (4.38) are material parameters and can all be relatively easily obtained by performing tests. The inclination parameters p would require more extensive testing, as these parameters are derivatives of a failure curve. Therefore, several tests are needed with different stress ratios to obtain each p . Recent research [133] suggests that these parameters are a function of type of material (i.e. Glass Fibre Reinforced Polymer (GFRP) or CFRP), rather than the exact specifications of the material (i.e. an AS4 carbon fibre or an IM7 carbon fibre). For epoxy based CFRP and GFRP, these parameters are given in Table 4.2. Strengths and inclination parameters which are a function of ψ will need to be determined by Equations (4.39) and (4.40). The relations between the action plane stresses and stresses in the ply coordinate system are all geometrical and given by Equations (4.41) to (4.44).

$$R_{\perp\psi} = \frac{\tau_{n\psi}}{\sqrt{\left(\frac{\tau_{nt}}{R_{\perp\perp}}\right)^2 + \left(\frac{\tau_{n\parallel}}{R_{\perp\parallel}}\right)^2}} \quad (4.39)$$

$$p_{\perp\psi}^{t,c} = \frac{R_{\perp\psi}}{\tau_{nt}^2 + \tau_{n\parallel}^2} \left(\frac{p_{\perp\perp}^{t,c} \tau_{nt}^2}{R_{\perp\perp}} + \frac{p_{\perp\parallel}^{t,c} \tau_{n\parallel}^2}{R_{\perp\parallel}} \right) \quad (4.40)$$

The strengths $R_{\perp\parallel}$ and R_{\perp}^t can be determined by in-plane shear tests and in-plane tensile tests perpendicular to the fibres, respectively. Experimental results using tests designed purely for $R_{\perp\perp}$ are unreliable, since a transverse shear loading has to be applied, hence

**Figure 4.3:** Definition of coordinate system and angles used in Puck's failure theory [132]

very thick specimens would be needed [117]. However, based on behaviour observed during tests [134–136], Puck is convinced that the transverse shear-off failure observed in in-plane compression can be used to determine this value. Equation (4.45) is used for this.

$$\sigma_n(\alpha) = \sigma_2 \cos^2 \alpha + \sigma_3 \sin^2 \alpha + 2\tau_{23} \sin \alpha \cos \alpha \quad (4.41)$$

$$\tau_{nt}(\alpha) = -\sigma_2 \sin \alpha \cos \alpha + \sigma_3 \sin \alpha \cos \alpha + \tau_{23} (\cos^2 \alpha - \sin^2 \alpha) \quad (4.42)$$

$$\tau_{n1}(\alpha) = \tau_{31} \sin \alpha + \tau_{21} \cos \alpha \quad (4.43)$$

$$\tau_{n\psi}(\alpha) = \sqrt{\tau_{nt}^2 + \tau_{n1}^2} \quad (4.44)$$

$$R_{\perp\perp} = \frac{R_{\perp}^c}{2(1 + p_{\perp\perp}^c)} \quad (4.45)$$

In which subscript t denotes tangential to the fibre direction. Note that n and t refer to the action plane, while \perp and \parallel refer to the fibre direction.

Delamination failure criteria

Next to the three-dimensional failure criteria presented in the previous paragraphs, there are failure criteria solely focussed on the prediction of delamination. Brewer and Lagace [56] developed a failure criterion, Equation (4.46), and compared it to test results of three laminate families: $[\pm 15_n]_s$, $[\pm 15_n/0_n]_s$ and $[0_n/\pm 15_n]_s$, with n ranging from 1 to 5. When comparing their failure criterion to a strain energy release rate approach, they concluded that the strain energy release rate is dependent on effective ply thickness. The results was that the stress based failure criterion showed better correlation to test results.

$$\left(\frac{\tau_{31}}{R_{31}}\right)^2 + \left(\frac{\tau_{23}}{R_{23}}\right)^2 + \left(\frac{\sigma_{33}^c}{R_{33}^c}\right)^2 + \left(\frac{\sigma_{33}^t}{R_{33}^t}\right)^2 = 1 \quad (4.46)$$

Note that only one of the last two terms on the left-hand side can be non-zero. Other, comparable failure criteria purely designed for delamination are the ones of Ochoa and Engblom [137], Equation (4.47); Hashin [124], Equation (4.48); and Lee [138], Equation (4.49).

$$\frac{\tau_{31}^2 + \tau_{23}^2}{R_{23}} + \left(\frac{\sigma_{33}}{R_{33}^t}\right)^2 = 1 \quad (4.47)$$

$$\left(\frac{\tau_{31}}{R_{31}}\right)^2 + \left(\frac{\tau_{23}}{R_{23}}\right)^2 + \left(\frac{\sigma_{33}}{R_{33}^t}\right)^2 = 1 \quad (4.48)$$

$$\frac{\sqrt{\tau_{31}^2 + \tau_{23}^2}}{R_S} = 1 \quad \text{or} \quad \frac{\sigma_{33}}{R_{33}^t} = 1 \quad (4.49)$$

Lee is not clear whether R_S is equal to R_{31} , R_{23} or a combination of the two, just that it should be experimentally obtained [138].

The just mentioned four criteria are all quadratic criteria. The differences can be divided into three categories. First, they debate whether a matrix tension should be separated from matrix compression. Looking at the argumentation given by Hou et al. [139] and by Puck in the previous paragraph, it is expected that there is a difference, since the stresses acting on the failure plane are different; the compressive applied stress results in a shear stress on the failure plane, while the tensile applied stress results in a tensile stress normal to the failure plane. Second, the criteria differ on whether R_{31} has a different value from R_{23} . Since one of these shear stresses is acting along the fibres, and the second one is acting only transverse to the fibres, it is expected that there is a difference. Creemers [140] confirmed this, noting that R_{31} is generally larger than R_{23} . This can furthermore be seen from these strengths of IM7/8551-7 CFRP as obtained by experiments, see Table 2.2. Final difference is whether shear and normal stress interact with each other, or that they can be viewed separately. Since the matrix itself can be viewed as an isotropic constituent in the composite, it is expected that normal stress and shear stresses acting on the matrix do interact with each other. This is backed up by looking at the in-plane matrix failure criteria of LaRC [122] and Laurin et al. [123], next to Puck the other two best-performing theories of WWFE-II, both having interaction in their matrix failure criteria. Hence, it is expected that this is also the case for delamination, making the criterion of Brewer and Lagace the best candidate out of the four pure delamination failure criteria.

Further building on the effect of interaction of stresses on delamination strength, Fenske and Vizzini [141] developed a criterion also taking into account the in-plane stresses acting on a laminate. Comparing their criterion to the one of Brewer and Lagace on test results of the same three laminate families ($[\pm 15_n]_s$, $[\pm 15_n/0_n]_s$ and $[0_n/\pm 15_n]_s$, with n ranging from 1 to 5), they obtained an increase in average accuracy of 0.8% over the 15 tests. However, this increase in accuracy is not deemed justified by the increase in complexity, and hence computational effort.

4.2.2 Puck's Failure Criteria for Pure Delamination

Due to the homogenized material approach, the distribution of fibre directions through thickness is not known. This is of importance for the failure theory of Puck, since its matrix failure mode relies on fracture planes parallel to the fibre direction. However, there is one plane always parallel to the fibres; the 12-plane of Figure 4.3. Combining this with the fact that the goal is to look for delamination, which is a fracture on the 12-plane, an angle of $\alpha = 90$ deg will be used. This leads to Equations (4.41) to (4.44) being reduced to Equations (4.50) to (4.53).

$$\sigma_n(\alpha = 90 \text{ deg}) = \sigma_{33} \quad (4.50)$$

$$\tau_{nt}(\alpha = 90 \text{ deg}) = \tau_{23} \quad (4.51)$$

$$\tau_{n1}(\alpha = 90 \text{ deg}) = \tau_{31} \quad (4.52)$$

$$\tau_{n\psi}(\alpha = 90 \text{ deg}) = \sqrt{\tau_{23}^2 + \tau_{31}^2} \quad (4.53)$$

Substituting Equations (4.50) to (4.53) into the relation for the strength $R_{\perp\psi}$ (Equation (4.39)) leads to Equation (4.54).

$$R_{\perp\psi} = \frac{R_{\perp\perp} R_{\perp\parallel} \sqrt{\tau_{23}^2 + \tau_{31}^2}}{\sqrt{\tau_{23}^2 R_{\perp\parallel}^2 + \tau_{31}^2 R_{\perp\perp}^2}} \quad (4.54)$$

Noting that all R s are always defined positive [117]. Now, substituting into the relation for $p_{\perp\psi}^{t,c}$ (Equation (4.40)) leads to Equation (4.55).

$$p_{\perp\psi}^{t,c} = \frac{p_{\perp\perp}^{t,c} \tau_{23}^2 R_{\perp\parallel} + p_{\perp\parallel}^{t,c} \tau_{31}^2 R_{\perp\perp}}{\sqrt{(\tau_{23}^2 R_{\perp\parallel}^2 + \tau_{31}^2 R_{\perp\perp}^2) (\tau_{23}^2 + \tau_{31}^2)}} \quad (4.55)$$

Finally, substituting these results into the failure criteria, Equation (4.38), leads to Equation (4.56).

$$\begin{aligned} \left(\frac{\tau_{23}}{R_{\perp\perp}}\right)^2 + \left(\frac{\tau_{31}}{R_{\perp\parallel}}\right)^2 + 2 \left(\frac{p_{\perp\perp}^c \tau_{23}^2}{R_{\perp\perp}} + \frac{p_{\perp\parallel}^c \tau_{31}^2}{R_{\perp\parallel}}\right) \frac{\sigma_{33}}{\tau_{23}^2 + \tau_{31}^2} = 1 \quad \text{if } \sigma_{33} < 0 \\ \left(\frac{\tau_{23}}{R_{\perp\perp}}\right)^2 + \left(\frac{\tau_{31}}{R_{\perp\parallel}}\right)^2 + \frac{2(p_{\perp\perp}^t \tau_{23}^2 R_{\perp\parallel} + p_{\perp\parallel}^t \tau_{31}^2 R_{\perp\perp})}{\sqrt{(\tau_{23}^2 R_{\perp\parallel}^2 + \tau_{31}^2 R_{\perp\perp}^2) (\tau_{23}^2 + \tau_{31}^2)}} \left(\frac{\sigma_{33}}{R_{\perp}^t}\right) \\ + \left(1 - \left(\frac{p_{\perp\perp}^t \tau_{23}^2}{R_{\perp\perp}} + \frac{p_{\perp\parallel}^t \tau_{31}^2}{R_{\perp\parallel}}\right) \frac{2R_{\perp}^t}{\tau_{23}^2 + \tau_{31}^2}\right) \left(\frac{\sigma_{33}}{R_{\perp}^t}\right)^2 = 1 \quad \text{if } \sigma_{33} \geq 0 \end{aligned} \quad (4.56)$$

Inspecting Equation (4.56), the following can be deduced. For a compressive transverse normal stress, all quantities on the last term of the left hand side are positive, except σ_3 itself. Hence, a compressive transverse normal stress delays delamination failure. Following the same logic, in case of a tensile transverse normal stress the third term of the left hand side is always positive. For the fourth and last term of this case, the terms after the minus sign have to be analysed. The squared shear stresses in both the nominator and the denominator cancel each other out. According to Table 4.2 the inclination parameters $p_{\parallel\parallel}^t$ and $p_{\perp\perp}^t$ are maximum 0.35. This leaves a ratio of $1/(2 \cdot 0.35) = 1.43$ for $R_{\perp}^t/R_{\perp\perp}$ and $R_{\perp}^t/R_{\perp\parallel}$ to make the last term on the left hand side always positive. After analysing several different kinds of CFRP and GFRP [33, 128, 142], the highest ratio found was 1.32 for the CFRP G40-800/5260 [128]. Hence, the total term after the minus sign will be lower than 1 for the analysed GFRP and CFRP materials. Thus, in contrary to a compressive transverse normal stress, a tensile stress will accelerate delamination failure. It is therefore essential to know if a transverse normal stress acting on a laminate is tensile or compressive, according to the inter-fibre failure theory of Puck.

4.2.3 Delamination Criteria Without Transverse Normal Stress

The most promising delamination criteria mentioned in the previous section (Brewer-Lagace, Puck) will be compared to each other while subjecting them to the case where the transverse normal stress is zero, and then compared to each other.

Ignoring the transverse normal stress in the Brewer-Lagace delamination criterion, Equation (4.46), simplifies it to Equation (4.57).

$$\left(\frac{\tau_{31}}{R_{31}}\right)^2 + \left(\frac{\tau_{23}}{R_{23}}\right)^2 = 1 \quad (4.57)$$

For Puck's failure criterion, neglecting the transverse normal stress in Equation (4.56) leads to Equation (4.58).

$$\left(\frac{\tau_{23}}{R_{\perp\perp}}\right)^2 + \left(\frac{\tau_{31}}{R_{\perp\parallel}}\right)^2 = 1 \quad (4.58)$$

Since the shear strength parallel to the fibres is the 23-direction, $R_{23} = R_{\perp\perp}$. Furthermore, the shear strength perpendicular to the fibres is either the 12-direction or the 31-direction, $R_{31} = R_{\perp\parallel}$. Hence, neglecting the transverse normal stress will lead to the same results according to the theory of Puck and the theory of Brewer and Lagace.

4.2.4 Implementation

For detection of onset of delamination, the only equation that needs to be implemented is the resulting failure criterion of the previous section, Equation (4.59). The location of this implementation is in the subroutine `umatXXv`, there all the needed stresses and strengths are available, plus this is the location where the in-plane failures are calculated as well.

$$D_i = \left(\frac{\tau_{31}}{R_{31}}\right)^2 + \left(\frac{\tau_{23}}{R_{23}}\right)^2 \quad (4.59)$$

As soon as the failure index for delamination D_i is larger than one, delamination is detected. What happens once there is delamination in an element, is the topic of the next chapter.

4.3 Summary

In this section, first the main conclusions of this chapter are presented. This is followed by an outlook on future work, based on the results of prediction of onset of delamination using the BLT element.

4.3.1 Conclusion

A method has been found in literature which is capable of predicting the transverse shear stresses in a 4-node element in explicit FEA due to applied transverse loads. Due to the limitation of using only symmetrical laminates, the maximum transverse shear stress was always found in the middle of the laminate. An example on 6 quasi-isotropic laminates showed that homogenizing the material through thickness, as done in an ESL approach, will cause errors in the predicted transverse shear stresses. An under prediction of 33% and an over

prediction of 31% were the highest values obtained for these 6 laminates. No solutions were found to predict the transverse normal stresses inside the 4-node element based on FSDT.

To determine what level of transverse normal stress would lead to delamination, several delamination failure criteria were examined. In the absence of transverse normal stresses, it was found that several failure criteria, including the Brewer-Lagace quadratic failure criterion and the fracture plane failure criterion of Alfred Puck, are equivalent to each other. Due to the quadratic transverse shear stress distribution through thickness, delamination onset is always predicted at the mid-plane of the laminate.

4.3.2 Outlook

To increase the accuracy of the prediction of onset of delamination, methods to predict the transverse normal stress need to be implemented. For transverse normal stresses caused by curvature effects, changing to a 8-node element would be enough to cover these. For transverse normal stresses due to applied transverse loads, the FEA code needs to be able to define on which surface (top or bottom) this load is acting, and whether it is a tensile or compressive load.

To further increase the accuracy of the prediction of delamination, more sources of transverse shear stresses need to be incorporated. One source of these stresses, the free edge effect, is highly dependent on the stacking sequence of the laminate. This will be a problem for the use in an ESL method, since it eliminates this information in the FEA input.

If a new method to incorporate the prediction of transverse normal stresses in the BLT element is developed, a new critical reflection of the used delamination failure criterion is needed. Three questions will need to be covered in this reflection:

- Should matrix tension failure be separated from matrix compression failure?
- Should matrix shear failure along the fibres be separated from shear failure perpendicular to the fibres?
- Is there interaction between the transverse shear and transverse normal stresses?

To help answer these questions, comparisons can be made to experimental results. For instance, to evaluate the criteria on performance on delamination failure due to curved regions, the test results of unidirectional curved laminates by Martin [143] or Wimmer et al. [144] can be used. If the calculation of transverse stresses due to free edges would be implemented, comparison to test results of Crossman et al. [145] or Shalev [52] is possible.

Effects of Delamination

After a method for the initiation of delamination is implemented in the previous chapter, the next step is to analyse what the effects of a delamination are on the structural response of plates. Two leading authors in field, Reddy and Robbins [146,147], stated that the kinematics of delamination itself cannot be modelled using an ESL approach. For the implementation, this means that there is not a single solution capable of modelling all effects of delamination at once. Hence, every effect has to be analysed and found a solution for separately.

Section 5.1 analyses and quantifies the three main effects of delamination, being a reduction in compression strength, a change in membrane stiffness and a reduction in bending stiffness. After concluding that the reduction in bending stiffness has the largest magnitude, this effect is chosen to implement in LS-Dyna in Section 5.2. The chapter continues in Section 5.3 with the results of the developed method and compares it to three-dimensional FEA results. Section 5.4 closes this chapter with the conclusions and an outlook for further work.

5.1 Analysis on Effects of Delamination

The literature review of Section 2.5.2 showed that the main effects of delamination on a laminate are a reduction in compression strength, membrane stiffness and bending stiffness. This section will analyse these three effects.

5.1.1 Compression Strength Reduction

Kutlu and Chang [69,70] concluded that the compressive strength of a panel containing delaminations can be severely lowered. The dominant source of reduction in compression strength of delaminated panels is sublaminates buckling, and multiple delaminations reduce the compression strength more than a single delamination does. However, buckling of sublaminates is out of the scope of this thesis, and therefore this effect is not included in further analysis.

5.1.2 Membrane Stiffness Reduction

The reduction of membrane stiffness as predicted and observed by Stalnaker and Stinchcomb [67] and O'Brien [68] can be described very well using a rule of mixtures approach, see Equation (5.1).

$$\mathbf{A}^* = \frac{1}{h} \sum_{i=1}^n \mathbf{A}_i t_i \quad (5.1)$$

In which \mathbf{A}^* is the equivalent membrane stiffness matrix, h is the total laminate thickness and \mathbf{A}_i and t_i are the membrane stiffness matrix and thickness of sublaminate i , respectively. When using this equation, the only possibility of having a reduced membrane stiffness is if the sublaminate have different poisson ratios. As explained in Chapter 4, the maximum transverse stresses are always predicted at the mid-plane of the laminate, hence delamination can be predicted only on this plane. Next, if also symmetrical laminates are assumed, the poisson ratio of the top and bottom sublaminate are equal. Furthermore, the use of an equivalent single layer model with homogenized material excludes the use of different poisson ratios for the sublaminate. Hence, there is no reliable way to include the reduction in membrane stiffness. The reduction in stiffness of 5% to 26% as reported by Stalnaker and Stinchcomb [67] and O'Brien [68] will therefore be ignored.

5.1.3 Bending Stiffness Reduction

Section 2.5.2 showed that by analysing the inertia of a one-dimensional delaminated beam without axial displacement compatibility, a reduction of 75% in bending stiffness is observed combined with a 50% reduction in maximum stress due to bending. With axial displacement compatibility, Tracy and Pardoen [72] showed that the reduction would be up to 43%, depending on the length of the delamination, delaminations of up to 40% of the length of the plate would see negligible stiffness reduction.

Comparing the magnitude of all previously mentioned effects, the focus of the remainder of this chapter will be on the effect with the largest magnitude, which is the bending stiffness reduction of a delaminated beam without axial displacement compatibility. Since this effect is coupled to the reduction in maximum stresses due to bending (see Figure 5.1), a delamination failure can be used in a beneficial way. Namely, for some structural parts of a car frame, an out-of-plane displacement is applied to the part for which catastrophic failure is allowed. In this case, the delamination would cause a lower bending stress and hence delay ply failure. Hence, the goal of the bending stiffness reduction is two-fold: not only should the resulting bending moment for a given displacement on a delaminated beam be 25% of the value for a undelaminated beam; the stresses due to bending should be halved as well.

How the reduction in bending stiffness and maximum bending stress is achieved is presented in the next section.

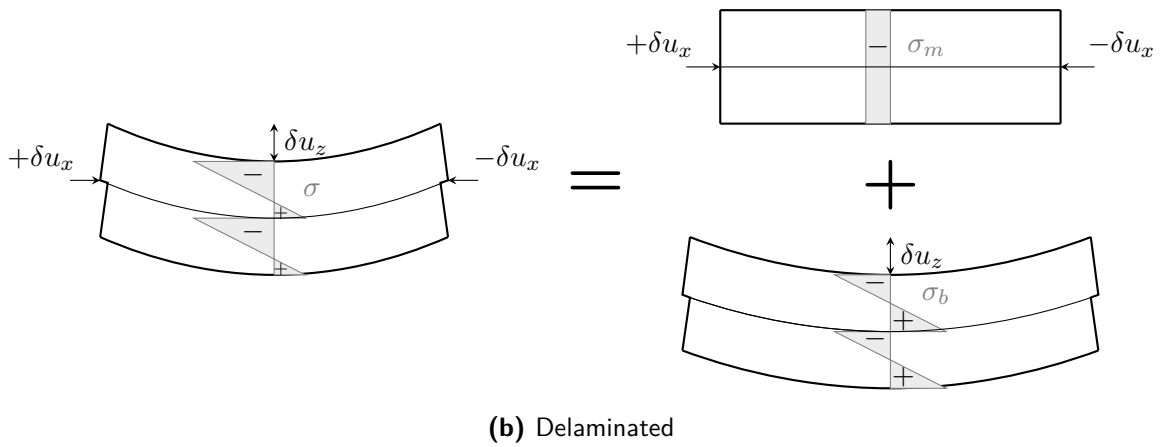
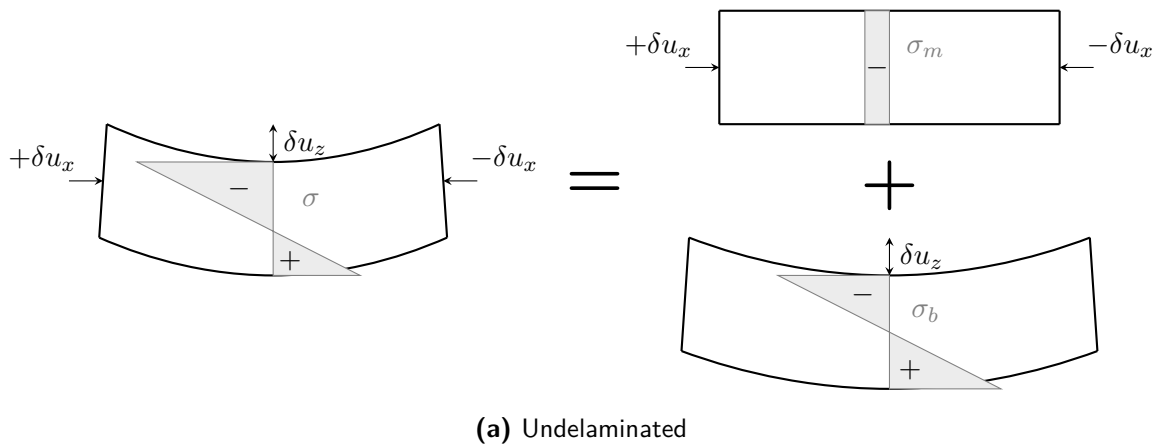


Figure 5.1: Stresses in bending beams

5.2 Implementation

The implementation of the reduction in bending stiffness is accomplished by a virtual strain reduction, which results in adjusting the strains obtained due to bending, while keeping the strains due to membrane loading constant. This is done by letting the integration points of the element simulate one sublaminates, and later multiply the resulting forces and moments by the number of sublaminates in the delaminated element. To investigate how this can be done, first the techniques used for the implementation of in-plane damage in LS-Dyna are examined in Section 5.2.1. When possible, these are used for the implementation of the virtual strain reduction as explained in Section 5.2.2. Once the method of how to reduce the bending stiffness is covered, a method to cover the problem of axial displacement compatibility is presented in Section 5.2.3.

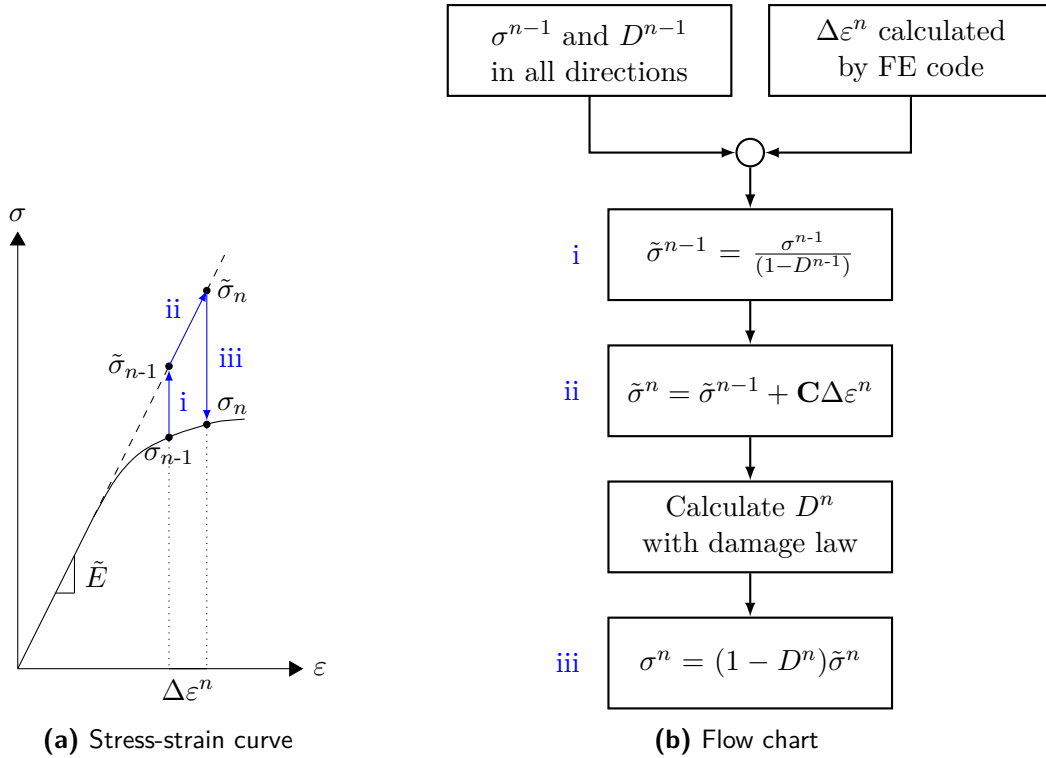


Figure 5.2: Calculation of stresses in case of non-linear material behaviour, with a stress-based failure model calculating the damage by using the undamaged stress

5.2.1 In-Plane Strength and Damage Evolution

In crash simulations, not only the point up to first failure is of interest, but also the damage evolution like the crushing of composites as explained in Section 2.4.2. For in-plane failure, a stress-based failure criterion is used (initial failure). The stiffness will be reduced by a factor depending on the damage mode, i.e. a softening curve as in Figure 5.2a will be used. For instance, for a compressive crushing mode the stiffness will be reduced to nearly zero. Then, if a certain threshold strain on an integration point is applied, it will be deleted. Finally, when a user-defined number of integration points of an element is deleted, the whole element is deleted (final failure).

While in-plane failure can be incorporated by adjusting the stresses using the method of Figure 5.2 on integration point level, this is not the case for delamination. For instance, delamination on the mid-plane surface would have an effect on the stress calculation of the outer integration points due to reduction of bending stiffness of the whole laminate. Furthermore, the calculation of forces and moments is done using the same stresses inside the element calculations. Hence, to adjust this, not only needs delamination to be detected in the material on an integration point level as was presented in Chapter 4, the effects of delamination need to be modelled in the element calculations.

5.2.2 Virtual Strain Reduction

Since the goal of the bending stiffness reduction is two-fold, i.e. reduction of bending stiffness by 75% and reduction of the stresses due to bending by 50%, implementing a separate bending stiffness would not work, as only one of the two goals can be reached. Furthermore, if the stress distribution could be directly changed from the undelaminated case to the delaminated case of Figure 5.1, an inaccuracy would arise when calculating the resulting bending moment: the BLT element relies on a Gauss quadrature integration for the bending moment out of the stresses, with 5 integration points through thickness. The inaccuracy then comes from applying Gauss quadrature to a function with a step in it. Furthermore, if a delamination occurs on one of the integration points, it would have two stresses simultaneously. Hence, a solution comprised of several steps is needed, which does not make use of a function which has a step function in it.

Looking at the internal force calculation of the BLT element, the stresses are calculated by application of a material model law to the strains, which are in turn obtained by a summation of the all strain increments over the time steps. The strain increments are calculated using the velocity-strain relations, see Equations (3.7) to (3.11).

$$d_{xx} = v_{x,x} + z\omega_{y,x} \quad (3.7 \text{ revisited})$$

$$d_{yy} = v_{y,y} - z\omega_{x,y} \quad (3.8 \text{ revisited})$$

$$d_{xy} = v_{x,y} + v_{y,x} + z(\omega_{y,y} - \omega_{x,x}) \quad (3.9 \text{ revisited})$$

$$d_{xz} = v_{z,x} + \omega_y \quad (3.10 \text{ revisited})$$

$$d_{yz} = v_{z,y} - \omega_x \quad (3.11 \text{ revisited})$$

To distinguish between strains due to bending and membrane loading, first the average strain over all integration point is calculated as the strain vector $\boldsymbol{\varepsilon}_0$, which is equal to strain due to membrane loading. To adjust for the reduction of strain due to bending in the case of a delamination, the strain is calculated by the average of the undamaged strain and the average strain weighted by the amount of damage, see Equation (5.2).

$$\boldsymbol{\varepsilon}_j = (1 - D_r)\boldsymbol{\varepsilon}_0 + D_r\tilde{\boldsymbol{\varepsilon}}_j \quad (5.2)$$

With $\tilde{\boldsymbol{\varepsilon}}_j$ the undamaged strain at integration point j , D_r the delamination damage factor and the vector

$$\boldsymbol{\varepsilon} = [\varepsilon_{xx} \quad \varepsilon_{yy} \quad \gamma_{xy}]^T$$

A damage factor of 1 corresponds to no delamination, a factor of 0.5 corresponds to one delamination on the mid-plane. There is a possibility to add friction as a stiffening factor, for instance by applying a factor of $0.5 < D_r < 1$ on a lamination with one mid-plane delamination. Exploitation of this option is out of the scope of this thesis, and up for recommended further work. Using a material law, the strains of Equation (5.2) are converted into stresses. Therefore, applying a delamination factor of 0.5 on a laminate with a single delamination, satisfies the requirement of reduction of the stresses due to bending by half without reducing the membrane stresses. This means that the average stress does not change, and integration of the stresses over the thickness will result in the same force resultant.

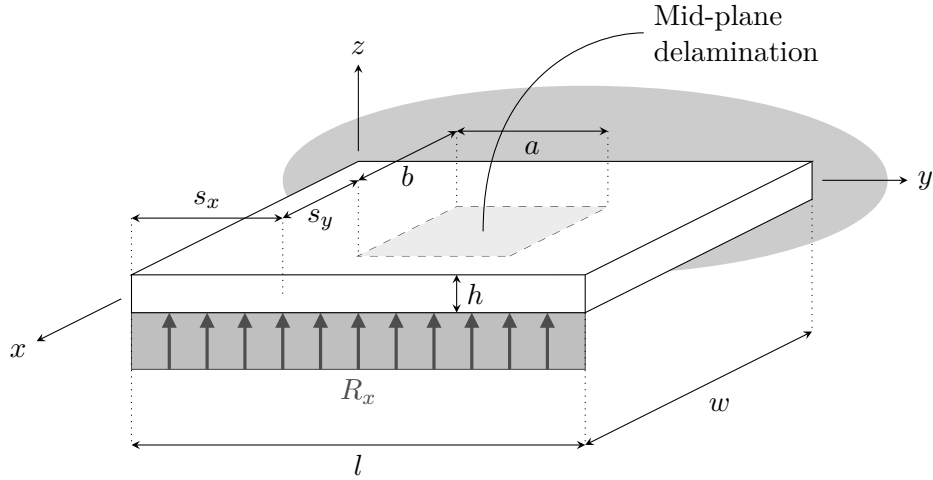


Figure 5.3: Cantilever plate with two-dimensional delamination

$$m_{xI} = A \left(\mathcal{B}_{2I} \int_{-h/2}^{h/2} z \sigma_y dz + \mathcal{B}_{1I} \int_{-h/2}^{h/2} z \sigma_{xy} dz - \frac{1}{4} k \int_{-h/2}^{h/2} \sigma_{yz} dz \right) \quad (3.29 \text{ revisited})$$

$$m_{yI} = A \left(-\mathcal{B}_{1I} \int_{-h/2}^{h/2} z \sigma_x dz + \mathcal{B}_{2I} \int_{-h/2}^{h/2} z \sigma_{xy} dz + \frac{1}{4} k \int_{-h/2}^{h/2} \sigma_{xz} dz \right) \quad (3.30 \text{ revisited})$$

With the in-plane stresses due to bending being reduced by half, this means that the moments in Equations (3.29) and (3.30) will be reduced by half as well. This, while the requirement for the moments was a reduction of 75% for a given applied displacement. Therefore, in the calculation of the nodal moments, the factor D_r needs to be applied another time. Since the transverse shear stiffness should not change, the factor should not be applied to the last integral of Equations (3.29) and (3.30); the result is Equations (5.3) and (5.4).

$$m_{xI} = A \left(D_r \mathcal{B}_{2I} \int_{-h/2}^{h/2} z \sigma_y dz + D_r \mathcal{B}_{1I} \int_{-h/2}^{h/2} z \sigma_{xy} dz - \frac{1}{4} k \int_{-h/2}^{h/2} \sigma_{yz} dz \right) \quad (5.3)$$

$$m_{yI} = A \left(-D_r \mathcal{B}_{1I} \int_{-h/2}^{h/2} z \sigma_x dz + D_r \mathcal{B}_{2I} \int_{-h/2}^{h/2} z \sigma_{xy} dz + \frac{1}{4} k \int_{-h/2}^{h/2} \sigma_{xz} dz \right) \quad (5.4)$$

5.2.3 Free Edge Indicator

The implementation of the reduction in bending stiffness would be relatively easy for a one-dimensional delamination; only when the delamination has no possibility for shear transfer at one of its ends, the bending stiffness would be reduced. However, the problem becomes more complex when looking at a two-dimensional delamination; take for instance the rectangular cantilever plate containing a delamination of length a and width b of Figure 5.3. The delamination has a distance from the edges of s_x at $x = l$ and s_y at $y = w$.

Several three-dimensional FEA models have been made to understand what the requirements on the delamination would be to cause a reduction in bending stiffness. These models were

built up using constant stress hexahedron elements, which are the default solid element in LS-Dyna [76]. Furthermore, frictionless contact was applied on all elements, and an isotropic material was chosen. A delamination was modelled by disconnecting the top from the bottom half of the plate at the location of the delamination. The models had a line load at $x = l$, the dimensions $l = w$, $h = l/10$, $a = b = w/2$ and s_x and s_y were varied. The results showed that only for $s_x = s_y = 0$, i.e. the case when the delamination reaches two free edges, a reduction in bending stiffness was noticed. For the other cases, the axial displacement compatibility prevents the two sublaminates from sliding over each other.

To see whether the order of magnitude of the reduction in bending stiffness was comparable to the 75% of only taking into account the reduction in area moment of inertia, the plate was then modelled with BLT elements. Since the method described in the previous section is not yet implemented in LS-Dyna, the delaminated area was modelled in a comparable way. At the location of delamination, the thickness of the elements was set at $h/2$. Next, these elements were duplicated on the same nodes. While this is physically impossible since it has two elements occupying the same physical space, it does replicate the stress distribution of Figure 5.1b and hence the same bending stiffness. The results showed good agreement on the displacements of the plate, as can be seen in Figure 5.4.

The results of the previous two paragraphs leads to the following observation: to reduce the bending stiffness of a plate by 75% due to delamination, the delamination should have progressed to two perpendicular free edges. To include this in the user modules of LS-Dyna, a new parameter is introduced which is stored on each node of the mesh: D_f . On each node this parameter can have the following three integer values:

- $D_f = 0$: This node is neither part of any free edge, nor connected to one via a continuous delamination
- $D_f = 1$: This node is part of one free edge or connected to one via a continuous delamination
- $D_f = 2$: This node is part of two perpendicular free edges, or connected to them via a continuous delamination

During the damage calculation in each time step in the analysis, D_f is updated. If the element is not delaminated, i.e. $D_r = 1$, the values of the flags are not changed. If the element is delaminated, the maximum of the four flags of the element is taken, and assigned

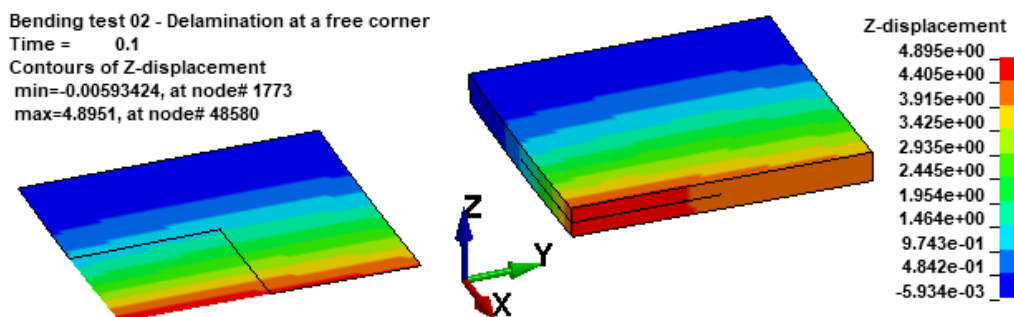


Figure 5.4: Modelling of a cantilever square plate with a delamination at the corner, brick elements versus plate elements

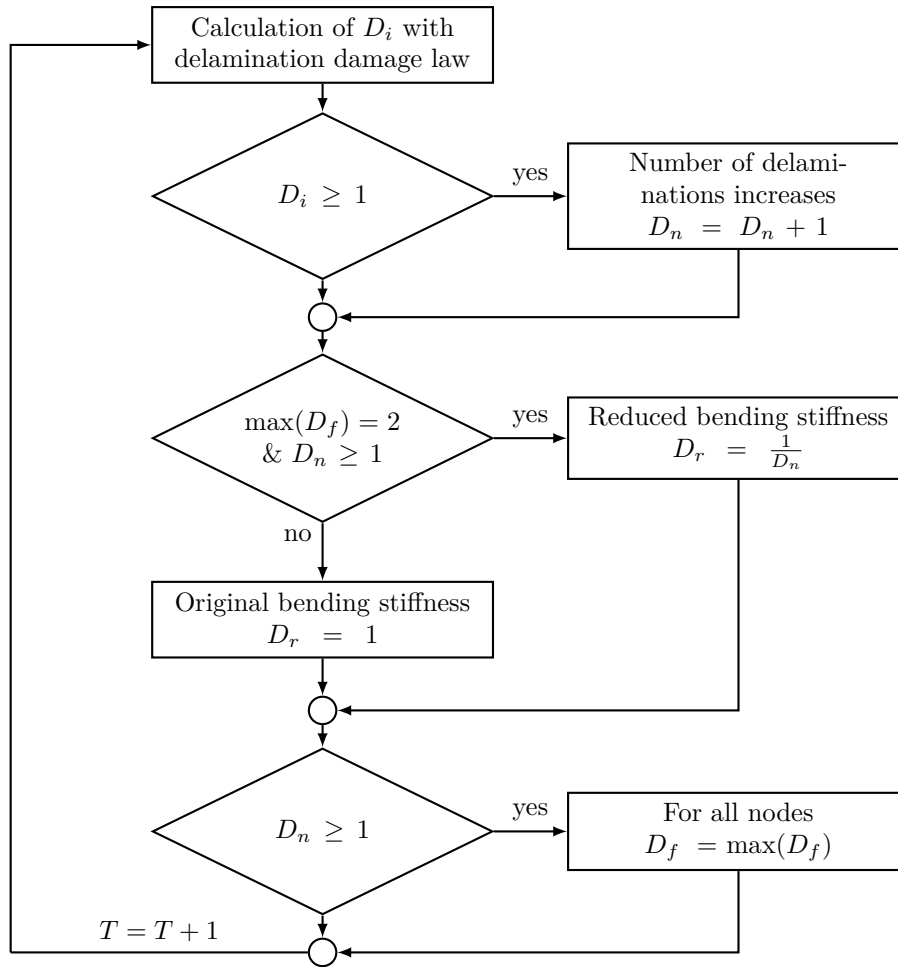


Figure 5.5: Flow chart of all delamination parameters

to all four nodes. For a flow chart of all delamination parameters D_i , D_n , D_r , and D_f in the calculation of a single element, see Figure 5.5. Furthermore, two examples are given below for clarification.

Example 1

This example shows the evolution of the delamination free edge flags on a cantilever square plate with delamination starting at a corner, see Figure 5.6. At the start of the analysis no delamination is present, and hence only the nodes at the free edges are given non-zero flag.

Due to an arbitrary loading, at time step $T=1000$ the element at a free corner of the plate delaminates. Since the lower left node of the element has a free edge flag of 2, the delamination immediately causes a reduced bending stiffness. At the end of the time step, the delamination causes the propagation of the $D_f = 2$ to all the nodes of the element.

As the plate is further loaded, at time step $T=2000$ the delamination progresses one element inwards. Since at this element the two nodes on the right side have $D_f = 2$, the delamination

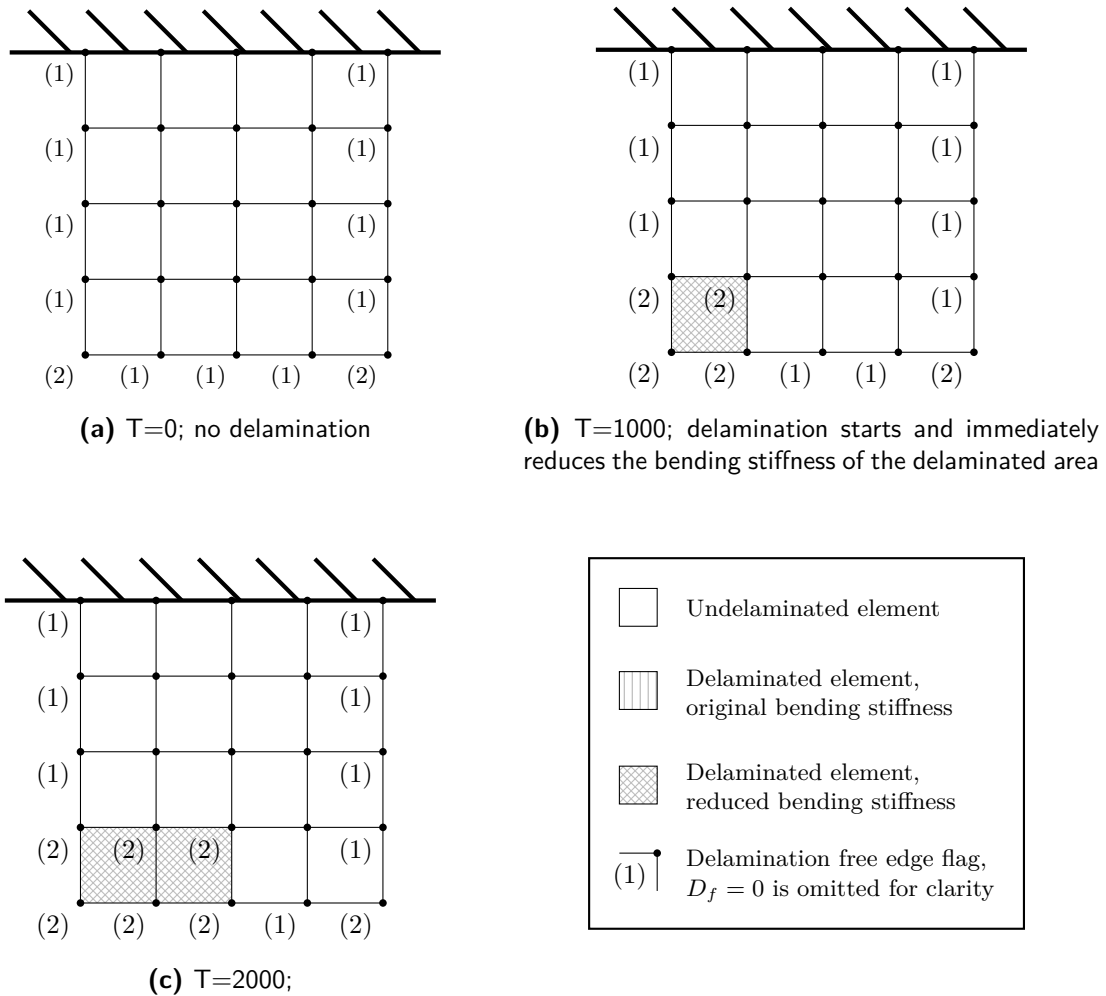


Figure 5.6: Example 1 on development of bending stiffness reduction: delamination starting at the corner of a cantilever plate

again causes an immediate reduction in bending stiffness, followed by setting the flag for all nodes of this element at $D_f = 2$.

Example 2

This example shows the evolution of the delamination free edge flags on a cantilever square plate with delamination starting at the middle of the free side of the plate. The start of the analysis is identical to the previous example, see Figure 5.7.

Due to a different arbitrary loading, at time step $T=1000$ one of the middle elements at the free side of the plate delaminates. Since the maximum value of the free edge flag of the four nodes is 1, the bending stiffness of the element is not affected. Afterwards, the delamination causes the propagation of the $D_f = 1$ to all the nodes of the element.

As the plate is further loaded, at time step $T=2000$ the delamination progresses one element inwards. Again there is no delamination flag of 2 so the bending stiffness is not affected, and

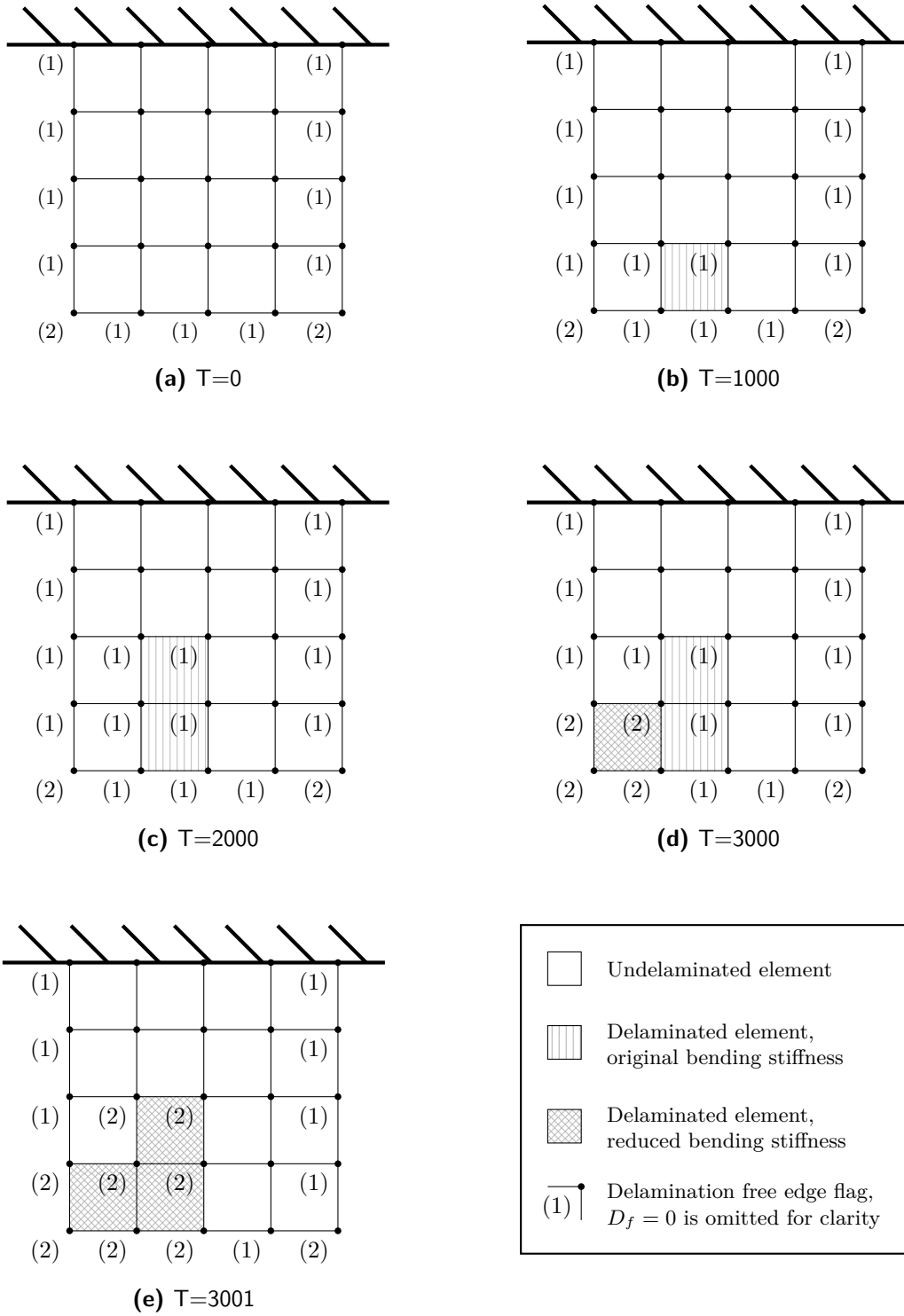


Figure 5.7: Example 2 on development of bending stiffness reduction: delamination starting in the middle of the free side of a cantilever plate

afterwards all flags of the element are set to $D_f = 1$.

Due to further development of the applied load, at time step $T=3000$ the delamination progresses to corner element, which has one node with $D_f = 2$ at the start of the time step. Therefore, this element has its bending stiffness reduced by setting $D_r = 0.5$. However, since at the start of this time step the other two delaminated element have $\max(D_f) = 1$, they do not see a reduced bending strain. At the end of the time step, all nodes belonging to the corner element get $D_f = 2$.

At the start of the next time step, all delaminated elements contain at least one node with $D_f = 2$. Hence, the bending stiffness of all these elements is reduced by setting $D_r = 0.5$. At the end of the time step, the delamination flags follow by setting the flag of all nodes of the delaminated elements to $D_f = 2$.

The use of this delamination flag has as added benefit that it identifies nodes which are part of the free edges and delamination crack fronts. These are the locations at which delamination cracks are known to initiate or propagate at global stress levels way below the undamaged interlaminar strength because of stress concentrations due to local effects as was explained in Section 2.5.1. While this is beyond the scope of this thesis, it leaves the possibility open to use the delamination flag to include the effects of free edges and delamination growth.

5.3 Verification

To see how the accuracy is of the previously described methods, comparisons on different loaded plates have been made to three-dimensional FEA.

5.3.1 Model Descriptions

The two methods of modelling are compared by comparing the results on rectangular cantilever plates with a line load at the free side of the plate. All analyses are done using the explicit solver of LS-Dyna, to minimize the number of differences between these comparisons and usage of the methods in a real case. The strains, and therefore the stresses, are derived from the displacements and are thus a function of them. Therefore, the displacement of the plates are the entity which is compared, in particular, the out-of-plane displacement u_z across the whole plate. The plates are of isotropic material; aluminium with $E = 71700$ MPa and $\nu = 0.33$. Furthermore, they contain a delamination up to the corner of the free side of the plate. In total five plates are analysed:

0. A square plate without any delaminations to act as the benchmark to indicate the error between shells and bricks for this geometry; see Figure 5.8a.
1. A square plate with a one-dimensional delamination spanning half the length of the plate; see Figure 5.8b.
2. A square plate with a delamination spanning half the length and width of the plate; see Figure 5.8c.
3. A square plate with a square delamination almost reaching the root and the third free edge; see Figure 5.8d.
4. A square plate with a half-width delamination from the root to free side; see Figure 5.8e.

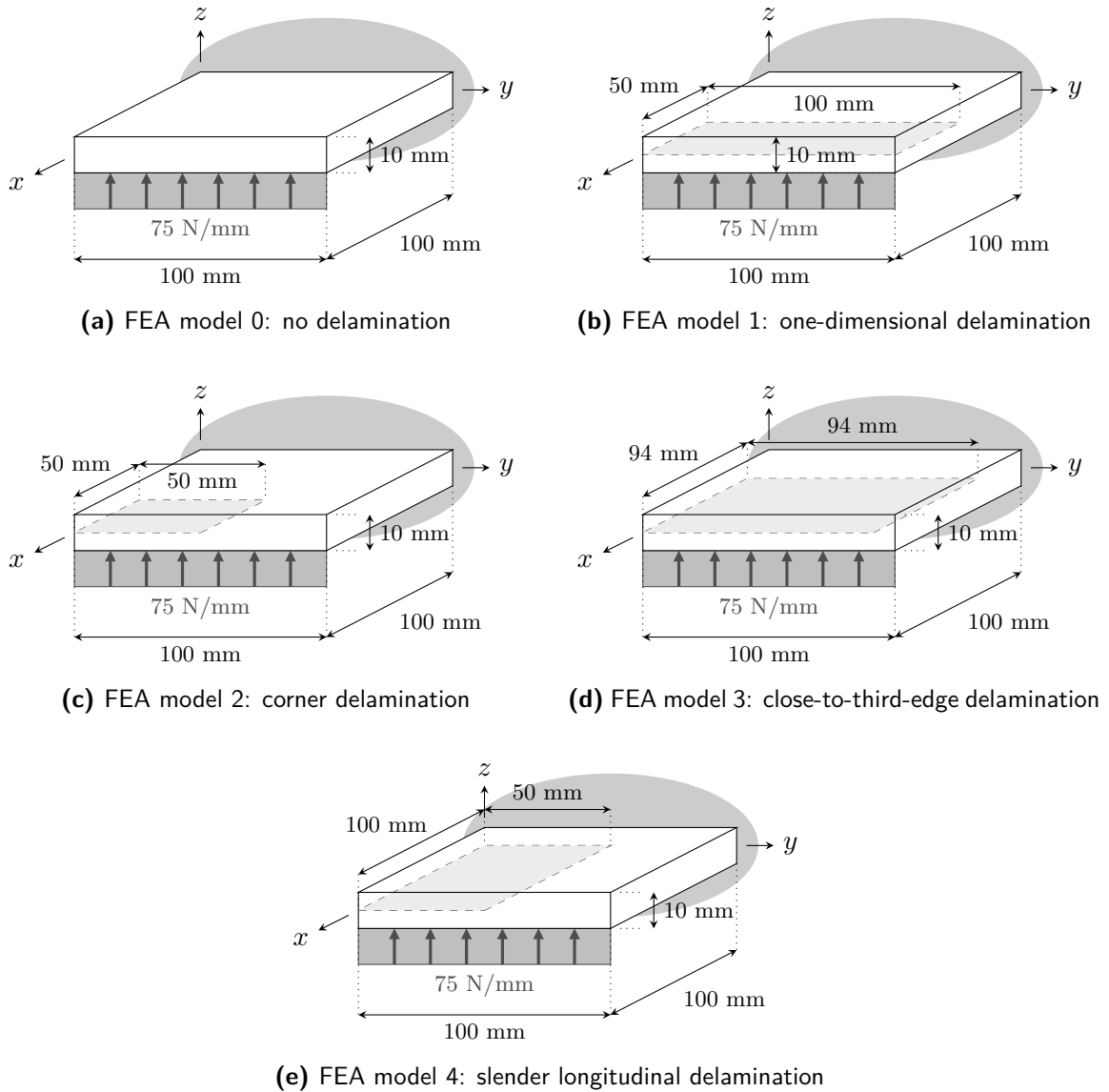


Figure 5.8: Geometrical specifications of the five used FEA models

The three-dimensional brick models are built up as follows. The plates are modelled with 10 elements through thickness, with the length and width of an element twice its thickness. A delamination is modelled by disconnecting the top from the bottom half at the desired location. The line load R_x is distributed through the thickness, creating forces on the nodes with their magnitude weighted to the amount of free side surface they represent.

Since the methods to model delamination in the BLT element are not yet implemented in the user modules of LS-Dyna, the shell element models are constructed in the same way as done in Section 5.2.3. The delaminations are modelled by having two elements of half the plate thickness at the same location, sharing the nodes. This makes sure the nodal forces and moments mimic the behaviour of a delaminated plate without axial displacement compatibility. The line load R_x is distributed to the nodes, again with their magnitude

weighted to the amount of free side surface they represent.

5.3.2 Results

The results show varying success for the different types of delamination shapes and locations. For a visual representation of the out-of-plane displacement of all 5 cases, see Figures 5.9 to 5.13. The maximum displacements, the error in maximum displacement and the average error on all nodes are given in Table 5.1. In these figures and table, a positive error means an over prediction of the displacement of the proposed method using shell elements, when compared to the brick element model.

The FEA for a cantilever square plate without delaminations, visualised in Figure 5.9, shows that the error in maximum displacement is 5.9% when comparing a model built up with shell elements to a model built up with brick elements. The error on the out-of-plane displacement, averaged over all nodes at least two plate thicknesses away from the clamping area, is higher at 7.1%. This gives a benchmark to compare the errors to of the remaining 4 tests.

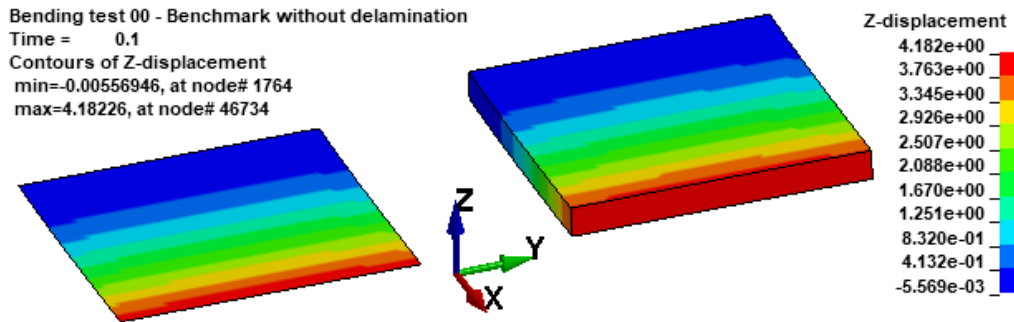
Figure 5.10 shows the results on the first test case: a cantilever plate with a delamination starting at half the length of the plate until the tip, which can be seen as the case of a one-dimensional delamination. Compared to the benchmark result, the errors on the maximum displacement and the average error are slightly higher, 7.0% and 9.5% respectively. When comparing the distribution of the error over the plate, i.e. Figure 5.10b to Figure 5.9b, it can be seen that profile is the same, only the error on the plate with delamination is 2% higher. Hence, the proposed method of modelling delamination in shell elements is very well suited for one-dimensional delaminations.

The next plate analysed is the cantilever plate with a delamination of moderate size at a free corner of the plate, spanning half the width and half the length. The results are found in Figure 5.11. Again the error in maximum displacement and the average error are comparable to the benchmark case: 7.6% and 8.8%, respectively. However, when looking at the error distribution over the plate in Figure 5.11b, it can be seen that the error is higher on the edge which does not have the delamination. This means that the displacement obtained in the

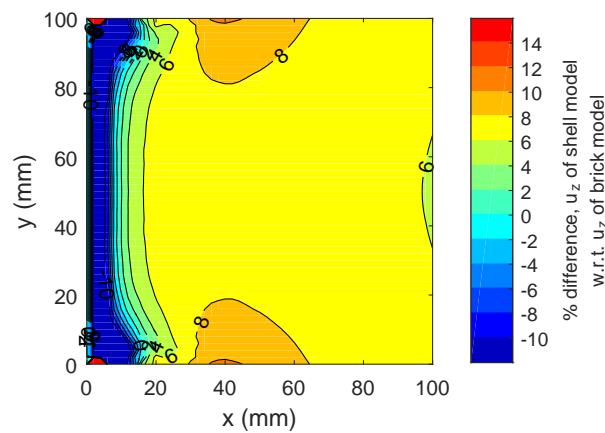
Table 5.1: Results of the comparison with 3D FEA

| Delamination type | $\max(u_z)$ (mm) | | Error | |
|----------------------|------------------|--------|-------------|----------------------|
| | Bricks | Shells | $\max(u_z)$ | Average ¹ |
| 0: None | 3.95 | 4.18 | +5.9% | +7.1% |
| 1: 1D | 5.51 | 5.90 | +7.0% | +9.5% |
| 2: Corner | 4.55 | 4.90 | +7.6% | +8.8% |
| 3: Close to 3rd edge | 10.47 | 13.95 | +33.2% | +49.7% |
| 4: Slender | 6.24 | 7.97 | +27.8% | +39.4% |

¹ For the average error in displacement, the rows of nodes close to the clamping (within two plate thicknesses) are omitted. This is to prevent the effects of clamping cluttering the results.



(a) FEA of the shell and brick models

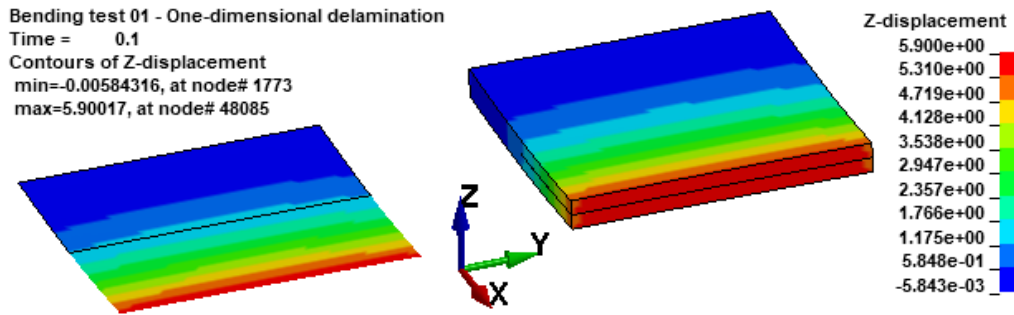


(b) Error on out-of-plane displacement

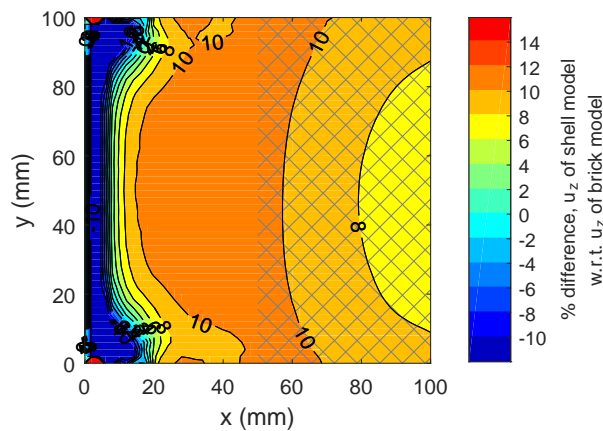
Figure 5.9: Results of the cantilever plate without delamination, comparing brick elements to the proposed method using shell elements

proposed method with shell elements comes more due to a rotation about the y -axis than the brick elements model, and less due to a rotation about the x -axis. The reason for this is that the edge of the delamination at half of the plate width does not cause an axial displacement compatibility for the shell model as strong as the one for the brick model. However, the overall displacement response of the shell model still replicates the brick model as well as the benchmark results, and hence, the proposed method can be used for delaminations of moderate size as well.

The third test case is for a cantilever plate in which a corner delamination almost reaches the third free edge, i.e. it is almost progressed from a two-dimensional delamination to a one-dimensional one. As can be seen from the results in Figure 5.12, both the profile of the out-of-plane delamination as well as the magnitude cannot be covered well by the proposed solution. This can be seen from the error in maximum displacement (33.2%) and the average error in out-of-plane displacement (49.7%) as well. The reason for this is the same as for the previous test case: the axial displacement compatibility condition at the crack front parallel to the x -axis is not as strong in the shell model as in the brick model. This causes a stiffer non-delaminated part for the brick model, which is reflected in the profile of the



(a) FEA of the shell and brick models



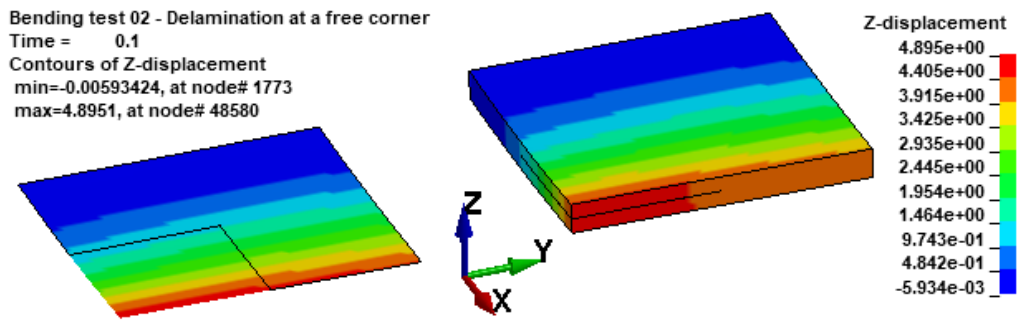
(b) Error on out-of-plane displacement; hatched area is the delamination

Figure 5.10: Results of the cantilever plate with a one-dimensional delamination, comparing brick elements to the proposed method using shell elements

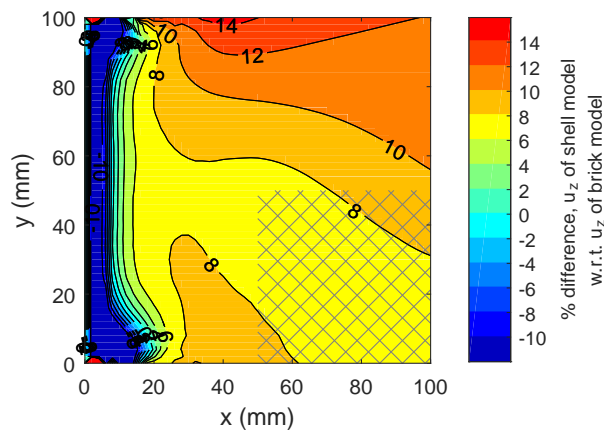
out-of-plane displacement, as can be seen from Figure 5.12b. Hence, for the case where a two-dimensional delamination is on the brink of reaching another free edge and hence becoming a one-dimensional delamination, the proposed method using shell elements cannot predict the bending stiffness of the plate accurately.

Figure 5.13 presents the results on the final test case; delamination over half of the width of the cantilever plate, reaching from the root until the tip of the plate. The proposed method does not provide an accurate representation of the structure when compared to the brick model, with an error in maximum displacement of 27.8% and an average error of 39.4%. The reason for the high differences can again be found in the axial displacement compatibility at half width leading to an under prediction of the bending stiffness for the proposed method using shell elements. So, also for plates containing a delamination with a high aspect ratio, the proposed method does not capture the bending stiffness of the plate accurately. However, for all the test cases including the method is still better than not including it when using an ESL method with delamination, as can be seen when comparing the maximum out-of-plane displacements in Table 5.1.

It should be noted that the tests were all done with isotropic materials, whereas the intention of the method is to be used with CFRP materials. The CFRP laminates will however be



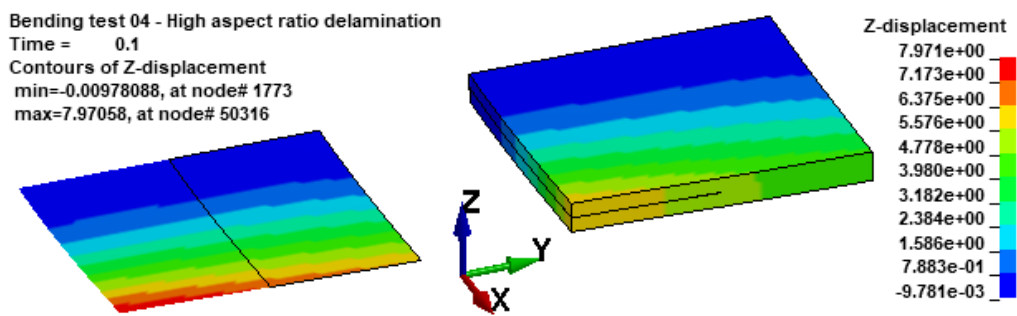
(a) FEA of the shell and brick models



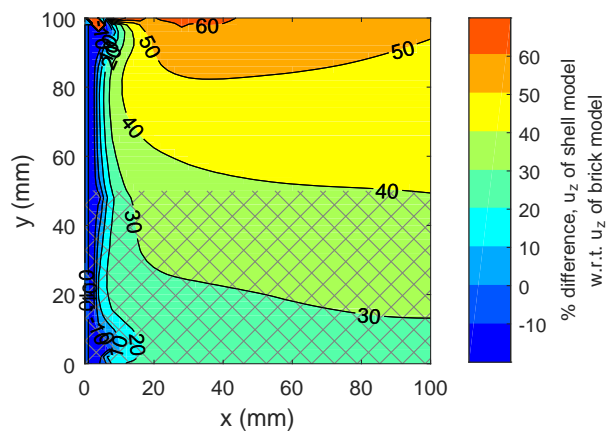
(b) Error on out-of-plane displacement; hatched area is the delamination

Figure 5.11: Results of the cantilever plate with a two-dimensional delamination at a free corner, comparing brick elements to the proposed method using shell elements

homogenized through thickness, as was explained in Sections 2.2.2 and 4.1.4. Because of the homogenization, the results obtained with an isotropic material can be used for verification. If any errors occur because of the difference in material, it is expected these are due to the homogenization, as was discussed in the two previously mentioned sections.



(a) FEA of the shell and brick models



(b) Error on out-of-plane displacement; hatched area is the delamination

Figure 5.13: Results of the cantilever plate with a two-dimensional delamination from root to tip over half the width of the plate, comparing brick elements to the proposed method using shell elements

5.4 Summary

In this section, first the main conclusions of this chapter are presented. This is followed by an outlook on future work.

5.4.1 Conclusion

After a literature review on the effects of delamination on the structural response of a plate under loading, it was found that the effect with the most impact on the results is the reduction in bending stiffness and bending stresses when a delamination does not have an axial displacement compatibility at its end. By looking at the inertia and stress distribution of a delaminated plate, it was found that the stress due to bending should be halved, while the bending stiffness should be 25% of the value of the original plate in the case of a mid-plane delamination. Axial displacement compatibility is easy to identify for the case of a one-dimensional (i.e. through the width) delamination, since it should be progressed to the tip of the plate. For a two-dimensional delamination, an algorithm was developed which identifies if an element is part of two perpendicular free edges or connected to them via a continuous delamination. If this is the case, the element should have its bending behaviour changed. This is done by first halving the strains due to bending inside an element. These strains are then converted to stresses using a standard material law, covering the effect of halving the stresses due to bending. Next, to satisfy the requirement reducing the bending stiffness by 75%, the moments calculated by integration of the new bending stresses should again be halved.

Due to time constraints on the project, implementation in the user modules of LS-Dyna was not possible. However, the proposed method could still be compared to more detailed brick FEA models. This was done by placing two elements of half thickness at the location of delamination. By first comparing the out-of-plane displacement results for shell elements to brick elements for a plate without any delaminations, a benchmark results was obtained to compare the other four test cases to. This benchmark FEA showed an over prediction of the displacement of the model with shell elements of 7.1%, when looking at the average error over the whole plate. The two first test cases, a one-dimensional delamination and a delamination of moderate size, showed satisfactory results with an average error in displacement of 9.5% and 8.8%, respectively. However, the method was not able to accurately predict the bending response for all four tested cases. Especially when a plate included an axial displacement compatibility transverse to the loading direction the results were unsatisfactory, which was the case with high-aspect ratio delaminations (average error of 39.4%) or delaminations on the brink of progressing to a third free edge (average error of 49.7%). For these cases, the results show an under prediction in bending stiffness, however, including the method provides more accurate displacement results than not including it. Furthermore, it is expected that for car crashes a delamination will quickly progress to the third free edge once it is close to it. Therefore, this case is unlikely to exist in car crash FEA for a long period of time.

To conclude, if an under prediction in stiffness leads to a robust design, implementation of this method is advised, as this method shows a clear benefit compared to no prediction of delamination. Also, in the stage of design where this method should be implemented (development of new car architecture concepts), the qualitative results are more important than the quantitative results. The main qualitative result is the opportunity to compare different design concepts, having the same differences to real delamination degradation.

5.4.2 Outlook

Even though the proposed method has been compared to detailed three-dimensional FEA by using an equivalent method, the actual implementation of the proposed method in the user modules of LS-Dyna would allow for verification and better validation of the method. Furthermore, this would allow for a better investigation as to why the axial displacement compatibility condition is not carried out very well when it is perpendicular to the main load path.

It may also be a benefit to implement the delamination in a way, that the effect of delamination could be scaled as some sort of material parameter, i.e. a bending reduction factor dependent on the layup. This parameter might be obtained by three-point bending tests from certain laminates as a function of anisotropy and lamination parameters, making the parameter a function of the stacking sequence.

While friction between sublaminates was not part of the scope of this thesis, the delamination damage factor, used to reduce the stresses due to bending and the bending stiffness, has been set up such that there is a possibility to include effects of friction as well. How the friction exactly affects the structural performance of a delaminated plate, is a possibility for further work.

Another possibility for further work is to include effects of free edges and delamination growth into the method. The delamination flag, used to identify when the axial displacement compatibility condition should be adhered to, can be a part of this as it also identifies which elements are part of a free edge or a delamination crack front.

To further improve the method, the two other main structural effects could be included as well, being a change in membrane stiffness and a reduction in compressive strength. The difficulty herein lies that both effects are largely dependent on the stacking sequence of the laminate and the through-the-thickness location of the delaminations and hence a lot of experiments and calibration would be needed to implement this in an ESL method. The reduction in bending stiffness for the case with axial displacement compatibility is also an effect which will increase the overall accuracy of the method. However, it is expected that implementing this kind of reduction in bending stiffness would come at a high computational cost.

Conclusions and Recommendations

The goal of this thesis was to answer the research question *How to detect and model delamination of laminated composites in an equivalent single layer model in explicit finite element analysis?*

To be able to answer this question, first a background was given on composites together with sources of the delamination failure mode. Then, a description of the most common way of modelling delamination in finite element analysis in general was given, which was done by using one shell or brick element per ply through thickness and connecting these elements with cohesive elements. However, since the goal of the equivalent single layer model was to eliminate the use of more elements through thickness, it was concluded that this approach could not be used in this thesis.

To further understand the problem, the most used element in explicit finite element analysis (the Belytschko-Lin-Tsay shell element [79]) was described to analyse possibilities to incorporate delamination failure in an equivalent single layer model. The conclusion was that the best way to answer the research question was to split the problem into two parts; the detection of delamination onset and the modelling of the effects of delamination. Furthermore, making use of the user modules of the commercial explicit finite element software package LS-Dyna would give a flexible but comprehensive basis to start with.

Next, the problem of delamination onset was analysed. The best method available to predict this in an equivalent single layer model which makes use of the Belytschko-Lin-Tsay element, was concluded to be calculating the transverse stresses inside an element, followed by the application of a stress-based failure criterion. It was possible to improve the accuracy of the transverse shear stresses from the solution of a Belytschko-Lin-Tsay element by making use of the method of Rolfes and Rohwer [103]. However, no solution was found which could calculate the transverse normal stresses without making rigorous adaptation to either the element scheme or the pre-processing. After a literature study, the failure theory of Puck [132] and the quadratic failure criterion of Brewer and Lagace [56] were selected to be the most promising failure criteria. Both were adapted for the use of pure delamination in the absence of transverse normal stresses, which led to the conclusion that under these circumstances they result in the same criterion.

The final part of this thesis tackled the effects of delamination and how they could be implemented into the user modules of LS-Dyna. From the start it was noted that modelling the kinematics of delaminations was not possible while making use of the equivalent single layer method, hence all effects were analysed and implemented separately. The most severe effect, a reduction of bending stiffness and stresses due to bending in the case of a delamination without axial displacement compatibility at the end, was selected to be analysed and implemented. It was concluded that for a mid-plane delamination with an equivalent single layer model, the maximum stresses due to bending should be decreased by 50%, while the bending stiffness should be reduced by 75%. The implementation was done by applying a delamination damage factor in the calculation of the stresses at an integration point. Then, the same damage factor was used in the calculation of the nodal moments, which led to the desired moment when a certain displacement is applied. Next, an algorithm was developed which identifies the elements without axial displacement compatibility. Then, a method was explained on how this approach could be implemented: by passing element information via the nodes. This made sure that only elements which are part of two perpendicular free edges, or connected to them via a continuous delamination, have their bending stiffness and stress reduced.

Since implementation of the previously described methods was not possible yet due to time constraints, the method was compared to more detailed finite element analysis in a different way. This was done by placing two elements of half thickness at the location of delamination. Using this equivalent method, a rectangular cantilever plate without delamination showed an average error in out-of-plane displacement of 7.1% and served as a benchmark result for the remaining test cases. Comparable errors of 9.5% and 8.8% were found for the test cases of a one-dimensional delamination and a delamination of moderate size at the corner of the plate, respectively. Hence, the proposed method of modelling the effect of bending stiffness reduction gave results with good agreement on these shapes of delamination. However, less satisfactory results were obtained for test cases with delaminations progressed close to a third free edge (error of 49.7%) and delaminations with high aspect ratios (error of 39.4%). However, including the method provided more accurate displacement results than not including it.

The first part of the research question therefore has the following answer: to detect delamination in an equivalent single layer model in explicit finite element analysis, the transverse shear stresses are recovered from the solution of a time step, followed by the application of a delamination failure criterion. The second part of the research question has the following result: to model the effects of delamination in the same framework, each effect has to be treated separately, leading to the use of a delamination damage factor to reduce the bending stiffness and stresses due to delamination.

Outlook

While this thesis provided an answer to the research question, it does not mean the answer cannot be improved upon. Sections 4.3.2 and 5.4.2 already gave recommendations for future work on the prediction of onset of delamination and on the modelling of the effects of delamination, respectively, and therefore they will not be repeated here. However, there are possible additions to the combination of the two parts and recommendations to the overall concept, which will be described in this section.

One large addition to the current method would be to include transverse stresses from other sources than only applied loads. Not only would this lead to better prediction of onset of delamination, it may also cause the first delamination to start on a different plane than the mid-plane of a laminate. This in turn would cause the need for a more detailed analysis on the two main effects of delamination besides a reduction in bending stiffness: a change in membrane stiffness and a reduced compression strength. The reason for this, is that sublaminates buckling is a large contributor to these two effects, a type of buckling which is more likely to occur on thinner sublaminates. In turn, sublaminates buckling may be an accelerator of delamination growth, especially if crack has an opening mode I (transverse tension).

This brings up the next recommendation for improvement of the current method: including a difference between the calculation of delamination growth versus delamination onset. A first version of this could be to implement a damage factor to reduce the interlaminar strength of an intact element whose neighbour has delaminated. A detection for this can be done by analysing the delamination free edge flag presented in Section 5.2.3. If not all node flags belonging to an element are equal to zero, one of the neighbouring elements is either a crack tip or a free edge. This would mean that a free edge will be treated as a crack tip, however, it is known that free edges are prone locations of delamination onset.

Finally, the overall concept of modelling using an equivalent single layer model for composites would benefit from distinguishing a membrane laminate stiffness from a bending laminate stiffness. While in the stage of car development where the equivalent single layer method is used relative large errors are expected, including three extra stiffnesses in the material card may be worth the while to reduce those errors. Section 2.2.2 showed that differences between bending and membrane stiffness could already be 68% for a quasi-isotropic layup. Implementation of these bending stiffnesses could be done by including a ratio of bending stiffness over membrane stiffness in the calculation of node moments.

References

- [1] Euro NCAP. Euro NCAP rating review - Report from the Ratings Group. Technical report, European New Car Assessment Programme, 2013.
- [2] NHTSA. New Car Assessment Program. Technical Report 241 (Docket No. NHTSA-2015-0119), National Highway Traffic Safety Administration, 2016.
- [3] R. Heuss, N. Mueller, W. Van Sinteren, A. Starke, and A. Tschiesner. Lightweight, heavy impact. Technical report, McKinsey & Company, 2012.
- [4] A. B. Lovins and D. R. Cramer. Hypercars, hydrogen, and the automotive transition. *International Journal of Vehicle Design*, 35(1/2):50, 2004.
- [5] N. Hu, A. Elmarakbi, Alamusi, Y. Liu, H. Fukunaga, S. Atobe, and T. Watanabe. Numerical simulation of damages in FRP laminated structures under transverse quasi-static or low-velocity impact loads. In A. Elmarakbi, editor, *Advanced composite materials for automotive applications: structural integrity and crashworthiness*, chapter 11, pages 257–292. Wiley, Chichester, 2014.
- [6] ERTRAC. European Roadmap Safe Road Transport, 2011.
- [7] J. M. Chang, T. Tyan, M. El-bkaily, J. Cheng, A. Marpu, Q. Zeng, and J. Santini. Implicit and explicit finite element methods for crash safety analysis. In *SAE Technical Paper 2007-01-0982*, 2007.
- [8] S. Boria. Design solutions to improve CFRP crash-box impact efficiency for racing applications. In A. Elmarakbi, editor, *Advanced composite materials for automotive applications: structural integrity and crashworthiness*, chapter 9, pages 205–226. Wiley, Chichester, 2014.
- [9] H. Hooputra, H. Gese, H. Dell, and H. Werner. A comprehensive failure model for crashworthiness simulation of aluminium extrusions. *International Journal of Crashworthiness*, 9(5):449–464, 2004.
- [10] A. C. Garg. Delamination—a damage mode in composite structures. *Engineering Fracture Mechanics*, 29(5):557–584, 1988.
- [11] K. Senthil, A. Arockiarajan, R. Palaninathan, B. Santhosh, and K. M. Usha. Defects in composite structures: Its effects and prediction methods - A comprehensive review. *Composite Structures*, 106:139–149, 2013.
- [12] N. J. Pagano and G. A. Schoeppner. Delamination of polymer matrix composites: Problems and assessment. In *Comprehensive Composite Materials*, chapter 2.13, pages 433–528. Elsevier, 2000.
- [13] R. Krueger and T. K. O’Brien. A shell/3D modeling technique for the analysis of delaminated composite laminates. *Composites Part A: Applied Science and Manufacturing*, 32(1):25–44, 2001.
- [14] C. K. Gim. Plate finite element modeling of laminated plates. *Computers & Structures*, 52(1):157–168, 1994.
- [15] G. Alfano and M. A. Crisfield. Finite element interface models for the delamination analysis of laminated composites: Mechanical and computational issues. *International Journal for Numerical Methods in Engineering*, 50:1701–1736, 2001.

- [16] P. P. Camanho, C. G. Davila, and M. F. S. F. De Moura. Numerical simulation of mixed-mode progressive delamination in composite materials. *Journal of Composite Materials*, 37(16):1415–1438, 2003.
- [17] L. Greve and A. K. Pickett. Delamination testing and modelling for composite crash simulation. *Composites Science and Technology*, 66(6):816–826, 2006.
- [18] C. Boegle. Personal Communication, 2016.
- [19] I. Daniel and O. Ishai. *Engineering Mechanics of Composite Materials*. Oxford University Press, New York, 1994.
- [20] H. T. Hahn and S. W. Tsai. *Introduction to Composite Materials*. Technomic Publishing AG, Washington DC, 1980.
- [21] Sapa Extrusion. Alloy 6101. Technical report, Sapa Extrusion North America, Rosemont, IL, 2017.
- [22] ArcelorMittal North America. Dual Phase Steels Data sheet. Technical report, ArcelorMittal North America, 2014.
- [23] P. D. Soden, M. J. Hinton, and A. S. Kaddour. Lamina properties, lay-up configurations and loading conditions for a range of fibre-reinforced composite laminates. *Composites Science and Technology*, 58:1011–1022, 1998.
- [24] P. J. Callus. The effects of hole-size and environment on the mechanical behaviour of a quasi-isotropic AS4 / 3501-6 laminate in tension, compression and bending. Technical report, Australian Government Department of Defence Science and Technology Organisation, 2007.
- [25] QuartusEngineering. Composites 101. <http://www.quartus.com/resources/white-papers/composites-101/>, Accessed 15 September 2017.
- [26] H. Adam. Carbon fibre in automotive applications. *Materials & Design*, 18(4-6):349–355, 1997.
- [27] J. Verrey, M. D. Wakeman, V. Michaud, and J.-A. E. Manson. Manufacturing cost comparison of thermoplastic and thermoset RTM for an automotive floor pan. *Composites Part A: Applied Science and Manufacturing*, 37:9–22, 2006.
- [28] E. Reissner. The effect of transverse shear deformation on the bending of elastic plates. *Journal of Applied Mechanics*, 12:A68–77, 1945.
- [29] R. D. Mindlin. Influence of rotatory inertia and shear on flexural motions of isotropic, elastic plates. *Journal of Applied Mechanics*, 18:31–38, 1951.
- [30] A. E. H. Love. The small free vibrations and deformation of a thin elastic shell. *Philosophical Transactions of the Royal Society of London*, A(179):491–546, 1888.
- [31] J. M. Whitney and N. J. Pagano. Shear deformation in heterogeneous anisotropic plates. *Journal of Applied Mechanics*, 37(4):1031–1036, 1970.
- [32] J. M. Whitney. Shear correction factors for orthotropic laminates under static load. *Journal of Applied Mechanics*, 40(1):302–304, 1973.
- [33] A. S. Kaddour and M. J. Hinton. Input data for test cases used in benchmarking triaxial failure theories of composites. *Journal of Composite Materials*, 46(19-20):2295–2312, 2012.
- [34] R. Talreja and C. V. Singh. *Damage and failure of composite materials*. Cambridge University Press, Cambridge, 2012.
- [35] L. Noels. Fracture Mechanics Online Class. <http://www.ltas-cm3.ulg.ac.be/FractureMechanics/>, Accessed 26 July 2017.
- [36] A. A. A. Alghamdi. Collapsible impact energy absorbers: An overview. *Thin-Walled Structures*, 39(2):189–213, 2001.
- [37] P. H. Thornton and R. A. Jeryan. Crash energy management in composite automotive structures. *International Journal of Impact Engineering*, 7(2):167–180, 1988.
- [38] J. J. Carruthers, A. P. Kettle, and A. M. Robinson. Energy absorption capability and crashworthiness of composite material structures: A review. *Applied Mechanics Reviews*, 51(10):635–649, 1998.
- [39] G. C. Jacob, J. F. Fellers, S. Simunovic, and J. M. Starbuck. Energy absorption in polymer composites for automotive crashworthiness. *Journal of Composite Materials*, 36(7):813–850, 2002.
- [40] D. Hull. A unified approach to progressive crushing of fiber-reinforced composite tubes. *Composites Science and Technology*, 40(4):377–421, 1991.

-
- [41] G. L. Farley and R. M. Jones. Crushing characteristics of continuous fiber-reinforced composite tubes. *Journal of Composite Materials*, 26(1):37–50, 1992.
- [42] P. H. Thornton and P. J. Edwards. Energy absorption in composite tubes. *Journal of Composite Materials*, 16:521–544, 1982.
- [43] D. W. Schmueser and L. E. Wickliffe. Impact energy absorption of continuous fiber composite tubes. *Journal of Engineering Materials and Technology*, 109(1):72–77, 1987.
- [44] G. L. Farley and R. M. Jones. Energy-absorption capability of composite tubes and beams. Technical report, NASA Langley Research Center, Hampton, VA, 1989.
- [45] H. A. Israr, S. Rivallant, and J.-J. Barrau. Experimental investigation on mean crushing stress characterization of carbon-epoxy plies under compressive crushing mode. *Composite Structures*, 96:357–364, 2013.
- [46] K. T. Kedward. Engineering properties of composites. In *Harris' Shock and Vibration Handbook*, chapter 35, pages 35.1–35.31. McGraw-Hill, 5th edition, 2002.
- [47] K. T. Kedward, R. S. Wilson, and S. K. McLean. Flexure of simply curved composite shapes. *Composites*, 20(6):527–536, 1989.
- [48] S. G. Lekhnitskii. *Anisotropic Plates*. Gordon and Breach, New York, Translated from the Russian 2nd edition by S. W. Tsai and T. Cheron, 1968.
- [49] J. P. H. Webber. Through-the-thickness stresses and failure in the corner radius of a laminated composite section (ESDU 94019), 1994.
- [50] R. B. Pipes and N. J. Pagano. Interlaminar stresses in composite laminates under uniform axial extension. *Journal of Composite Materials*, 4:538–548, 1970.
- [51] S. S. Wang and I. Choi. Boundary-layer effects in composite laminates: Part 1 - Free-edge stress singularities. *Journal of Applied Mechanics*, 49(3):541–548, 1982.
- [52] D. Shalev and K. L. Reifsnider. Study of the onset of delamination at holes in composite laminates. *Journal of Composite Materials*, 24(1):42–71, 1990.
- [53] C. Mittelstedt and W. Becker. Interlaminar stress concentrations in layered structures: Part I - a selective literature survey on the free-edge effect since 1967. *Journal of Composite Materials*, 38(12):1037–1062, 2004.
- [54] J. M. Whitney and R. Nuismer. Stress fracture criteria for laminated composites containing stress concentrations. *Journal of Composite Materials*, 8(8):253–265, 1974.
- [55] R. Y. Kim. Experimental and analytical studies on the onset of delamination in laminated composites. *Journal of Composite Materials*, 18:70–80, 1984.
- [56] J. C. Brewer and P. A. Lagace. Quadratic stress criterion for initiation of delamination. *Journal of Composite Materials*, 22(12):1141–1155, 1988.
- [57] D. Leguillon, G. Marion, R. Harry, and F. Lécuyer. The onset of delamination at stress-free edges in angle-ply laminates - analysis of two criteria. *Composites Science and Technology*, 61(3):377–382, 2001.
- [58] C. Kassapoglou. Determination of interlaminar stresses in composite laminates under combined loads. *Journal of Reinforced Plastics and Composites*, 9(1):33–58, 1990.
- [59] C. Kassapoglou and A. DiNicola. Efficient stress solutions at skin stiffener interfaces of composite stiffened panels. *32nd Structures, Structural Dynamics, and Materials Conference*, 30(7):1833–1839, 1991.
- [60] C. Kassapoglou. Calculation of stresses at skin-stiffener interfaces of composite stiffened panels under shear loads. *International Journal of Solids and Structures*, 30(11):1491–1501, 1993.
- [61] C. Kassapoglou. Stress determination at skin-stiffener interfaces of composite stiffened panels under generalized loading. *Journal of Reinforced Plastics and Composites*, 13(6):555–571, 1994.
- [62] K. He, S. V. Hoa, and R. Ganesan. The study of tapered laminated composite structures: A review. *Composites Science and Technology*, 60(14):2643–2657, 2000.
- [63] N. J. Pagano. Exact solutions for rectangular bidirectional and sandwich plates. *Journal of Composite Materials*, 4:20–34, 1970.

- [64] K. Rohwer. Application of higher order theories to the bending analysis of layered composite plates. *International Journal of Solids and Structures*, 29(1):105–119, 1992.
- [65] M. Savoia and J. N. Reddy. A variational approach to three-dimensional elasticity solutions of laminated composite plates. *Journal of Engineering Mechanics*, 59(1992):166–175, 1992.
- [66] R. Rolfes, K. Rohwer, and M. Ballerstaedt. Efficient linear transverse normal stress analysis of layered composite plates. *Computers & Structures*, 68(6):643–652, 1998.
- [67] D. O. Stalnaker and W. W. Stinchcomb. Load history-edge damage studies in two quasi-isotropic graphite epoxy laminates. In *Composite Materials: Testing and Design (Fifth Conference)*, ASTM STP 674, pages 620–641, 1979.
- [68] T. K. O’Brien. Characterization of delamination onset and growth in a composite laminate. Technical report, NASA, Hampton, VA, 1982.
- [69] Z. Kutlu and F.-K. Chang. Composite panels containing multiple through-the-width delaminations and subjected to compression. Part I: Analysis. *Composite Structures*, 31(4):273–296, 1995.
- [70] Z. Kutlu and F.-K. Chang. Composite panels containing multiple through-the-width delaminations and subjected to compression. Part II: experiments & verification. *Composite Structures*, 31(4):297–314, 1995.
- [71] W. S. Chan and C. J. Chou. Effects of delamination and ply fiber waviness on effective axial and bending stiffnesses in composite laminates. *Composite Structures*, 30(3):299–306, 1995.
- [72] J. J. Tracy and G. C. Pardo. Effect of delamination on the flexural stiffness of composite laminates. *Thin-Walled Structures*, 6(5):371–383, 1988.
- [73] P. M. Mujumdar and S. Suryanarayan. Flexural vibrations of beams with delaminations. *Journal of Sound and Vibration*, 125(3):441–461, 1988.
- [74] J. P. Hou and G. Jeronimidis. Vibration of delaminated thin composite plates. *Composites Part A: Applied Science and Manufacturing*, 30(8):989–995, 1999.
- [75] J. P. Hou and G. Jeronimidis. Bending stiffness of composite plates with delamination. *Composites Part A: Applied Science and Manufacturing*, 31(2):121–132, 2000.
- [76] LSTC. LS-DYNA Keyword User’s Manual, R9.0 (r:7883), 2016.
- [77] T. Belytschko, W. K. Liu, B. Moran, and K. Elkhodary. *Nonlinear Finite Elements for Continua and Structures*. Wiley, 2nd edition, 2013.
- [78] LSTC. LS-DYNA Theory Manual (r:7709), 2016.
- [79] T. Belytschko, J. I. Lin, and C. Tsay. Explicit algorithms for the nonlinear dynamics of shells. *Computer Methods in Applied Mechanics and Engineering*, 42(2):225–251, 1984.
- [80] E. D. Jr. Reedy, F. J. Mello, and T. R. Guess. Modeling the initiation and growth of delaminations in composite structures. *Journal of Composite Materials*, 31(8):812–831, 1997.
- [81] E. F. Rybicki and M. F. Kanninen. A finite element calculation of stress intensity factors by a modified crack closure integral. *Engineering Fracture Mechanics*, 9(4):931–938, 1977.
- [82] T. K. Hellen. On the method of virtual crack extensions. *International Journal for Numerical Methods in Engineering*, 9(1):187–207, 1975.
- [83] J. R. Rice. A path independent integral and the approximate analysis of strain concentration by notches and cracks. *Journal of Applied Mechanics*, 35(2):379–386, 1968.
- [84] A. C. Orifici, I. Herszberg, and R. S. Thomson. Review of methodologies for composite material modelling incorporating failure. *Composite Structures*, 86(1-3):194–210, 2008.
- [85] P. P. Camanho and C. G. Davila. Mixed-mode decohesion finite elements for the simulation of delamination in composite materials. Technical report, NASA Langley Research Center, 2002.
- [86] T. K. O’Brien. Interlaminar fracture toughness: the long and winding road to standardization. *Composites Part B: Engineering*, 29(1):57–62, 1998.
- [87] A. Tabiei and R. Tanov. New nonlinear higher order shear deformation shell element for metal forming and crashworthiness analysis: Part I. Formulation and finite element equations. In *Proceedings of the 6-th International LS-DYNA Users Conference*, pages 7–1 – 7–16, 2000.

-
- [88] A. Tabiei and R. Tanov. New nonlinear higher order shear deformation shell element for metal forming and crashworthiness analysis: Part II. Performance validation through standard tests. In *Proceedings of the 6-th International LS-DYNA Users Conference*, pages 7–17 – 7–28, 2000.
- [89] E. N. Dvorkin and K. Bathe. A continuum mechanics based four-node shell element for general non-linear analysis. *Engineering Computations*, 1(1):77–88, 1984.
- [90] J. J. Engblom and O. O. Ochoa. Through-the-thickness stress predictions for laminated plates of advanced composite materials. *International Journal for Numerical Methods in Engineering*, 21:1759–1776, 1985.
- [91] R. M. J. Groh and P. M. Weaver. A computationally efficient 2D model for inherently equilibrated 3D stress predictions in heterogeneous laminated plates. Part I: Model formulation, 2016.
- [92] M. Cho and M. H. Kim. A postprocess method using a displacement field of higher-order shell theory. *Composite Structures*, 34(2):185–196, 1996.
- [93] A. K. Noor and M. Malik. Accurate determination of transverse normal stresses in sandwich panels subjected to thermomechanical loadings. *Computer Methods in Applied Mechanics and Engineering*, 178(3-4):431–443, 1999.
- [94] M. Cho and J.-S. Kim. A postprocess method for laminated shells with a doubly curved nine-noded finite element. *Composites Part B: Engineering*, 31(1):65–74, 2000.
- [95] J. W. Park and Y. H. Kim. Re-analysis procedure for laminated plates using FSDT finite element model. *Computational Mechanics*, 29(3):226–242, 2002.
- [96] A. K. Noor and W. S. Burton. Stress and free vibration analyses of multilayered composite plates. *Composite Structures*, 11(3):183–204, 1989.
- [97] A. K. Noor, W. S. Burton, and J. M. Peters. Predictor-corrector procedures for stress and free vibration analyses of multilayered composite plates and shells. *Computer Methods in Applied Mechanics and Engineering*, 82(1-3):341–363, 1990.
- [98] K. Y. Sze, L. W. He, and Y. K. Cheung. Predictor-corrector procedures for analysis of laminated plates using standard Mindlin finite element models. *Composite Structures*, 50(2):171–182, 2000.
- [99] J. W. Park, K. C. Lee, and Y. H. Kim. Comparative study of finite element based response evaluation methods for laminated plates. *Computational Mechanics*, 32(1-2):115–133, 2003.
- [100] C. W. Jr. Pryor and R. M. Barker. A finite-element analysis including transverse shear effects for applications to laminated plates. *AIAA Journal*, 9(5):912–917, 1971.
- [101] R. A. Chaudhuri. An equilibrium method for prediction of transverse shear stresses in a thick laminated plate. *Computers & Structures*, 23(2):139–146, 1986.
- [102] J. N. Reddy, E. J. Barbero, and J. L. Teply. A plate bending element based on a generalized laminate plate theory. *International Journal for Numerical Methods in Engineering*, 28(10):2275–2292, 1989.
- [103] R. Rolfes and K. Rohwer. Improved transverse shear stresses in composite finite elements based on first order shear deformation theory. *International Journal for Numerical Methods in Engineering*, 40(1):51–60, 1997.
- [104] R. Tanov and A. Tabiei. Adding transverse normal stresses to layered shell finite elements for the analysis of composite structures. *Composite Structures*, 76(4):338–344, 2006.
- [105] G. Alfano, F. Auricchio, L. Rosati, and E. Sacco. MITC finite elements for laminated composite plates. *International Journal for Numerical Methods in Engineering*, 50(3):707–738, 2001.
- [106] R. Roos. *Model for Interlaminar Normal Stresses in Doubly Curved Laminates*. PhD thesis, ETH Zurich, 2008.
- [107] M. Schürig, W. Wagner, and F. Gruttmann. An enhanced FSDT model for the calculation of interlaminar shear stresses in composite plate structures. *Computational Mechanics*, 44(6):765–776, 2009.
- [108] T. Kant and B. S. Manjunatha. On accurate estimation of transverse stresses in multilayer laminates. *Computers & Structures*, 50(3):351–365, 1994.
- [109] N. Moës, J. Dolbow, and T. Belytschko. A finite element method for crack growth without remeshing. *International Journal for Numerical Methods in Engineering*, 46:131–150, 1999.
- [110] T. Nagashima and H. Suemasu. X-FEM analyses of a thin-walled composite shell structure with a delamination. *Computers & Structures*, 88(9-10):549–557, 2010.

- [111] J. Brouzoulis, M. Fagerström, and E. Svenning. A shell element formulation for the simulation of propagating delamination and through-thickness cracks. In *16th European Conference on Composite Materials*, 2014.
- [112] J. Främby, M. Fagerström, and J. Brouzoulis. Delamination initiation and propagation modelling with an enriched shell element formulation. *Composite Structures*, 126:196–205, 2015.
- [113] A. K. Noor and W. S. Burton. Assessment of computational models for multilayered anisotropic plates. *Composite Structures*, 14(3):233–265, 1990.
- [114] A. K. Noor, W. S. Burton, and J. M. Peters. Assessment of computational models for multilayered composite cylinders. *International Journal of Solids and Structures*, 27(10):1269–1286, 1991.
- [115] A. K. Noor and M. Malik. An assessment of five modeling approaches for thermo-mechanical stress analysis of laminated composite panels. *Computational Mechanics*, 25(1):43–58, 2000.
- [116] K. Rohwer, S. Friedrichs, and C. Wehmeyer. Analyzing laminated structures from fibre-reinforced composite material - An assessment. *Technische Mechanik*, 25(1):59–77, 2005.
- [117] A. Puck. *Festigkeitsanalyse von Faser-Matrix-Laminaten: Modelle für die Praxis*. Carl Hanser, München Wien, 1996.
- [118] M. J. Hinton, A. S. Kaddour, and P. D. Soden. *Failure criteria in fibre reinforced polymer composites*. Elsevier Ltd, Oxford, 1st edition, 2004.
- [119] M. J. Hinton and A. S. Kaddour. The second world-wide failure exercise: Benchmarking of failure criteria under triaxial stresses for fibre-reinforced polymer composites. In *16th International Conferences on Composite Materials*, 2007.
- [120] A. S. Kaddour and M. J. Hinton. Maturity of 3D failure criteria for fibre-reinforced composites: Comparison between theories and experiments: Part B of WWFE-II. *Journal of Composite Materials*, 47(6-7):925–966, 2013.
- [121] A. S. Kaddour, M. J. Hinton, P. A. Smith, and S. Li. The background to the third world-wide failure exercise. *Journal of Composite Materials*, 47(20-21):2417–2426, 2013.
- [122] S. T. Pinho, C. G. Dávila, P. P. Camanho, L. Iannucci, and P. Robinson. Failure models and criteria for FRP under in-plane or three-dimensional stress states including shear non-linearity. Technical report, NASA Langley Research Center, Hampton, VA, 2005.
- [123] F. Laurin, N. Carrere, and J.-F. Maire. A multiscale progressive failure approach for composite laminates based on thermodynamical viscoelastic and damage models. *Composites Part A: Applied Science and Manufacturing*, 38(1):198–209, 2007.
- [124] Z. Hashin. Failure criteria for unidirectional fiber composites. *Journal of Applied Mechanics*, 47(2):329, 1980.
- [125] A. Turon, P. P. Camanho, J. Costa, and C. G. Davila. An interface damage model for the simulation of delamination under variable-mode ratio in composite materials. Technical Report October, NASA Langley Research Center, 2004.
- [126] N. Carrere, F. Laurin, and J.-F. Maire. Micromechanical-based hybrid mesoscopic three-dimensional approach for non-linear progressive failure analysis of composite structures - Part B: Comparison with experimental data. *Journal of Composite Materials*, 47(6-7):743–762, 2013.
- [127] A. S. Kaddour, M. J. Hinton, S. Li, and P. A. Smith. Damage theories for fibre-reinforced polymer composites: The third world-wide failure exercise (WWFE-III). *16th International Conferences on Composite Materials*, page 10, 2007.
- [128] A. S. Kaddour, M. J. Hinton, P. A. Smith, and S. Li. Mechanical properties and details of composite laminates for the test cases used in the third world-wide failure exercise. *Journal of Composite Materials*, 47(20-21):2427–2442, 2013.
- [129] F. Laurin, N. Carrere, C. Huchette, and J.-F. Maire. A multiscale hybrid approach for damage and final failure predictions of composite structures. *Journal of Composite Materials*, 47(20-21):2713–2747, 2013.
- [130] S. T. Pinho, G. Vyas, and P. Robinson. Response and damage propagation of polymer-matrix fibre-reinforced composites: Predictions for WWFE-III Part A. *Journal of Composite Materials*, 47(20-21):2595–2612, 2013.

-
- [131] A. S. Kaddour, M. J. Hinton, P. A. Smith, and S. Li. A comparison between the predictive capability of matrix cracking, damage and failure criteria for fibre reinforced composite laminates: Part A of the third world-wide failure exercise. *Journal of Composite Materials*, 47(20-21):2749–2779, 2013.
- [132] M. Knops. *Analysis of Failure in Fiber Polymer Laminates: The Theory of Alfred Puck*. Springer Berlin Heidelberg, 2nd edition, 2008.
- [133] A. Puck, J. W. Kopp, and M. Knops. Guidelines for the determination of the parameters in Puck's action plane strength criterion. *Composites Science and Technology*, 62(3):371–378, 2002.
- [134] D. Huybrechts. Ein erster Beitrag zur Verifikation des wirkebenebezogenen Zwischenfaserbruchkriteriums nach Puck (a first contribution in verifying the action-plane-related inter-fiber-failure criterion after Puck). Technical report, Institut für Kunststoffverarbeitung (IKV) Bd. 44, Aachen, Mainz, 1996.
- [135] R. Cuntze, J. W. Kopp, and D. Huybrechts. Neue bruchkriterien und Festigkeitsnachweis für unidirektionalen Faserkunststoffverbund unter mehrachsiger Beanspruchung - Modelle und Experimente. Technical report, VDI-Fortschrittberichte, Reihe 5: Grund und Werkstoffe, Düsseldorf, 1997.
- [136] J. W. Kopp. Zur Spannungs- und Festigkeitsanalyse für unidirektionalen Faserverbundkunststoff (Contribution to the Stress and Strength Analysis of Unidirectionally Fiber Reinforced Plastics). Technical report, Institut für Kunststoffverarbeitung (IKV) Bd. 99, Mainz, Aachen, 2000.
- [137] O. O. Ochoa and J. J. Engblom. Analysis of progressive failure in composites. *Composites Science and Technology*, 28(2):87–102, 1987.
- [138] J. D. Lee. Three dimensional finite element analysis of damage accumulation in composite laminate. *Computers & Structures*, 15(3):335–350, 1982.
- [139] J. P. Hou, N. Petrinic, and C. Ruiz. Prediction of impact damage in composite plates. *Composites in Science and Technology*, 60:273–281, 2000.
- [140] R. J. C. Creemers. Interlaminar shear strength criteria for composites - An assessment by means of statistical analysis. Technical report, National Aerospace Laboratory NLR, Amsterdam, 2010.
- [141] M. T. Fenske and A. J. Vizzini. The inclusion of in-plane stresses in delamination criteria. *Journal of Composite Materials*, 35(15):1325–1342, 2001.
- [142] Cytec Industries Inc. APC-2-PEEK thermoplastic polymer technical data sheet, 2015.
- [143] R. H. Martin. Delamination failure in a unidirectional curved composite laminate. Technical report, NASA Langley Research Center, Hampton, VA, 1990.
- [144] G. Wimmer, C. Schuecker, and H. E. Pettermann. Numerical simulation of delamination in laminated composite components - A combination of a strength criterion and fracture mechanics. *Composites Part B: Engineering*, 40(2):158–165, 2009.
- [145] F. W. Crossman, W. J. Warren, A. S. D. Wang, and G. E. Law. Initiation and growth of transverse cracks and edge delamination in composite laminates part 2. Experimental correlation. *Journal of Composite Materials*, 14(1):88–108, 1980.
- [146] J. N. Reddy and D. H. Robbins. Theories and computational models for composite laminates. *Applied Mechanics Reviews*, 47(6):147–169, 1994.
- [147] D. H. Robbins and J. N. Reddy. Variable kinematic modelling of laminated composite plates. *International Journal for Numerical Methods in Engineering*, 39:2283–2317, 1996.

Appendix A

Obtaining Transverse Normal Stresses in a One-Dimensional Linear Element

In addition to Section 4.1.3, this appendix presents an attempt to obtain the transverse normal stresses through post-processing of the BLT element; for this a parabolic distribution of the out-of-plane displacement component u_z is needed. To simplify the problem, obtaining this solution for a one-dimensional element is analysed. This is done by trying to find a non-trivial solution for C_{11} in Equation (A.1), making sure the internal strain energy of that solution is equal to that of the one-dimensional FSDT solution of Equation (A.2).

$$u_{z\mathcal{P}}(\xi) = C_{11} (1 - \xi^2) + \frac{-\xi + 1}{2} u_{z1} + \frac{\xi + 1}{2} u_{z2} \quad (\text{A.1})$$

$$u_{z\mathcal{L}}(\xi) = \frac{-\xi + 1}{2} u_{z1} + \frac{\xi + 1}{2} u_{z2} \quad (\text{A.2})$$

$$\theta_y(\xi) = \frac{-\xi + 1}{2} \theta_{y1} + \frac{\xi + 1}{2} \theta_{y2} \quad (\text{A.3})$$

With ξ the isoparametric coordinate, ranging from -1 to 1, and u_{z1} and u_{z2} the out of plane displacement at nodes 1 and 2, respectively. Furthermore, the subscripts \mathcal{L} and \mathcal{P} denote the linear and parabolic interpolation for the out-of-plane displacement.

Equations (A.4) and (A.5) give the stress-strain relations for an orthotropic material and the internal strain energy equation, respectively.

$$\begin{bmatrix} \sigma_{xx} \\ \sigma_{yy} \\ \sigma_{zz} \\ \tau_{yz} \\ \tau_{xz} \\ \tau_{xy} \end{bmatrix} = \begin{bmatrix} E_{11} & E_{12} & E_{13} & 0 & 0 & E_{16} \\ E_{12} & E_{22} & E_{23} & 0 & 0 & E_{26} \\ E_{13} & E_{23} & E_{33} & 0 & 0 & E_{36} \\ 0 & 0 & 0 & E_{44} & E_{45} & 0 \\ 0 & 0 & 0 & E_{45} & E_{55} & 0 \\ E_{16} & E_{26} & E_{36} & 0 & 0 & E_{66} \end{bmatrix} \begin{bmatrix} \varepsilon_{xx} \\ \varepsilon_{yy} \\ \varepsilon_{zz} \\ \gamma_{yz} \\ \gamma_{xz} \\ \gamma_{xy} \end{bmatrix} \quad (\text{A.4})$$

90 Obtaining Transverse Normal Stresses in a One-Dimensional Linear Element

$$U = \frac{1}{2} \iiint_V \sigma_{xx}\varepsilon_{xx} + \sigma_{yy}\varepsilon_{yy} + \sigma_{zz}\varepsilon_{zz} + \tau_{xy}\gamma_{xy} + \tau_{xz}\gamma_{xz} + \tau_{yz}\gamma_{yz} dV \quad (\text{A.5})$$

$$\varepsilon_{xx} = u_{x,x} + z\theta_{y,x} \quad (\text{2.2 revisited})$$

$$\gamma_{xz} = u_{z,x} + \theta_y \quad (\text{2.5 revisited})$$

$$\varepsilon_{zz} = u_{z,z} \quad (\text{A.6})$$

Assuming unit depth in y and no dependence on y :

$$U = \frac{1}{2} \iint \sigma_{xx}\varepsilon_{xx} + \sigma_{zz}\varepsilon_{zz} + \tau_{xz}\gamma_{xz} dx dz \quad (\text{A.7})$$

Substituting stresses from Equation (A.4)

$$U = \frac{1}{2} \iint E_{11}\varepsilon_{xx}^2 + E_{33}\varepsilon_{zz}^2 + 2E_{13}\varepsilon_{xx}\varepsilon_{zz} + E_{55}\gamma_{xz}^2 dx dz \quad (\text{A.8})$$

Substituting strains from Equations (2.2), (2.5) and (A.6):

$$U = \frac{1}{2} \iint E_{11}(u_{x,x} + z\theta_{y,z})^2 + E_{33}u_{z,z}^2 + 2E_{13}(u_{x,x} + z\theta_{y,z})u_{z,z} + E_{55}(u_{z,x} + \theta_y)^2 dx dz \quad (\text{A.9})$$

Of interest is the equivalence of the internal energy of the parabolic interpolation with respect to the linear interpolation. Therefore, the terms which are equal for both energies are cancelled out:

$$U = \frac{1}{2} \iint E_{55} (u_{z,x}^2 + u_{z,x}\theta_y) dx dz \quad (\text{A.10})$$

Assume a coordinate system such that $x = \xi$, and hence all dependencies on z drop:

$$(u_{z,x})_{\mathcal{L}} = \frac{u_{z2} - u_{z1}}{2} \quad (\text{A.11})$$

$$(u_{z,x})_{\mathcal{P}} = \frac{u_{z2} - u_{z1}}{2} - 2C_{11}\xi \quad (\text{A.12})$$

Substituting Equations (A.3), (A.11) and (A.12) leads to the two internal energies:

$$U_{\mathcal{L}} = \frac{E_{55}}{2} \int dz \int_{\xi=-1}^{\xi=1} \left(\frac{u_{z2} - u_{z1}}{2} \right)^2 + \left(\frac{u_{z2} - u_{z1}}{2} \right) \left(\frac{1 - \xi}{2} \theta_{y1} + \frac{\xi + 1}{2} \theta_{y2} \right) d\xi \quad (\text{A.13})$$

$$U_{\mathcal{P}} = \frac{E_{55}}{2} \int dz \int_{\xi=-1}^{\xi=1} \left(\frac{u_{z2} - u_{z1}}{2} - 2C_{11}\xi \right)^2 + \left(\frac{u_{z2} - u_{z1}}{2} - 2C_{11}\xi \right) \left(\frac{1-\xi}{2}\theta_{y1} + \frac{\xi+1}{2}\theta_{y2} \right) d\xi \quad (\text{A.14})$$

Working out integrals:

$$U_{\mathcal{L}} = \frac{E_{55}}{4} \int dz [(u_{z1} - u_{z2})(u_{z1} - u_{z2} - \theta_{y1} - \theta_{y2})] \quad (\text{A.15})$$

$$U_{\mathcal{P}} = \frac{E_{55}}{4} \int dz \left[(u_{z1} - u_{z2})(u_{z1} - u_{z2} - \theta_{y1} - \theta_{y2}) + \frac{16}{3}C_{11}^2 + \frac{4}{3}C_{11}(\theta_{y1} - \theta_{y2}) \right] \quad (\text{A.16})$$

Now, equating $U_{\mathcal{L}}$ to $U_{\mathcal{P}}$ and solve for C_{11} leads to the trivial solution and:

$$C_{11} = \frac{-\theta_{y1} + \theta_{y2}}{4} \quad (\text{A.17})$$

The original goal of this method was to find a parabolic solution for u_z , such that it can be used to calculate the transverse normal stress, for that $\gamma_{xz,x}$ should exist. Based on Equation (2.5), it is given by Equation (A.18).

$$\gamma_{xz,x} = u_{z,xx} + \theta_{y,x} \quad (\text{A.18})$$

Continuing with the assumption of a coordinate system such that $x = \xi$ and substituting $u_{z\mathcal{P}}$ and θ_y from Equations (A.1) and (A.3) and C_{11} from Equation (A.17) leads to Equation (A.19).

$$\gamma_{xz,\xi} = \frac{\partial^2}{\partial \xi^2} \left(\frac{-\theta_{y1} + \theta_{y2}}{4} (1 - \xi^2) + \frac{-\xi + 1}{2} u_{z1} + \frac{\xi + 1}{2} u_{z2} \right) + \frac{\partial}{\partial \xi} \left(\frac{-\xi + 1}{2} \theta_{y1} + \frac{\xi + 1}{2} \theta_{y2} \right) \quad (\text{A.19})$$

Solving Equation (A.19) leads to $\gamma_{xz,\xi} = 0$. Hence, while a solution was found for a parabolic distribution of the out-of-plane displacement, the effect was that the sought for differential is equal to zero.

92 Obtaining Transverse Normal Stresses in a One-Dimensional Linear Element

Appendix B

Transverse Normal Stress Implementation

This appendix provides the necessary equations in order to implement the post-processing needed to calculate the transverse normal stresses. This is under the assumption that a valid, parabolic distribution is available for the out-of-plane displacement u_z , i.e. a solution to the unsolved problem of Appendix A. The goal is to obtain $\Delta\gamma_{xz,x}$, $\Delta\gamma_{xz,y}$, $\Delta\gamma_{yz,x}$ and $\Delta\gamma_{yz,y}$, such that the part of Section 4.1.2 on the transverse normal stresses can be implemented as well.

This will be done using spatial derivatives of the strain-displacement matrix: $\mathcal{B}_{,x}$ and $\mathcal{B}_{,y}$. The items of interest for the calculation of the mentioned derivatives are given in the shortened notations in Equations (B.1) and (B.2).

$$\Delta\gamma_{,x} = \mathcal{B}_{,x}^s \Delta\mathbf{u}^s$$
$$\begin{bmatrix} \Delta\gamma_{xz,x} \\ \Delta\gamma_{yz,x} \end{bmatrix} = \begin{bmatrix} N_{1,xx} & 0 & N_{1,x} & \dots & N_{4,xx} & 0 & N_{4,x} & N_{5,xx} & N_{6,xx} \\ N_{1,xy} & -N_{1,x} & 0 & \dots & N_{4,xy} & -N_{4,x} & 0 & N_{5,xy} & N_{6,xy} \end{bmatrix} \begin{bmatrix} \Delta w_1 \\ \Delta\theta_{x1} \\ \Delta\theta_{y1} \\ \vdots \\ \Delta w_4 \\ \Delta\theta_{x4} \\ \Delta\theta_{y4} \\ C_5 \\ C_6 \end{bmatrix}$$

(B.1)

$$\Delta\boldsymbol{\gamma}_{,y} = \mathcal{B}_{,y}^s \Delta\mathbf{u}^s$$

$$\begin{bmatrix} \Delta\gamma_{xz,y} \\ \Delta\gamma_{yz,y} \end{bmatrix} = \begin{bmatrix} N_{1,xy} & 0 & N_{1,y} & \dots & N_{4,xy} & 0 & N_{4,y} & N_{5,xy} & N_{6,xy} \\ N_{1,yy} & -N_{1,y} & 0 & \dots & N_{4,yy} & -N_{4,y} & 0 & N_{5,yy} & N_{6,yy} \end{bmatrix} \begin{bmatrix} \Delta w_1 \\ \Delta\theta_{x1} \\ \Delta\theta_{y1} \\ \vdots \\ \Delta w_4 \\ \Delta\theta_{x4} \\ \Delta\theta_{y4} \\ C_5 \\ C_6 \end{bmatrix} \quad (\text{B.2})$$

In which C_5 and C_6 are the constants of Equation (4.29), N_1 to N_4 are given by Equation (3.15) and N_5 and N_6 are given by Equation (B.3)

$$N_5 = (1 - \xi^2); \quad N_6 = (1 - \eta^2) \quad (\text{B.3})$$

The second derivatives of the shape functions require an approach presented by Reddy et al. [102], shown in Equation (B.4).

$$\begin{bmatrix} N_{I,xx} \\ N_{I,yy} \\ N_{I,xy} \end{bmatrix} = \mathbf{J}_1^{-1} \left(\begin{bmatrix} N_{I,\xi\xi} \\ N_{I,\eta\eta} \\ N_{I,\xi\eta} \end{bmatrix} - \mathbf{J}_2 \begin{bmatrix} N_{I,x} \\ N_{I,y} \end{bmatrix} \right) \quad (\text{B.4})$$

Subscript I denotes the shape function. Note that there are 6 shape functions for w . Furthermore, \mathbf{J}_1 and \mathbf{J}_2 given by Equations (B.5) and (B.6), respectively.

$$\mathbf{J}_1 = \begin{bmatrix} (x,\xi)^2 & (y,\xi)^2 & 2x,\xi y,\xi \\ (x,\eta)^2 & (y,\eta)^2 & 2x,\eta y,\eta \\ x,\xi x,\eta & y,\xi y,\eta & x,\eta y,\xi + x,\xi y,\eta \end{bmatrix} \quad (\text{B.5})$$

$$\mathbf{J}_2 = \begin{bmatrix} x,\xi\xi & y,\xi\xi \\ x,\eta\eta & y,\eta\eta \\ x,\xi\eta & y,\xi\eta \end{bmatrix} \quad (\text{B.6})$$

And the inverse of Equation (B.5) given by Equation (B.7).

$$\mathbf{J}_1^{-1} = \frac{1}{(x,\eta y,\xi - x,\xi y,\eta)^2} \begin{bmatrix} (y,\eta)^2 & (y,\xi)^2 & -2y,\eta y,\xi \\ (x,\eta)^2 & (x,\xi)^2 & -2x,\eta x,\xi \\ -x,\eta y,\eta & -x,\xi y,\xi & x,\eta y,\xi + x,\xi y,\eta \end{bmatrix} \quad (\text{B.7})$$

Hence, if there is a possibility to adapt the BLT element in such a way that the out-of-plane displacement can be interpolated using parabolic shape functions, while making sure the transverse shear strains do not become equal to zero as a result, the calculation of the spatial derivatives of the transverse shear strains can be implemented in the user modules of LS-Dyna by using the equations of this appendix.